

# **Seismic Ray Impedance Inversion**

**Xiaolin Lu**

**A THESIS SUBMITTED TO  
IMPERIAL COLLEGE LONDON  
FOR THE DEGREE OF  
DOCTOR OF PHILOSOPHY**

Centre for Reservoir Geophysics  
Department of Earth Science and Engineering  
Imperial College London



## **Declaration of Originality**

I, Xiaolin Lu, declare that this thesis is entirely my own work. Information derived from the published and unpublished work of others has been acknowledged in the text and a list of references is given in the bibliography.





## Abstract

This thesis investigates a prestack seismic inversion scheme implemented in the ray parameter domain. Conventionally, most prestack seismic inversion methods are performed in the incidence angle domain. However, inversion using the concept of ray impedance, as it honours ray path variation following the elastic parameter variation according to Snell's law, shows the capacity to discriminate different lithologies if compared to conventional elastic impedance inversion.

The procedure starts with data transformation into the ray-parameter domain and then implements the ray impedance inversion along constant ray-parameter profiles. With different constant-ray-parameter profiles, mixed-phase wavelets are initially estimated based on the high-order statistics of the data and further refined after a proper well-to-seismic tie. With the estimated wavelets ready, a Cauchy inversion method is used to invert for seismic reflectivity sequences, aiming at recovering seismic reflectivity sequences for blocky impedance inversion. The impedance inversion from reflectivity sequences adopts a standard generalised linear inversion scheme, whose results are utilised to identify rock properties and facilitate quantitative interpretation. It has also been demonstrated that we can further invert elastic parameters from ray impedance values, without eliminating an extra density term or introducing a Gardner's relation to absorb this term.

Ray impedance inversion is extended to P-S converted waves by introducing the definition of converted-wave ray impedance. This quantity shows some advantages in connecting prestack converted wave data with well logs, if compared with the shear-wave elastic impedance derived from the Aki and Richards approximation to the Zoeppritz equations. An analysis of P-P and P-S wave data under the framework of ray impedance is conducted through a real multicomponent dataset, which can reduce the uncertainty in lithology identification.

Inversion is the key method in generating those examples throughout the entire thesis as we believe it can render robust solutions to geophysical problems. Apart from the reflectivity sequence, ray impedance and elastic parameter inversion mentioned above, inversion methods are also adopted in transforming the prestack data from the offset domain to the ray-parameter domain, mixed-phase wavelet estimation, as well as the registration of P-P and P-S waves for the joint analysis.

The ray impedance inversion methods are successfully applied to different types of datasets. In each individual step to achieving the ray impedance inversion, advantages, disadvantages as well as limitations of the algorithms adopted are detailed. As a conclusion, the ray impedance related analyses demonstrated in this thesis are highly competent compared with the classical elastic impedance methods and the author would like to recommend it for a wider application.

## **Acknowledgments**

I would like to thank my supervisor, Prof. Yanghua Wang, for his guidance in this research topic and in the field of seismic inversion. I would also like to thank my second supervisor, Prof Mike Warner, for his support throughout these years.

Special thanks go to the sponsors of the Centre for Reservoir Geophysics. Without their financial support my research would not be carried on.

Also thank Dr Joanna Morgan, Dr. Ivan Stekl and all my colleagues in the Centre for Reservoir Geophysics.

Finally I would like to thank my family, Miss Lisha Xie and all my friends for their continuous help.



# Contents

<b>Declaration of Originality .....</b>	<b>3</b>
<b>Abstract.....</b>	<b>5</b>
<b>Acknowledgments .....</b>	<b>7</b>
<b>Contents .....</b>	<b>9</b>
<b>List of Figures.....</b>	<b>11</b>
<b>Glossary .....</b>	<b>17</b>
<b>List of Symbols .....</b>	<b>19</b>
<b>Chapter 1 Introduction.....</b>	<b>23</b>
1.1 From acoustic impedance to elastic impedance.....	23
1.2 Seismic ray impedance .....	28
1.3 Evaluation of $\nu$ value in RI.....	29
1.4 Comparison between RI and EI in identifying lithology .....	32
1.5 Construction of constant ray-parameter profiles.....	39
1.5.1 Tau-p transform on CMP gathers .....	40
1.5.2 CMP gathers mapped using local slope .....	44
1.5.3 Ray-parameter domain common image point gathers .....	45
1.5.4 Ray tracing in offset domain CIP gathers .....	46
1.6 The dataset for demonstration in the thesis.....	49
1.7 Overview of this thesis.....	50
Appendix 1.A Derivation of acoustic and elastic ray impedance .....	53
Appendix 1.B A simple verification regarding the tau-p transform in CMP gathers .....	54
<b>Chapter 2 Mixed-phase wavelet estimation.....</b>	<b>57</b>
2.1 Introduction.....	57
2.2 High-order statistics of seismic data .....	58
2.3 The validity of the prerequisites in using HOS.....	61
2.4 Constant phase estimation.....	68
2.5 Mixed-phase wavelet estimation by iterative linear inversion .....	70
2.6 Mixed-phase wavelet estimation in practice.....	72
2.7 Discussion .....	77
<b>Chapter 3 Seismic reflectivity inversion .....</b>	<b>78</b>
3.1 Introduction.....	78
3.2 Regularisation using a Cauchy priori model.....	80
3.2.1 Seismic reflectivity inversion by time-domain deconvolution .....	80
3.2.2 The Cauchy priori model .....	82
3.3 Estimation of the Cauchy parameter and application .....	85
3.4 Statistical information of reflectivity series with different constraints.....	89
3.5 Conclusions of sparseness constraint reflectivity inversion .....	92
<b>Chapter 4 Ray impedance inversion and application.....</b>	<b>95</b>

4.1 Preparation for ray impedance inversion .....	95
4.2 Ray impedance inversion .....	99
4.2.1 Initial model building .....	100
4.2.2 Reflectivity scalar .....	100
4.2.3 Ray impedance inversion result .....	101
4.3 Lithology discrimination from the ray impedance inversion result .....	104
4.4 Comparison with elastic impedance inversion result .....	108
4.5 Discussion and conclusions .....	112
<b>Chapter 5 Simultaneous elastic parameter inversion from ray impedance .....</b>	<b>115</b>
5.1 Elastic parameter inversion from ray impedance .....	116
5.2 Numerical test of elastic parameter inversion from ray impedance .....	117
5.2.1 Noise-free synthetic test .....	117
5.2.2 Noisy synthetic test and the calculation of the weighting matrices .....	120
5.2.3 Uncertainty and resolution analysis .....	124
5.3 Two-parameter elastic inversion from ray impedance .....	127
5.4 Two parameter elastic inversion from ray impedance -- real data application	130
5.5 Discussion and Conclusions .....	135
<b>Chapter 6 Converted-wave ray impedance inversion and joint analysis with P-P</b>	
<b>wave ray impedance .....</b>	<b>137</b>
6.1 The dataset for this study .....	138
6.2 Derivation of converted ray impedance .....	141
6.3 Event matching between P-P and P-S waves .....	146
6.4 Inversion result analysis .....	152
6.5 Conclusions .....	157
<b>Chapter 7 Conclusions and future work .....</b>	<b>159</b>
7.1 General conclusions .....	159
7.2 Future work .....	161
7.3 Software developed .....	163
<b>Publications .....</b>	<b>165</b>
<b>References .....</b>	<b>167</b>

# List of Figures

<b>Figure 1.1</b> Graphical differences between equation (1.7) and equation (1.8).....	25
<b>Figure 1.2</b> Five well logs from a producing gas well in the North Sea. ....	31
<b>Figure 1.3</b> Linear regressions of $\log \rho$ (vertical axis) and $\log \beta$ (horizontal axis) in different formations to identify the Gardner's type of relationship between density and S-wave velocity. (a) - (f) are corresponding to the six formations in the well shown in Figure 1.2, from top to bottom respectively. ....	32
<b>Figure 1.4</b> P-wave reflection coefficient comparisons between the quadratic expression (1.17) and the linear expression (1.10), using the exact values for reference. (a)-(e) are corresponding to the five examples described in the context. ....	35
<b>Figure 1.5</b> Comparison between the accuracy of the synthetic traces generated from RI and EI. (a) Synthetic traces generated from the Zoeppritz equations (index 1) and from RI values (index 2) at ray parameter 0.21s/km. (b) Synthetic traces generated from the Zoeppritz equations (index 1) and from EI values (index 2) at $30^\circ$ . ....	36
<b>Figure 1.6</b> Crossplots of (a) normalised EI(30), (b) RI( $p = 0.21$ ) with a unique $v$ value for different lithologies and (c) RI( $p = 0.21$ ) using different $v$ values for different lithologies, versus AI. The black lines denote the main axis.....	37
<b>Figure 1.7</b> Smoothed Gaussian distributions for different facies when projecting their crossplots in Figure 1.6 along the main axis for (a) normalised EI(30), (b) RI( $p = 0.21$ ). ....	39
<b>Figure 1.8</b> A dipping geometry for a CMP gather .....	41
<b>Figure 1.9</b> Comparison of (a) average horizontal slownesses and (b) striking ray parameter values as functions of dip angles and incidence angles. ....	42
<b>Figure 1.10</b> (a) A synthetic CMP gather composed of hyperbolas. (b) The corresponding point-source tau-p transform result. ....	43
<b>Figure 1.11</b> Schematic illustration of the bending ray method ( $k = 3$ ). ....	47
<b>Figure 1.12</b> Synthetic example of bending ray tracing method for a P-P wave. ....	49
<b>Figure 1.13</b> The stack section of a turbidite reservoir of Tertiary age in the North Sea with geological horizons and well log. ....	50
<b>Figure 1.14</b> Flowchart of the inversion procedure in this thesis. ....	52
<b>Figure 1.15</b> A simple ray-path geometry for a reflection in a CMP gather. ....	54
<b>Figure 2.1</b> (a) A synthetic zero-mean mixed-phase wavelet and its amplitude spectrum is plotted in (b) and the time-shifted phase spectrum in (c). ....	61
<b>Figure 2.2</b> (a) A seismic reflectivity sequence. (b) The amplitude spectrum of the sequence in (a). (c) The equivalent white sequence corresponding to (a). (d) The amplitude spectrum of the sequence in (c). (e) The whitening filter convolved with (a) to obtain (c). ....	63
<b>Figure 2.3</b> A synthetic trace by convolving the mixed-phase wavelet (Figure 2.1a) and the white reflectivity sequence (Figure 2.2c). ....	65

<b>Figure 2.4</b> (a) A fourth-order moment (FOM) slice of the wavelet in Figure 2.1a. (b) A fourth-order cumulant (FOC) slice of the synthetic trace shown in Figure 2.1b. (c) A slice of Parzen window. (d) Approximate FOM slice of wavelet by windowing FOC of the seismic trace. (e) FOC slice of a very long seismic trace.	66
<b>Figure 2.5</b> (a) A random non-Gaussian sequence denoting reflectivity coefficients. (b) The probability density function of (a). (c) The long synthetic seismic trace.	68
<b>Figure 2.6</b> (a) Kurtosis variation with rotation angle for the seismic trace in Figure 2.5c. (b) Constant-phase wavelet corresponding to the maximum kurtosis.	70
<b>Figure 2.7</b> Estimated mixed-phase wavelet using iterative inversion scheme.	72
<b>Figure 2.8</b> The real seismic profile used for estimating wavelet.	73
<b>Figure 2.9</b> (a) Estimated wavelet spectrum from the data. (b) The kurtosis variation with rotation angle. (c) The estimated constant-phase wavelet from the 3-second window. (d) The estimated mixed-phase wavelet from the 3-second window. (e) The estimated constant-phase wavelet from the 1.5-second window. (f) The estimated mixed-phase wavelet from the 1.5-second window.	74
<b>Figure 2.10</b> Correlation between the seismic data and the synthetic trace generated from the wavelets of (a) HOS method and (b) Walden and White (1998) method. The five blue traces are repeated reflectivity series convolved with the corresponding wavelet and the five red traces are the same as the single red one, which represents the real seismic trace in the well-tie position.	76
<b>Figure 2.11</b> Wavelet estimated using Walden and White (1998) method when the best well-tie is achieved.	77
<b>Figure 3.1</b> Deconvolution illustrations. (a) An original seismic section. (b) Deconvolved seismic reflectivity. (c) Synthetic seismic section by convolving (b) with the wavelet. (d) Difference between the original and synthetic seismic sections caused by pre-whitening in the matrix inversion.	81
<b>Figure 3.2</b> Schematic comparison of PDF between a Gaussian distribution and a Cauchy distribution.	83
<b>Figure 3.3</b> (a) Histogram of the reflectivity amplitudes (red marks) with its best-fit Gaussian (solid line) and Cauchy (dashed line) curves. (b) The $Q$ function plotted versus the Cauchy parameter $\lambda$ . The estimated $\hat{\lambda}$ value corresponding to the minimum $Q$ value is 0.0042. Estimation is based on the well shown in Figure 1.2.	86
<b>Figure 3.4</b> (a) Sparse seismic reflectivity sequences under the Cauchy constraint using the optimum parameter. (b) Synthetic seismic section by convolving (a) with the wavelet. (c) Difference between the original and synthetic seismic sections caused by the Cauchy constraint inversion.	87
<b>Figure 3.5</b> Convergence rate of the iterative inversion with Cauchy constraint.	89
<b>Figure 3.6</b> The amplitude spectra of the original seismic profile (grey), the least-squares inversion result (black) and the seismic reflectivity sequences after different numbers of iterations in Cauchy constraint inversion (colour).	89
<b>Figure 3.7</b> The histograms of seismic reflectivity after a different number of iterations. (a)-(h) indicate the probability density function of seismic reflectivity after 1 to 8 iterations respectively.	90
<b>Figure 3.8</b> (a) A Cauchy fitting (dashed line, merged with the original distribution dots) of the reflectivity distribution after the first Cauchy constraint distribution compared with the best-fit Gaussian distribution (solid line). (b) After the 8th iteration, the reflectivity distribution changes towards Gaussian (solid line) rather than Cauchy (dashed line).	91



<b>Figure 3.9</b> (a) The computed acoustic impedance well log at CDP 2232. (b) The original stack section. (c) The Gaussian constraint least-squares inversion result. (d) The Cauchy constraint inversion result after 2 iterations. (e) The Cauchy constraint inversion result after 8 iterations. (f) The QC panel of synthetic traces generated from different reflectivity sequences.....	92
<b>Figure 4.1</b> CIP gathers at CDP 2232 in (a) the offset domain and (b) the ray-parameter domain.....	96
<b>Figure 4.2</b> Interval velocity field in the ray-tracing to transform the CIP gathers from the offset domain to the ray-parameter domain. ....	97
<b>Figure 4.3</b> The constant ray-parameter profiles at (a) 0.05 s/km and (b) 0.2 s/km. (c) The full stack.....	98
<b>Figure 4.4</b> Initial ray-impedance models with different ray-parameter values at (a) 0.05 s/km, (b) 0.2 s/km and (c) the acoustic impedance model.....	101
<b>Figure 4.5</b> Ray impedance inversion results with different ray-parameter values at (a) 0.05 s/km and (b) 0.2 s/km. (c) The inverted acoustic impedance. ....	102
<b>Figure 4.6</b> Ray impedance inversion results (red curves) compared with the initial models (blue curves) and the synthetic values from the well-logs (black curves). (a) – (c) are corresponding to (a) – (c) in previous Figures 4.4 - 4.5.....	103
<b>Figure 4.7</b> Bivariate probability density functions for different facies. (a) Clean sand. (b) Cemented sand. (c) Silty sand (type 1, oil-bearing). (d) Silty sand (type 2, oil-free). (e) Shale. (f) Silty shale.....	105
<b>Figure 4.8</b> Joint crossplot of oil-bearing sand and oil-free sand (generated from well logs). The solid line denotes where the discriminant values equal zero to separate these two facies. ....	106
<b>Figure 4.9</b> (a) Crossplot of the inverted ray impedance values versus acoustic impedance values for the cap-rock (blue) and the reservoir sand (green). (b) Distributions after projecting the crossplot along the main axis (black line in a). ....	107
<b>Figure 4.10</b> Impedance inversion results and seismic lithofacies prediction (a) above and (b) below the Top Heimdal horizon. ....	108
<b>Figure 4.11</b> (a) Common angle stack, (b) initial EI model and (c) inverted impedance profile for EI inversion at 29 degrees. ....	110
<b>Figure 4.12</b> (a) Crossplot of the inverted elastic impedance values versus acoustic impedance values for the cap-rock (blue) and the reservoir sand (green). (b) Distributions after projecting the crossplot along the main axis (black line in a). ....	111
<b>Figure 5.1</b> Three well logs (black) overlain with the elastic models (red) which are low-pass filtered version of real well logs for (a) P-wave velocity, (b) S-wave velocity and (c) density.....	118
<b>Figure 5.2</b> Synthetic noise-free ray impedance traces indicating ray impedance values varying with ray parameters.....	118
<b>Figure 5.3</b> Elastic inversion results for (a) P-wave velocity, (b) S-wave velocity and (c) density from the noise free ray impedance traces in Figure 5.2. ....	119
<b>Figure 5.4</b> Eigenvalue analysis for elastic parameter inversion from noise-free ray impedance traces. (a) The eigenvalue curves corresponding to the three elastic parameters. (b) The condition number curve. ....	120
<b>Figure 5.5</b> Synthetic noisy ray impedance profile with two percent random noise added.....	120

<b>Figure 5.6</b> Elastic parameter inversion results from noisy ray impedance traces for (a) P-wave velocity, (b) S-wave velocity and (c) density. Red: true model. Black solid: Inverted. Black dashed: initial model. ....	123
<b>Figure 5.7</b> Eigenvalue analysis for elastic parameter inversion from noisy ray impedance profiles. (a) The eigenvalue curves corresponding to the three elastic parameters. (b) The condition number curve. ....	124
<b>Figure 5.8</b> Convergence curve of the three-parameter inversion from noisy data....	124
<b>Figure 5.9</b> The relative standard deviation curves for the three updating estimates in the last iteration of (a) P-wave velocity, (b) S-wave velocity and (c) density...	125
<b>Figure 5.10</b> The resolution analysis for this linearised inversion in the last iteration. The three resolution curves are for (a) P-wave velocity, (b) S-wave velocity and (c) density.....	126
<b>Figure 5.11</b> Elastic inversion results for (a) P-impedance and (b) S-impedance from noisy ray impedance traces. Red: true model. Black solid: Inverted. Black dashed: initial model. ....	128
<b>Figure 5.12</b> Eigenvalue analysis for two-parameter elastic inversion from noisy ray impedance traces. (a) The eigenvalue curves corresponding to the two elastic parameters. (b) The condition number curve. ....	128
<b>Figure 5.13</b> Convergence curve of the two-parameter inversion from noisy data....	129
<b>Figure 5.14</b> The relative standard deviations for the two updating estimates in the last iteration of (a) P-impedance and (b) S-impedance. ....	129
<b>Figure 5.15</b> The resolution analysis for the two-parameter inversion in the last iteration. The two resolution curves are for (a) P-impedance and (b) S-impedance. ....	130
<b>Figure 5.16</b> Ray impedance inversion results at different ray parameter values: (a) 0, (b) 0.05, (c) 0.1, (d) 0.15 and (e) 0.2 s/km. ....	131
<b>Figure 5.17</b> Elastic inversion results for (a) P-impedance and (b) S-impedance.....	132
<b>Figure 5.18</b> The normalised convergence curve for the real data inversion. ....	132
<b>Figure 5.19</b> Comparison between the inverted attributes at CDP 2232 and the well logs for (a) P-impedance and (b) S-impedance.....	133
<b>Figure 5.20</b> (a) Eigenvalue and (b) condition number analyses at CDP 2232 for the two-parameter elastic parameter inversion. ....	133
<b>Figure 5.21</b> The uncertainty analyses for (a) P-impedance and (b) S-impedance and the resolution analyses for (c) P-impedance and (d) S-impedance at CDP 2232. ....	134
<b>Figure 5.22</b> (a) Crossplot of the inverted S-impedance versus P-impedance values for the cap-rock (blue) and the reservoir sand (green). (b) Distributions after projecting the crossplot along the main axis (black line in a).....	135
<b>Figure 6.1</b> (a) The P-P-wave stack section for the tight gas sand reservoir across the well CX560. (b) The corresponding P-S-wave stack section. ....	139
<b>Figure 6.2</b> Well log portions within the target reservoir area from the well CX560. ....	140
<b>Figure 6.3</b> (a) Correlation between the well logs (Figure 6.2) and the P-P seismic stack section shown in Figure 6.1a. (b) Well-tie applied to the P-S stack section of Figure 6.1b. The correlation coefficients are 0.8213 and 0.7532. ....	141
<b>Figure 6.4</b> P-S reflection coefficient comparisons between the pseudo quadratic expression (6.1) and the Aki and Richards linearised approximation with the exact values from Zoeppritz equations. (a)-(e) correspond to the five examples described in section 1.2.....	143
<b>Figure 6.5</b> Variation of $\kappa$ over a portion of the well logs shown in Figure 6.2. ....	145

<b>Figure 6.6</b> Synthetic traces using (from left to right) Zoeppritz equations, converted ray impedances and shear elastic impedances. ....	146
<b>Figure 6.7</b> (a) The reference P-P stack section. (b) The registered P-S stack by matching interpreted horizons. (c) The final P-S stack matched to P-P time through iterative inversion. ....	149
<b>Figure 6.8</b> (a) Correlation coefficient comparison performed at each CDP location between the initial matching result (red) and the final matching result (blue). (b) The amplitude spectra of the P-P data (grey), the P-S data before (red) and after (blue) the final registration.....	150
<b>Figure 6.9</b> Warping P-S time functions corresponding to P-P time leading to the final registered P-S image in Figure 6.6c. ....	151
<b>Figure 6.10</b> Estimated P to S velocity ratio from (a) the initial match using interpreted horizons and (b) the updated match after the iterative inversion.....	152
<b>Figure 6.11</b> Inversion results (red) compared with well log synthetics (black). (a) Ray impedance at $p = 0.1s/km$ , (b) P-impedance and (c) S-impedance. ....	153
<b>Figure 6.12</b> Inversion results for the whole line (a) Ray impedance at $p = 0.1s/km$ , (b) P-impedance and (c) S-impedance.....	154
<b>Figure 6.13</b> Converted ray impedance inversion result. ....	156
<b>Figure 6.14</b> Converted ray impedance at $p = 0.1s/km$ compared with well log derived synthetics.....	156
<b>Figure 6.15</b> (a) Crossplot between RI ( $p = 0.1s/km$ ) and AI. (b) Crossplot between CRI ( $p = 0.1s/km$ ) and AI.....	157



# Glossary

AI	acoustic impedance
AVA	amplitude versus angle
AVO	amplitude versus offset
CDF	cumulative distribution function
CIP	common image point
CMP	common mid point
CRI	converted-wave ray impedance
EI	elastic impedance
GLI	generalised linear inversion
HOS	high-order statistics
IID	independent, identically distributed
MAP	maximum a posteriori
PDF	probability density function
QC	quality control
RI	ray impedance
RMS	root mean square
SEI	shear-wave elastic impedance
SVD	singular value decomposition
TWT	two-way traveltime
VSP	vertical seismic profile



## List of Symbols

Throughout this thesis, I use the convention that upper case bold face lettering designates a matrix, lower case bold face lettering designates a vector and a scalar is italicized. Estimates are denoted with the symbol  $\hat{\cdot}$  over the variable and averages with a bar over them. Summarised below, for the readers' convenience, are the symbols used in this thesis and the order is capital letters first, then lower case followed by Greek letters.

<b>A</b>	augmented matrix
<i>AI</i>	acoustic impedance
<i>ARI</i>	acoustic ray impedance
<i>B</i>	bandwidth
<b>C<sub>d</sub></b>	data misfit covariance matrix
<b>C<sub>m</sub></b>	model covariance matrix
<b>C<sub>w</sub></b>	the convolution matrix
<i>EI</i>	elastic impedance
<i>ERI</i>	elastic ray impedance
<b>F</b>	Fréchet derivatives matrix or Jacobian matrix
<i>H</i>	Hilbert transform
<b>I</b>	unit matrix
<i>I<sub>p</sub></i>	P-wave impedance
<i>I<sub>s</sub></i>	S-wave impedance
<i>J</i>	objective function in inversion
<i>K</i>	square of the ratio between S-wave velocity and P-wave velocity
<i>L</i>	size of a region involved in computation
<i>P(x)</i>	cumulative distribution function
<b>P</b>	diagonal matrix defined as Wang (2003b)
<i>Q</i>	negative log-likelihood function

$RI$  ray impedance  
 $\mathbf{RI}$  ray impedance vector  
 $\mathbf{RI}_0$  initial ray impedance vector  
 $R_f$  fluid-fluid reflectivity  
 $R_{pp}$  or  $R$  P-P wave reflectivity  
 $R_{ps}$  P-S wave reflectivity  
 $S$  ray path  
 $T$  seismic travel time for P-P wave  
 $T_{ps}$  seismic travel time for P-S converted wave  
 $\mathbf{W}_d$  covariance matrix of data  
 $\mathbf{W}_m$  covariance matrix of model  
 $\mathbf{X}$  replicate matrix  
 $a(\tau_1, \tau_2, \tau_3)$  3D window function  
 $c(t)$  composite trace  
 $c_k^x$   $k$ -th order cumulant of signal  $x$   
 $\hat{c}_k^x$  estimation of  $c_k^x$   
 $d$  seismic data  
 $\mathbf{d}$  seismic data vector  
 $\mathbf{e}$  residual vector in least-squares problem  
 $f_0$  central frequency  
 $k$  kurtosis  
 $m$  constant  
 $\mathbf{m}$  model vector  
 $\mathbf{m}_0$  initial model vector  
 $m_k^x$  the  $k$ -th order moment of signal  $x$   
 $\hat{m}_k^x$  estimation of  $m_k^x$   
 $\tilde{m}_n^w$  windowed  $n$ -order cumulant from the seismic trace (approximate the  $n$ -order moment of the wavelet)  
 $n$  noise  
 $p$  ray parameter (horizontal slowness)



$\bar{p}$  average horizontal slowness  
 $p(x)$  probability density function of a random variable  $x$   
 $p(\mathbf{d})$  probability density function of a vector  $\mathbf{d}$   
 $q$  effective length of a wavelet  
 $q_\alpha$  P-wave vertical slowness  
 $q_\beta$  S-wave vertical slowness  
 $v$  medium velocity  
 $\mathbf{r}$  reflection coefficient vector  
 $r(\theta)$  angle-dependant reflection coefficient  
 $s$  ray path segment  
 $\mathbf{t}_d$  vector of time derivatives  
 $u$  slowness  
 $w$  wavelet  
 $\mathbf{w}$  wavelet in vector form  
 $\Delta\mathbf{w}$  wavelet updating vector  
 $x$  a random variable or horizontal coordinate  
 $x(t)$  a signal or a seismic trace  
 $x_0$  location parameter in Cauchy distribution  
 $\mathbf{x}_d$  vector of space derivatives  
 $\mathbf{z}$  impedance vector  
 $\mathbf{z}_0$  initial impedance value vector  
 $\alpha$  P-waved velocity  
 $\mathbf{a}$  P-wave velocity vector  
 $\alpha_0$  P-wave velocity constant  
 $\mathbf{a}_0$  initial P-wave velocity vector  
 $\bar{\alpha}$  average P-wave velocity  
 $\beta$  S-wave velocity  
 $\mathbf{\beta}$  S-wave velocity vector  
 $\beta_0$  S-wave velocity constant  
 $\mathbf{\beta}_0$  initial S-wave velocity vector

$\delta \mathbf{d}$	data residual vector
$\delta \mathbf{m}$	model updating vector
$\varepsilon$	data misfit
$\kappa$	exponential term in converted ray impedance
$\varphi$	converted S-wave angle
$\gamma$	angle of seismic ray at the surface
$\gamma_k^r$	$k$ th order reflectivity cumulant
$\eta$	pre-whitening or balancing parameter in least squares inversion
$\lambda$	Cauchy distribution parameter
$\hat{\lambda}$	Cauchy distribution parameter solved based on the statistical information of the whole seismic section
$\mu$	shear modulus
$\theta$	P-wave incidence angle
$\rho$	density
$\mathbf{\rho}$	density vector
$\rho_0$	density constant
$\mathbf{\rho}_0$	initial density vector
$\sigma$	standard deviation
$\tau$	time lag
$\nu$	ratio between the relative change of density and S-wave velocity across an interface $((\Delta\rho/\rho)/(\Delta\beta/\beta))$
$\psi$	warp function in matching P-S events to P-P events

# **Chapter 1**

## **Introduction**

With the development of modern geophysics, geoscientists and engineers are not satisfied merely with geological structure interpretation after seismic data processing and imaging. What they need is the quantitative information about rock properties and fluid parameters, which can be interpreted and utilised by a team of geologists, geophysicists and reservoir engineers. Seismic impedance inversion is such a technique that can be used in reservoir characterization. This technique is best performed by combining data of all types, not only seismic but also well log, petrophysics and geological prior information.

Acoustic impedance and elastic impedance are important physical properties as well as powerful tools in seismic inversion. Their presence in the oil and gas exploration has facilitated us in making enormous successful discoveries. Elastic impedance is derived from a linear approximation of the Zoeppritz equations. Strictly speaking, acoustic impedance is a particular case of elastic impedance when the seismic incidence angle is zero. In this thesis, I will use the concept of seismic ray impedance, proposed by Wang (2003a) and derived from a different approximation of the Zoeppritz equations. The ray impedance can be classified as a sort of generalised elastic impedance. Here “generalised” indicates that the elastic impedance is a combination of P-wave velocity, S-wave velocity and density, similar to the conventional elastic impedance which is defined by Connolly (1999).

### **1.1 From acoustic impedance to elastic impedance**

Acoustic impedance (AI), which was usually computed from post-stack seismic data, is a simple but powerful tool in seismic interpretation and many other seismic

applications. Considering a discrete earth model, the P-wave reflection coefficient,  $R$ , for normal incidence, at an interface between the layer number  $k$  and  $k + 1$  is given by

$$R_k = \frac{AI_{k+1} - AI_k}{AI_{k+1} + AI_k}, \quad (1.1)$$

where  $AI_k$  and  $AI_{k+1}$  are the acoustic impedances above and below the interface,

$$AI_i = \rho_i \alpha_i, \quad (1.2)$$

and  $\rho_i$  and  $\alpha_i$  denote the density and P-wave velocity at the incident side ( $i = k$ ) and at the opposite side ( $i = k + 1$ ) of the reflecting interface. Re-arranging equation (1.1), one may compute the acoustic impedance using the following recursive formula as

$$AI_{k+1} = AI_k \frac{1 + R_k}{1 - R_k}. \quad (1.3)$$

By successive applications of equation (1.3), one obtains a nonlinear expression as

$$AI_{k+1} = AI_1 \prod_{j=1}^k \frac{1 + R_j}{1 - R_j}, \quad (1.4)$$

which relates the acoustic impedance  $AI_{k+1}$  to the reflection coefficients. In equation (1.4) we assume that the acoustic impedance  $AI_1$  in the first layer is known.  $AI$  calculated using equation (1.4) is usually called the pseudo-logging method.

In expression (1.3), if we take the following approximations

$$e^{R_k} \approx 1 + R_k, \quad e^{-R_k} \approx 1 - R_k, \quad (1.5)$$

we may derive another recursive formula as

$$AI_{k+1} = AI_1 \exp\left(2 \sum_{j=1}^k R_j\right). \quad (1.6)$$

Comparison of the two different recursive formulae for the computation of the acoustic impedance is made by expanding both of them in Taylor series. From equation (1.3), we have

$$\frac{AI_{k+1}}{AI_k} = \frac{1 + R_k}{1 - R_k} = 1 + 2 \sum_{n=1}^{+\infty} R_k^n = 1 + 2R_k + 2R_k^2 + 2R_k^3 + \dots, \quad (1.7)$$

and for equation (1.6) one has

$$\frac{AI_{k+1}}{AI_k} = \exp(2R_k) = \sum_{n=0}^{+\infty} \frac{2^n}{n!} R_k^n = 1 + 2R_k + 2R_k^2 + \frac{4}{3} R_k^3 + \dots. \quad (1.8)$$

We can see that the two expressions are equivalent up to the second order approximation of  $R_k$ .

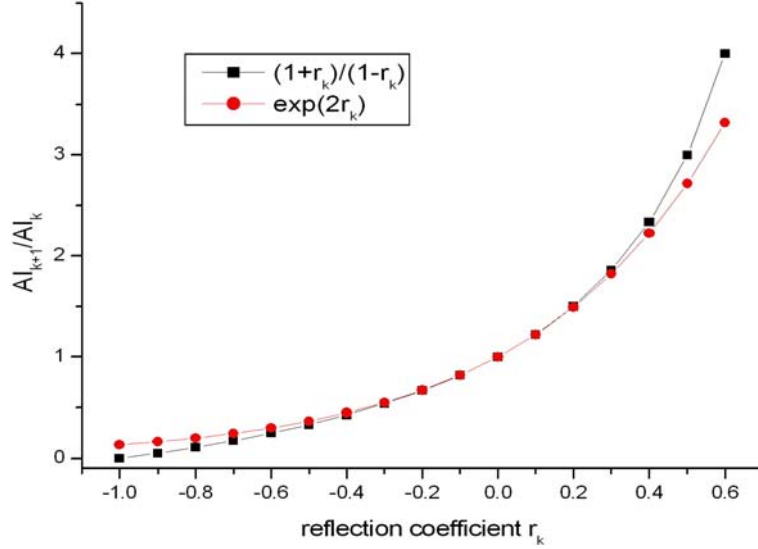


**Figure 1.1** Graphical differences between equation (1.7) and equation (1.8).

Figure 1.1 shows a graphical comparison of the two recursive formulae. The difference between the two expressions is less than 5 percent for  $|R_k| \leq 0.4$ . However, for reflection coefficients with large positive values, the exponential formula is less sensitive to noise. Although the theoretical value of reflection coefficient is usually less than 0.3, the reflection coefficient series derived from a real seismic trace may sometime contain large coefficient values, due to the effects such as data noise and data processing errors or artefacts. In this case, computation using the exponential formula will be more stable.

In the case of non-normal incidence in acoustic media, where the shear wave velocity is assumed to be zero, the corresponding reflection coefficient can be written in a similar form

$$R_k = \frac{AI_{k+1} \sec \theta_{k+1} - AI_k \sec \theta_k}{AI_{k+1} \sec \theta_{k+1} + AI_k \sec \theta_k}, \quad (1.9)$$

where  $\theta_k$  is the incidence angle and  $\theta_{k+1}$  is the transmission angle. Equation (1.9) makes the acoustic impedance applicable to prestack seismic data. By comparison with hydrocarbon detection methods, such as amplitude-versus-offset (AVO) or

amplitude-versus-angle (AVA) analysis, conventional acoustic impedance seems uncompetitive since another important medium parameter, S-wave velocity, is neglected, as well as many equivalent combinations of P-wave velocity, S-wave velocity and density, such as shear modulus, bulk modulus, Poisson's ratio, which are very important indicators for a hydrocarbon reservoir. In order to incorporate these factors in oil and gas detection, many efforts have been made. Among them the derivation of elastic impedance is a brilliant and successful attempt.

Elastic impedance (EI), defined on variable incidence angles, is a generalisation of acoustic impedance (Connolly, 1999). The EI provides a consistent and absolute framework to calibrate and invert nonzero-offset seismic data just as AI does for zero-offset data. EI is derived from a linearisation of the Zoeppritz equations as follows,

$$R(\theta) = A + B \sin^2 \theta + C \sin^2 \theta \tan^2 \theta, \quad (1.10)$$

with

$$A = \frac{1}{2} \left( \frac{\Delta \alpha}{\alpha} + \frac{\Delta \rho}{\rho} \right),$$

$$B = \frac{\Delta \alpha}{2\alpha} - 4 \frac{\beta^2}{\alpha^2} \frac{\Delta \beta}{\beta} - 2 \frac{\beta^2}{\alpha^2} \frac{\Delta \rho}{\rho}$$

$$\text{and } C = \frac{1}{2} \frac{\Delta \alpha}{\alpha}$$

where  $\Delta \alpha$  and  $\alpha$  are the difference and average of the P-wave velocities at either side of the interface

$$\alpha = (\alpha_{k+1} + \alpha_k) / 2,$$

$$\Delta \alpha = \alpha_{k+1} - \alpha_k$$

(similarly,  $\Delta \beta$  and  $\beta$  of the S-wave velocity, and  $\Delta \rho$  and  $\rho$  of the density) and

$$\frac{\beta^2}{\alpha^2} = \left( \frac{\beta_{k+1}^2}{\alpha_{k+1}^2} + \frac{\beta_k^2}{\alpha_k^2} \right) / 2.$$

EI is defined such that the reflection coefficient variation with angle can be derived from the formula analogous to the acoustic reflectivity

$$R_k(\theta) = \frac{EI_{k+1}(\theta) - EI_k(\theta)}{EI_{k+1}(\theta) + EI_k(\theta)}. \quad (1.11)$$

This involves the use of the approximate log derivation for reflection coefficient at a certain interface which is accurate to the second order

$$R(\theta) \approx \frac{1}{2} \frac{\Delta EI(\theta)}{EI(\theta)} \approx \frac{1}{2} \Delta \ln(EI(\theta)). \quad (1.12)$$

By combining equation (1.10) and equation (1.12), substituting  $K$  for  $\beta^2/\alpha^2$ , and rearranging the equation we get

$$\frac{1}{2} \Delta \ln(EI(\theta)) = \frac{1}{2} \left( \frac{\Delta \alpha}{\alpha} (1 + \tan^2 \theta) - \frac{\Delta \beta}{\beta} 8K \sin^2 \theta + \frac{\Delta \rho}{\rho} (1 - 4K \sin^2 \theta) \right). \quad (1.13)$$

Using the differential equivalent of logarithm function again, equation (1.13) is reformed as

$$\Delta \ln(EI(\theta)) = (1 + \tan^2 \theta) \Delta \ln \alpha - 8K \sin^2 \theta \Delta \ln \beta + (1 - 4K \sin^2 \theta) \Delta \ln \rho. \quad (1.14)$$

Assuming  $K$  is a constant, integrating equation (1.13) and setting the integration constant to zero, we have

$$EI(\theta) = \alpha^{(1+\tan^2 \theta)} \beta^{-8K \sin^2 \theta} \rho^{(1-4K \sin^2 \theta)}. \quad (1.15)$$

An undesirable feature of the EI function (1.15) has been that its dimensionality varies with incidence angles. Whitcombe (2002) overcame these problems by normalising the EI function with constants  $\alpha_0$ ,  $\beta_0$  and  $\rho_0$  (equation 1.16). These modifications do not change the accuracy of the reflectivity expression that can be derived from the EI function.

$$EI(\theta) = \alpha_0 \rho_0 \left[ \left( \frac{\alpha}{\alpha_0} \right)^{(1+\tan^2 \theta)} \left( \frac{\beta}{\beta_0} \right)^{-8K \sin^2 \theta} \left( \frac{\rho}{\rho_0} \right)^{(1-4K \sin^2 \theta)} \right] \quad (1.16)$$

EI is a function of P-wave velocity, S-wave velocity, density and incidence angle. To relate EI to seismic data, there must be some form of angle stacks rather than stacks with different offsets. Furthermore EI inversion is closely related to AVO/AVA analysis, which has been proved to be a powerful tool in up-to-date petroleum exploration.

## 1.2 Seismic ray impedance

EI is a successful attempt to relate elastic medium parameters to prestack seismic data by utilising the linear approximation (1.10) of the Zoeppritz equations. From EI, the inversion of S-wave velocity is possible, which is very important for detecting hydrocarbons. But from the derivation of EI, there are two major assumptions which make it inaccurate. First, the incidence and the transmitted angle are assumed to be identical, which is not correct by violating Snell's law, and secondly the parameter  $K = \beta^2 / \alpha^2$  remains a constant when we integrate equation (1.14) to obtain (1.15), which is not true in most real cases.

There is another sort of simplification of the Zoeppritz equations which leaves the ray parameter value unchanged across an interface, following Snell's law strictly. The simple approximation to the P-wave reflection coefficient proposed by Mallick (1993) is such an attempt and Wang (1999) not only provided a different way of deriving this reflection coefficient for a P-P wave but also extended the derivation to the P-P transmission coefficient and the coefficients of converted wave reflection and transmission.

Wang (2003a) further mathematically proposed the concept of ray impedance (RI) for P-P waves which honours Snell's law. Consider a horizontal interface separating two elastic media, in which the P-wave velocities are  $\alpha_1$  and  $\alpha_2$ , the S-wave velocities are  $\beta_1$  and  $\beta_2$  and the densities are  $\rho_1$  and  $\rho_2$ . Seismic ray impedance is derived from the truncated quadratic approximation of the P-P wave reflection coefficient (Wang, 1999) as

$$R_{pp}(p) \approx R_f(p) - \frac{2\Delta\mu}{\rho} p^2, \quad (1.17)$$

where  $p$  is the ray parameter,  $\Delta\mu = \mu_2 - \mu_1 = \rho_2\beta_2^2 - \rho_1\beta_1^2$  is the difference of the shear moduli, and

$$R_f(p) = \frac{\rho_2 q_{\alpha_1} - \rho_1 q_{\alpha_2}}{\rho_2 q_{\alpha_1} + \rho_1 q_{\alpha_2}}, \quad (1.18)$$

in which  $q_{\alpha_1}$  and  $q_{\alpha_2}$  are the vertical slownesses.



Similar to the derivation of EI from the linear approximation (1.10) of the Zoeppritz equations, we require the RI function to have analogous properties to EI, such that reflectivity can be derived from the following formula for a ray parameter value  $p$  :

$$R_{pp}(p) = \frac{RI_{i+1}(p) - RI_i(p)}{RI_{i+1}(p) + RI_i(p)} \approx \frac{1}{2} \ln \frac{RI_{i+1}(p)}{RI_i(p)}, \quad (1.19)$$

which leads to the definition of RI expressed as (Wang, 2003a)

$$RI(\alpha, \beta, \rho, p) = \frac{\rho\alpha}{\sqrt{1-\alpha^2 p^2}} (1 - \beta^2 p^2)^{2(\nu+2)} = \frac{\rho\alpha}{\cos\theta} \left(1 - \frac{\beta^2}{\alpha^2} \sin^2 \theta\right)^{2(\nu+2)}. \quad (1.20)$$

The detail derivation is summarized in Appendix 1.A. In equation (1.20),  $\nu$  is defined by

$$\nu = (\Delta\rho/\rho)/(\Delta\beta/\beta),$$

which is the ratio between the relevant changes of density and S-wave velocity. Notice that even the second expression in (1.20) is adopted, Snell's law is still honoured as the angle value is changing according to

$$p = \frac{\sin \theta}{\alpha}$$

at different sides of the interface.

Unlike EI, RI naturally has the dimensionality of impedance, which is velocity multiplied by density. Thus we do not need normalisation in using RI. We can also observe from (1.20) that, when ray parameter  $p = 0$ , RI will degenerate into AI, just as EI does when the angle  $\theta$  equals zero.

### 1.3 Evaluation of $\nu$ value in RI

The value of  $\nu$  should be calculated according to the local petrophysical environment. A very straightforward thought is to utilise those values directly calculated from well log data at each depth point in the well. However there are two considerations preventing us from using  $\nu$  calculated in such a manner: first, when dealing with

geophysical problems to a seismic scale, we care more about the macro effects regarding geological formations rather than the very high frequency variations changing at every several centimetres as they are beyond the discriminability of seismic data; secondly, the denominator of  $\nu$ ,  $\Delta\beta/\beta$  will be zero when the S-wave velocities are the same at adjacent logging points, which makes the calculation of  $\nu$  unstable.

A practical solution in obtaining  $\nu$  value is through discovering the relationship between density and S-wave velocity first and then calculating  $\nu$  value from the relationship. From the experimental research of Potter et al. (1998), we assume that a similar Gardner's relationship (Gardner et al., 1974) exists between S-wave velocity and density as

$$\rho = c\beta^b. \quad (1.21)$$

The parameters  $c$  and  $b$  can be determined through a linear regression of well data if we write equation (1.21) into

$$\log \rho = \log c + b \log \beta. \quad (1.22)$$

The linear regression of (1.22) is commonly used in petrophysical and geophysical analysis.

The relation expressed in equation (1.21) is observed from a real producing well in the North Sea, which is attached to a seismic dataset that will be used and introduced later in this thesis. Figure 1.2 shows five well logs available for our analysis from an oil-producing well in the Glitne field in the North Sea. These well logs are used to demonstrate several case studies in *Quantitative Seismic Interpretation* (Avseth et al., 2005). There are six formations identified from the well logs which are labelled on the right in Figure 1.2. They are, from top to bottom, shale, silty shale, clean sand, silty sand group 1, silty sand group 2 and cemented sand. The oil reservoir is located in the formations of clean sand and silty sand 1.

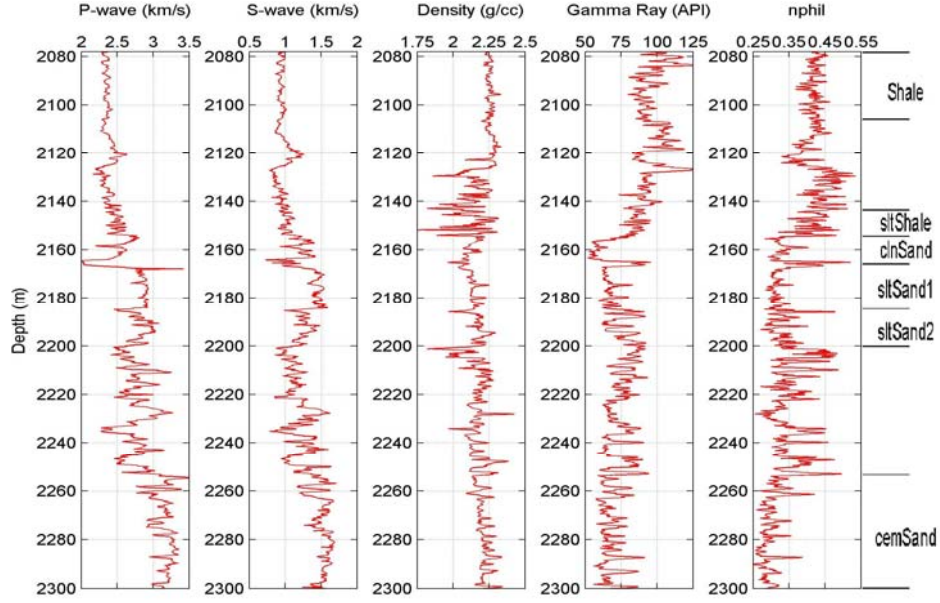


**Figure 1.2** Five well logs from a producing gas well in the North Sea.

The linear regressions between  $\log \rho$  and  $\log \beta$  in different formations are plotted in Figure 1.3, (a) - (f) are corresponding to the six identified formations from top to bottom in Figure 1.2. The units for velocity and density are  $km/s$  and  $g/cm^3$ , respectively. From the results of the linear regressions, we can identify the values of  $c$  and  $b$ , and thus the  $\nu$  values for the six formations are calculated according to:

$$\Delta \rho = cb\beta^{b-1}\Delta \beta,$$

$$\frac{\Delta \rho}{\rho} = b \frac{\Delta \beta}{\beta},$$

$$\nu = (\Delta \rho / \rho) / (\Delta \beta / \beta) = b,$$

which are listed as follows:

$$0.098, 0.010, 0.049, 0.012, -0.008, 0.048.$$

It will be shown later in 1.4 that for such small  $\nu$  values compared to 2 (see the exponential term in 1.20), the difference is neglectable and will not lead to lithology identification failure if we only use a single  $\nu$  value (0.07 in this case) calculated for all the six formations.

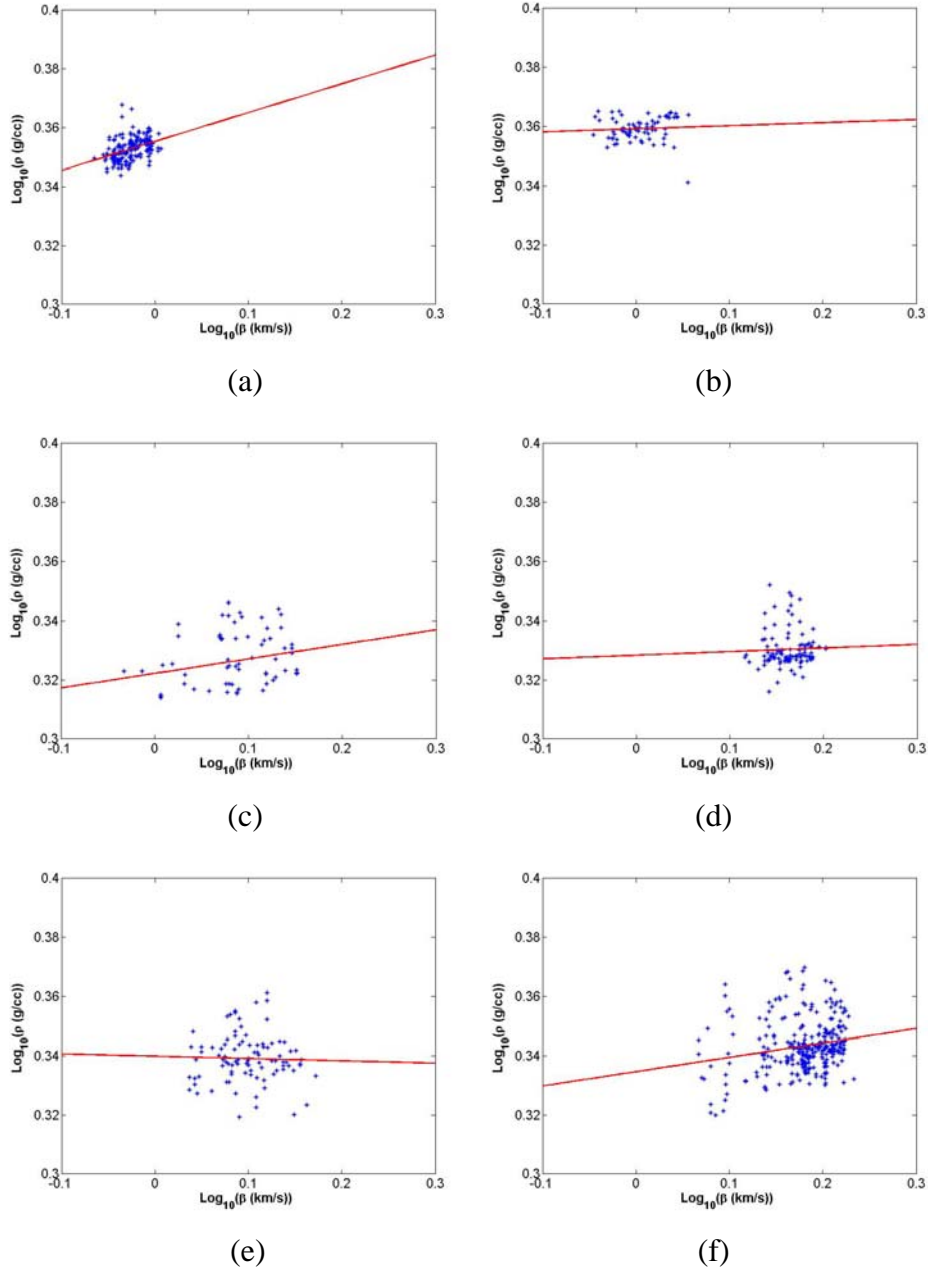


**Figure 1.3** Linear regressions of  $\log \rho$  (vertical axis) and  $\log \beta$  (horizontal axis) in different formations to identify the Gardner's type of relationship between density and S-wave velocity. (a) - (f) are corresponding to the six formations in the well shown in Figure 1.2, from top to bottom respectively.

#### 1.4 Comparison between RI and EI in identifying lithology

The quadratic expression denoted by Mallick (1993) and Wang (1999) is much more accurate than any linear approximation of the Zoeppritz equations (Mallick, 1993 and

Wang, 1999). However, as (1.17) is a truncated version of the quadratic approximation, it is necessary to compare the accuracy of (1.17) with (1.10) first. This comparison is shown in Figure 1.4, using the exact reflection coefficient values calculated from the Zoeppritz equations for reference. The same five examples demonstrated in Mallick (1993) are employed here to generate these figures. In all these examples below,  $\alpha_1$ ,  $\beta_1$  and  $\rho_1$  denote the P-wave velocity, S-wave velocity and density respectively, for the medium above a reflecting interface, whereas  $\alpha_2$ ,  $\beta_2$  and  $\rho_2$  stand for the same quantities for the medium below the reflecting interface. The comparison is restricted to non-evanescent P-waves only as both equation (1.17) and (1.10) are valid only in the non-evanescent regime.

The first example is for a model with

$$\alpha_1 = 2307m/s, \beta_1 = 942m/s, \rho_1 = 2.15g/cm^3,$$

$$\alpha_2 = 1951m/s, \beta_2 = 1301m/s \text{ and } \rho_2 = 1.95g/cm^3,$$

which is corresponding to an interface between shale and Class-3 type gas sand (Rutherford and Williams, 1989). Example two is for a model with

$$\alpha_1 = 2307m/s, \beta_1 = 1538m/s, \rho_1 = 2.15g/cm^3,$$

$$\alpha_2 = 2500m/s, \beta_2 = 1021m/s \text{ and } \rho_2 = 2.2g/cm^3,$$

representing an interface between gas sand and shale. Example three is for

$$\alpha_1 = 2400m/s, \beta_1 = 980m/s, \rho_1 = 2.2g/cm^3,$$

$$\alpha_2 = 2550m/s, \beta_2 = 1755m/s \text{ and } \rho_2 = 2.0g/cm^3,$$

which is representative of shale and Class-2 type gas sand reflection (Rutherford and Williams, 1989). Example four is also a representative interface between shale and Class-2 type gas sand defined by Rutherford and Williams (1989), with

$$\alpha_1 = 2400m/s, \beta_1 = 980m/s, \rho_1 = 2.2g/cm^3,$$

$$\alpha_2 = 2700m/s, \beta_2 = 1858m/s \text{ and } \rho_2 = 2g/cm^3.$$

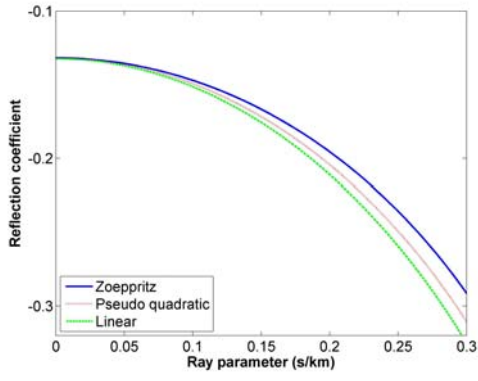
The last example denotes shale and Class-1 type gas sand reflection (Rutherford and Williams, 1989), with

$$\alpha_1 = 2350m/s, \beta_1 = 959m/s, \rho_1 = 2.2g/cm^3,$$

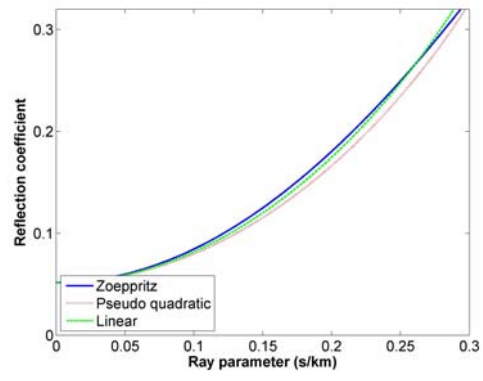
$$\alpha_2 = 2730m/s, \beta_2 = 1879m/s \text{ and } \rho_2 = 2.15g/cm^3.$$

The five comparisons with the above examples are plotted in Figure 1.4 (a) – (e). The angle value in (1.10) is converted to ray parameter using the average velocity of both layers. From these comparisons we can find that generally the truncated quadratic equation (1.17) is slightly more accurate than the linear approximation (1.10). Now the question is whether this improvement in accuracy can be carried into inversion.

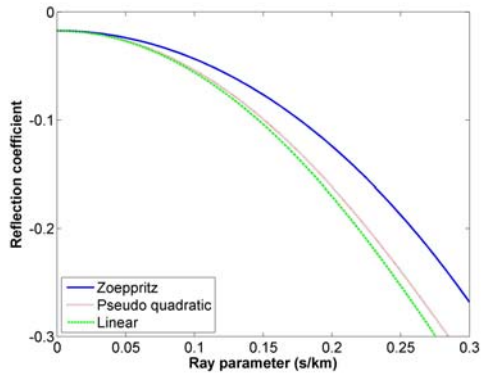
Figure 1.5a compares the synthetic traces generated from the Zoeppritz equations (index 1) and from RI values (index 2) using (1.19) at ray parameter 0.21s/km, by convolving a Ricker wavelet (dominant frequency 20Hz) with both sets of reflectivity series obtained from the well partly shown in Figure 1.2 (the original length is about 400m). This record is about 0.5s in duration representing the whole available well logs which are partially shown in Figure 1.2. Figure 1.5b is a similar comparison between the synthetic traces generated from the Zoeppritz equations (index 1) and EI values at 30° (index 2), which is equivalent to a ray parameter value of 0.21s/km calculated from  $p = \sin 30^\circ / \bar{\alpha}$ , where  $\bar{\alpha}$  is the average P-wave velocity of this area, 2.4 km/s. As the Zoeppritz equations are originally defined on ray parameter values, the angle value 30° is converted to the corresponding ray parameter value at each layer in Figure 1.5b, in order to have an accurate comparison between the two synthetic traces. The correlation coefficient between the two traces in Figure 1.5a is 0.97 and 0.92 for Figure 1.5b, indicating that RI can correlate prestack seismic data more accurately with subsurface elastic parameters.



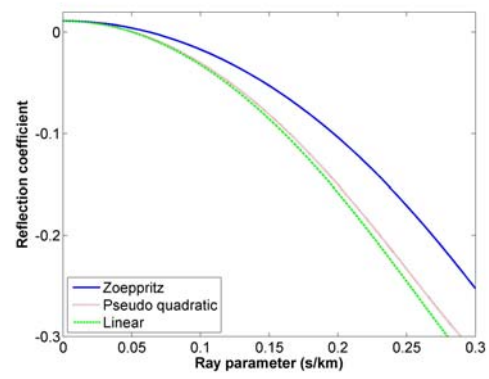
(a)



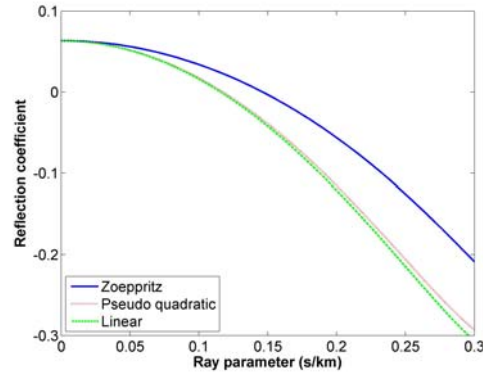
(b)



(c)



(d)



(e)

**Figure 1.4** P-wave reflection coefficient comparisons between the quadratic expression (1.17) and the linear expression (1.10), using the exact values for reference. (a)-(e) are corresponding to the five examples described in the context.

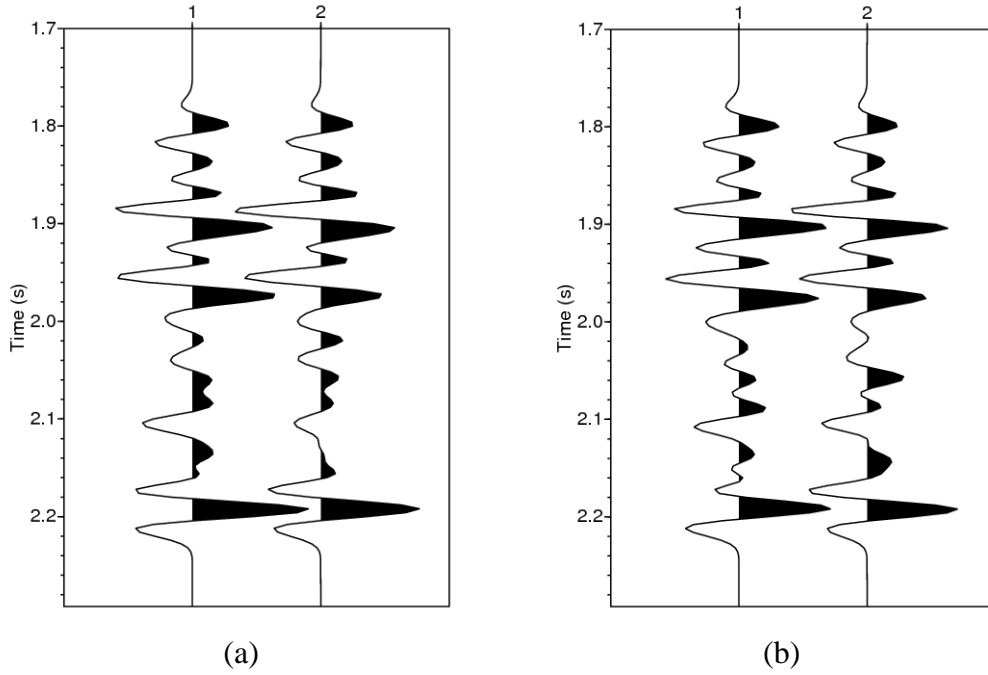


**Figure 1.5** Comparison between the accuracy of the synthetic traces generated from RI and EI. (a) Synthetic traces generated from the Zoeppritz equations (index 1) and from RI values (index 2) at ray parameter 0.21s/km. (b) Synthetic traces generated from the Zoeppritz equations (index 1) and from EI values (index 2) at 30°.

For the capability of RI in classifying and identifying different lithological properties, the crossplots of EI and RI versus AI are compared in Figure 1.6: (a) is the crossplot between the normalised EI at 30 degrees and the AI for the six formations displayed in Figure 1.2, while (b) crossplots the RI at  $p = 0.21s/km$  and the AI. The  $\nu$  value used in calculating the RI in Figure 1.6b, 0.07 (i.e.  $2(\nu + 2) \approx 4.14$ , the exponent in 1.20), is determined by a linear regression between the logarithms of all the S-wave velocity and density values from 2100m and 2300m along the well shown in Figure 1.2. The normalised elastic impedance values are calculated when we set the angle value to be 30° (for the same reason in Figure 1.5). The black lines denote the main axis that projection will be made later.

For comparison, we also crossplot in Figure 1.6c the RI versus the AI using the six different  $\nu$  values calculated in section 1.3. It is nearly identical to the crossplot in Figure 1.6b. In this case, where the value of  $\nu$  is much smaller than 2 and hence the exponential term in expression (1.20) is mainly determined by the constant part rather



than the  $\nu$ . This phenomenon can also be generally explained as the density variations are normally much smaller than the variations of velocity. As a consequence, it is reasonable to choose a unique  $\nu$  value when we do modelling or inversion regarding RI in similar geological formations.

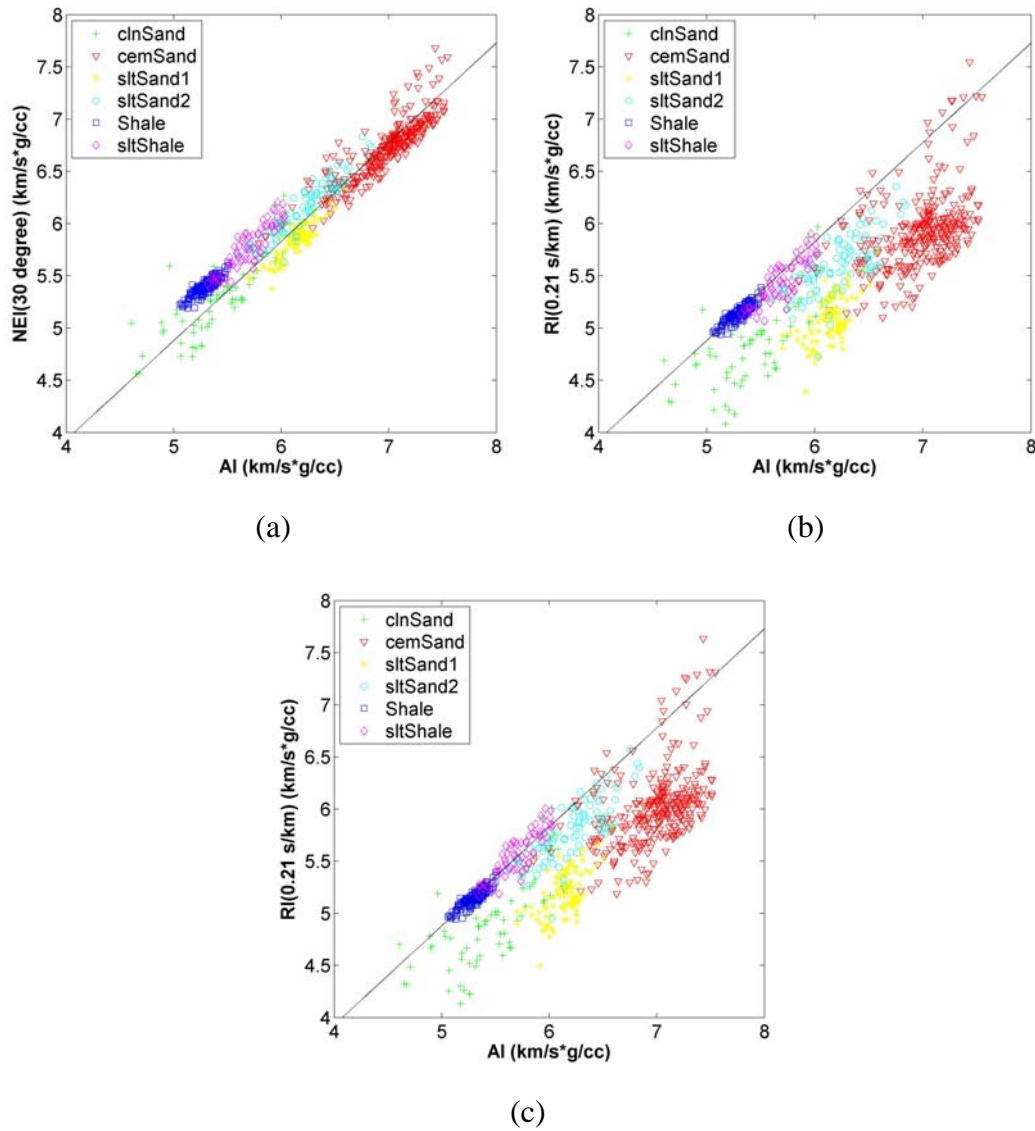


**Figure 1.6** Crossplots of (a) normalised EI(30), (b) RI( $p = 0.21$ ) with a unique  $\nu$  value for different lithologies and (c) RI( $p = 0.21$ ) using different  $\nu$  values for different lithologies, versus AI. The black lines denote the main axis.

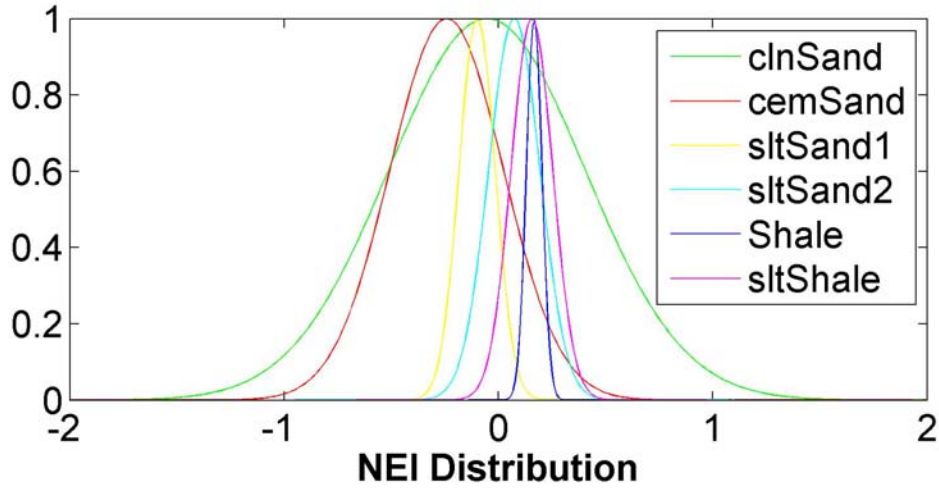
From the crossplot between EI(30) and AI, we can observe that the relationship between EI and AI distributions of different lithologies are nearly linear with the same slope and intercept. This means that using the crossplot in Figure 1.6a is similarly

difficult to separate different lithologies which we can not achieve by using AI only. Meanwhile, as the RI values here are not correlated to the AI values by a similar relationship for all formations, the crossplot of Figure 1.6b or 1.6c between RI and AI values makes it easier for us to discern different lithologies.

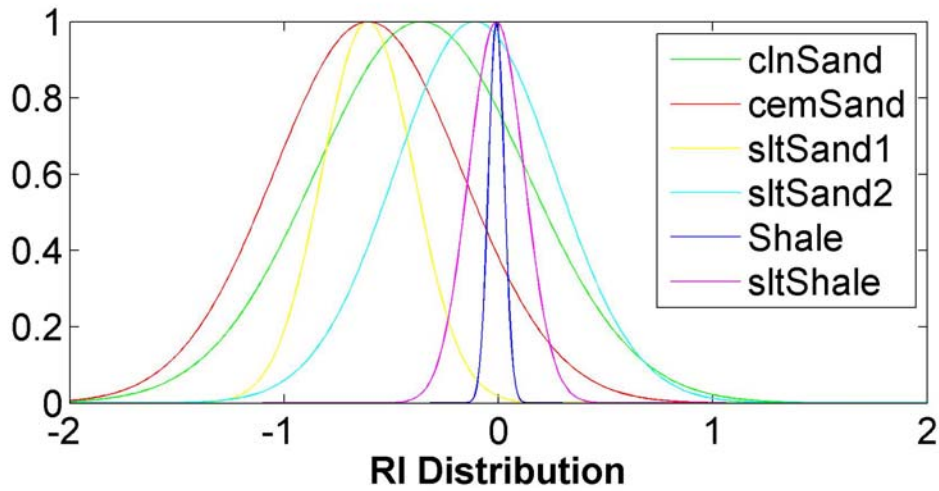
Figure 1.7 displays the distributions of the cross-plotted data in Figure 1.6a and 1.6b in projection along the main axis (black lines in Figure 1.6). The distribution for each facies is fitted by a smoothed Gaussian curve which is normalised to 1. The parameters for these Gaussian curves are listed in Table 1.1, where  $M$  and  $\sigma$  denotes the mean and the standard deviation of a Gaussian distribution respectively. From this table we can find that the RI-AI crossplots for five facies (except the Shale) are stretched when projecting along the main axis. However, using silty shale (cap rock) for reference, the means of 4 out of the other 5 facies departs the mean of silty shale more rapidly than their standard deviations stretch, especially for the two oil-bearing formations (clean sand and silty sand 1). This means that using RI-AI crossplots will facilitate us more in discriminating oil-bearing formations from capping rocks.

	clnSand	cemSand	sltSand1	sltSand2	Shale	sltShale
$\sigma$ (EI)	0.457	0.264	0.084	0.119	0.036	0.097
$M$ (EI)	-0.054	-0.242	-0.010	0.074	0.167	0.156
$\sigma$ (RI)	0.494	0.439	0.214	0.374	0.036	0.129
$M$ (RI)	-0.361	-0.608	-0.609	-0.111	-0.010	-0.010
$\sigma$ (RI)- $\sigma$ (EI)	0.037	0.175	0.130	0.255	0.000	0.032
$ M(RI,sltShale)-M(RI) $ - $ M(EI,sltShale)-(M(EI)) $	0.141	0.200	0.433	0.019	0.011	0.000

**Table 1.1** Gaussian parameters when projecting the crossplots in Figure 1.6 along the main axis.



(a)



(b)

**Figure 1.7** Smoothed Gaussian distributions for different facies when projecting their crossplots in Figure 1.6 along the main axis for (a) normalised EI(30), (b) RI( $p = 0.21$ ).

### 1.5 Construction of constant ray-parameter profiles

Traditional AVO analysis is carried out on the offset domain CMP gathers and can only qualitatively identify the amplitude variation along the offset axis. Afterwards geophysicists managed to transform CMP gathers from the offset domain to the angle domain which leads to the development of AVA methods for quantitative modelling and inversion analysis. Compared with inverting multi-offset data through fitting elastic wavefield, e.g. Mora (1987, 1988), which is very computing intensive,

traditional AVA analysis or inversion is much faster with acceptable accuracy since they are based on convolutional trace assumption. This evolution also makes the EI inversion possible as EI is defined on angle values.

When Connolly (1999) proposed the concept of EI, two methods of constructing angle stacks were mentioned to relate prestack seismic data to EI. Similar to this procedure, as RI is defined on ray parameters, methods of generating constant ray-parameter profiles need to be pointed out for the future inversion study. In the following section, I clarify different methods to transform CMP gathers from the offset domain to the ray-parameter domain. Then the constant ray-parameter profile, whose amplitudes are related to a specific ray-parameter value, can be extracted from the transformed CMP gathers in the ray-parameter domain.

### **1.5.1 Tau-p transform on CMP gathers**

Probably the most straightforward method is the tau-p transform which can transfer the seismic traveltimes data from the time-space domain to the instantaneous-slope and intercept-time domain. It has been widely employed in seismic processing, e.g. multiple attenuation and the removal of coherent noise. The instantaneous-slope contains the ray parameter information needed for RI inversion.

For common source/receiver geometry, the instantaneous slope of the traveltimes data represents the true horizontal ray parameter  $p$ , and the intercept time is the sum of the thickness multiplied by the vertical slowness along a seismic ray, referenced to the fixed surface station. However we intend to carry out the tau-p transform on CMP gathers for the sake of convenience, since all the reflections along the same hyperbola come from the same reflecting point when the subsurface structure is flat, whereas this is not true for a common source/receiver gather. This practice is also consistent to those in classical AVO modelling and inversion, as well as in EI inversion. It is shown that the instantaneous slope in CMP gathers is the average slowness of upgoing and downgoing rays at the surface, and the intercept time is the sum of thickness and vertical slowness products, but referenced to the common mid point (Diebold and Stoffa, 1981). A simple verification of the statement, that for reflections

from a flat reflector the instantaneous slope in CMP gathers is equal to the horizontal slowness of the seismic ray, is detailed in Appendix 1.B.

For CMP gathers from dipping structures, the average horizontal slowness is no longer equal to the ray parameter value related to the incidence angle. See Figure 1.8 for example,  $\gamma_1$  and  $\gamma_2$  are the two angles that are related to the horizontal slownesses,  $\theta$  is the incidence/reflection angle that is related to the ray parameter value denoted by RI and  $\gamma$  is the dip angle. Under this circumstance, the calculated instantaneous slope from CMP gathers, which is the average of the two horizontal slownesses related to  $\gamma_1$  and  $\gamma_2$ , is only an approximation to the ray parameter value related to the angle  $\theta$ . This ray parameter value is indeed the parameter indicated by the Zoeppritz equations and the one that our inversion should deal with.

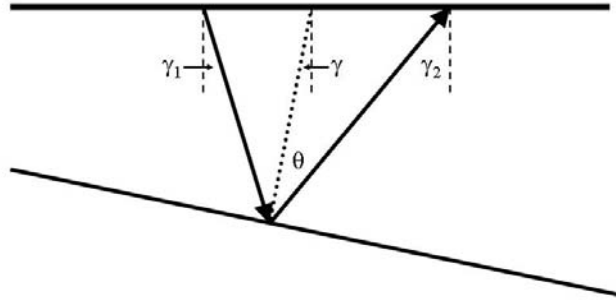


**Figure 1.8** A dipping geometry for a CMP gather

From simple trigonometry we find that

$$\gamma = \frac{1}{2}(\gamma_1 + \gamma_2) \text{ and } \theta = \frac{1}{2}(\gamma_2 - \gamma_1). \quad (1.23)$$

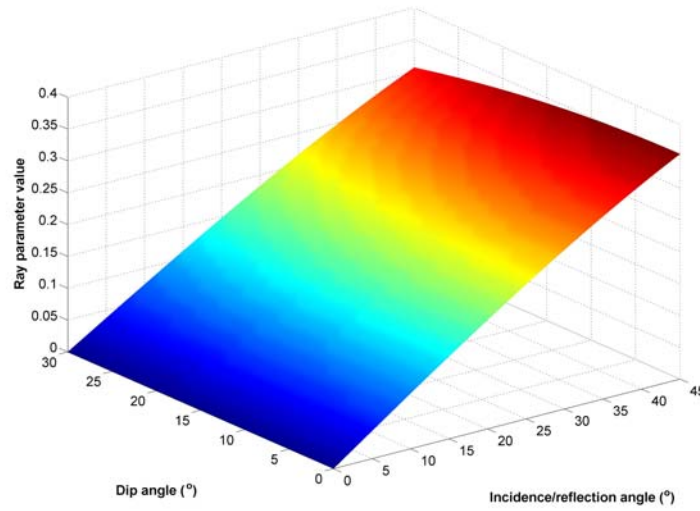
Please note that here  $\gamma_1$  and  $\gamma_2$  have opposite signs in the geometry shown in Figure 1.8. The average horizontal slowness

$$\bar{p} = \frac{1}{2\alpha} [\sin \gamma_2 + \sin(-\gamma_1)] = \frac{1}{\alpha} \cos \gamma \sin \theta \quad (1.24)$$

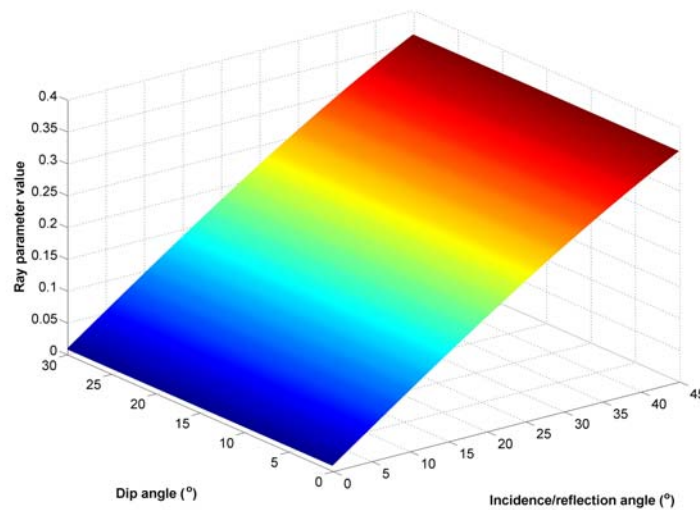
is different from the incidence ray parameter value ( $\frac{\sin \theta}{\alpha}$ ) by a factor of  $\cos \gamma$ .

Figure 1.9 compares the average horizontal slownesses and the incidence ray parameter values for different dip angles, assuming the medium velocity

$\alpha = 2000m/s$  . This approximation is acceptable for the dip angle up to  $30^\circ$  when the incidence angle is smaller than  $45^\circ$  .



(a)



(b)

**Figure 1.9** Comparison of (a) average horizontal slownesses and (b) striking ray parameter values as functions of dip angles and incidence angles.

RI inversion, similar to AVO and EI inversion, is highly dependent on the relative amplitude variations of seismic data, so that a full 3D processing is preferable. However when the data acquisition is restricted to 2D surveys, it is necessary to compensate the seismic data amplitude by simulating a 3D processing when we carry out the processing for inversion purposes. For the tau-p transform, Wapenaar et al.

(1992) integrated the amplitude compensation into the tau-p transform via a Fourier-Hankel transform (Treitel et al., 1982), followed by an inverse Fourier transform. This process is also known as a cylindrical slant stack, or the tau-p transform from point-sources to line-sources. The significant assumption in this technique is the cylindrical symmetry around the source point which limits the application to simple media only. Although this method is first developed for the tau-p transform of shot gathers, it is also valid when applied to CMP gathers, by assuming that the cylindrical symmetry is referenced to the mid point. Figure 1.10a shows a synthetic CMP gather composed of hyperbolas and (b) is the result after the above point-source tau-p transform.

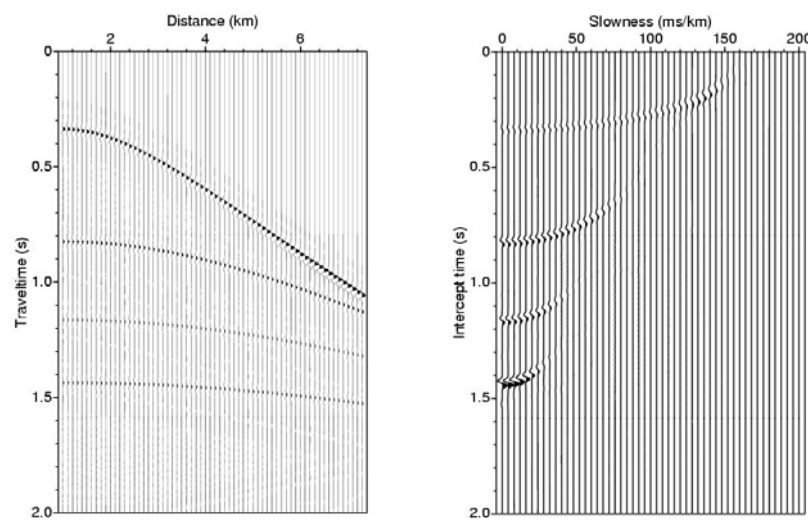


**Figure 1.10** (a) A synthetic CMP gather composed of hyperbolas. (b) The corresponding point-source tau-p transform result.

Although we have the horizontal slowness information after the tau-p transform, the intercept time needs to be transferred to zero-offset traveltime to ensure the ray-parameter dependent amplitudes coming from the same reflector will line up at the same time position. This is not difficult to achieve when the velocity information is available, since the transformed tau-p domain data are stacks of constant velocity only and the semi-axial lengths of each ellipse are both related to interval velocity. However seismic data after tau-p transform are not suitable for further amplitude related analysis directly as the relative amplitude is altered during the slant stack processing. This can be observed from Figure 1.10: The strongest reflection appears on the bottom event of the transformed data (Figure 1.10b), which is fairly weak on

the original CMP gather (Figure 1.10a). This is attributed to the different numbers of wavelets involved in the slant stack for different slopes. Before we put the tau-p transformed data into inversion usage, a calibration should be carried out using synthetic traces from well logs.

### 1.5.2 CMP gathers mapped using local slope

The slant stack method is demonstrated to be unsuitable for direct amplitude related analysis. However it is a heuristic for us because it tells us that the horizontal slowness is related to the local slope of traveltime hyperbolas. If we can find a way of mapping, rather than stacking, to transfer the data from the offset domain to the ray parameter domain, then the relative amplitude information will be preserved. The plane-wave destruction filters introduced by Claerbout (1992) and improved by Fomel (2002) can help us to achieve this objective.

The so-called plane-wave destruction filters introduced by Claerbout (1992) can be employed to calculate the local slope via a local-coherence analysis. In a small window, the data variations along the time and the spatial axis are approximated through a finite-difference scheme. The slope value is then computed by

$$p = -\frac{\mathbf{t}_d \cdot \mathbf{t}_d}{\mathbf{x}_d \cdot \mathbf{t}_d}$$

where  $\mathbf{t}_d$  and  $\mathbf{x}_d$  are vectors formed by time derivatives and spatial derivatives of the windowed data. Since only one slope value can be calculated within each window, we need to repeat this process at each discrete sample point to produce a slope field first and then map the data from the time-space domain to the time-ray parameter domain. Using this scheme, we will be in a dilemma that, on the one hand the coherence analysis requires more data within the window to generate an accurate slope value, while on the other hand a large window will not lead to a local solution.

Fomel (2002) introduced another approach toward the finite difference scheme for increasing the accuracy and dip bandwidth of Claerbout's method (1992). The plane-wave destruction filters are designed using the z-transform technique and local windows are no longer necessary because the slope is estimated as a continuous function of the data coordinates. This slope function is smoothly variable by adding a



regularisation to avoid oscillatory local slope estimates in regions with unknown or constant data since the local slope is not constrained in these regions. Once the slope values are estimated, the prestack seismic data can be mapped from the time-space domain into the time-ray parameter domain in a CMP gather.

### **1.5.3 Ray-parameter domain common image point gathers**

For CMP gathers generated from flat geological structures, all the reflections come from the same horizontal location. Under this circumstance, a constant ray-parameter profile extracted from the ray-parameter domain CMP gathers reveals the reflection amplitudes at a certain ray-parameter value with the same horizontal locations. It might be taken as granted that migration is not necessary in areas where the sedimentary structures are flat, but actually it should be applied whenever it is possible as the diffractions at the target area will be collapsed to be smaller than the Fresnel zone and as a consequence to improve the lateral resolution (Avseth, et al., 2005). Whereas for seismic data coming from complex subsurface structures, the constant ray-parameter profiles built from the unmigrated CMP gathers will no longer tell us the true reflection positions and hence the migration processing is even more necessary.

For AVA analysis and elastic impedance inversion, angle domain common-image-point (CIP) gathers are needed. De Bruin et al. (1990) first described a method for calculating angle-dependent reflectivity within a wave-equation migration process. In their algorithm, angle gathers are evaluated using slant stacks of the downward-continued wavefield prior to imaging, and are functions of horizontal slowness instead of the ray parameter related to the true reflection angle. Rickett and Sava (2002) and Sava and Fomel (2003) presented improved approaches for extracting true angle-domain CIP gathers during wavefield continuation migration. This kind of angle domain CIP gathers can also be produced by Kirchhoff migration (Xu et al., 2001).

Generally speaking, prestack time migration is preferred to prestack depth migration as the former tends to perform better in preserving amplitudes (Avseth, 2005). However, in areas with complicated geology, prestack depth migration remains the most accurate tool and an amplitude-preserving prestack depth migration algorithm should be applied (Zhang, 2007).

Generally CIP gathers generated by the wavefield continuation migration algorithm are images in the depth domain. However most AVO analysis and elastic inversion are carried out in the time domain since an obvious disadvantage in the depth domain is that even stationary wavelets in the time domain will be stretched or compressed in the depth domain.

#### 1.5.4 Ray tracing in offset domain CIP gathers

Nowadays Kirchhoff prestack time migration is still a prevalent imaging technique and its product is usually the offset domain CIP gathers, which form the majority of the data available to us. In order to apply the offset domain CIP gathers to ray impedance inversion, we have to transform these CIP gathers from the offset domain to the ray-parameter domain. Here we adopt a ray tracing algorithm to implement this transform. The principle is: each reflection event at a certain time with a certain offset in the offset domain CIP gather, is mapped in the ray-parameter domain CIP gather at the same time but with a corresponding ray parameter.

There are many ray tracing methods and considering both efficiency and accuracy I adopt here the one commonly used in seismic tomography which is called the bending ray tracing method (see for instance, Wang, 2003a p.17-19). According to Fermat's principle, the actual ray path is the one (denoted by  $S$ ) which minimises the travel time  $T$ , given by

$$\min T(S) = \int_s \frac{ds}{\alpha}, \quad (1.25)$$

where  $s$  stands for the ray arc-length so that  $ds$  is the length of the ray segment. Within each CIP gather after migration, the velocity field is assumed to only change along the depth direction and the ray-path under consideration can be discretized into a polygonal path with unique small depth interval (Figure 1.11),

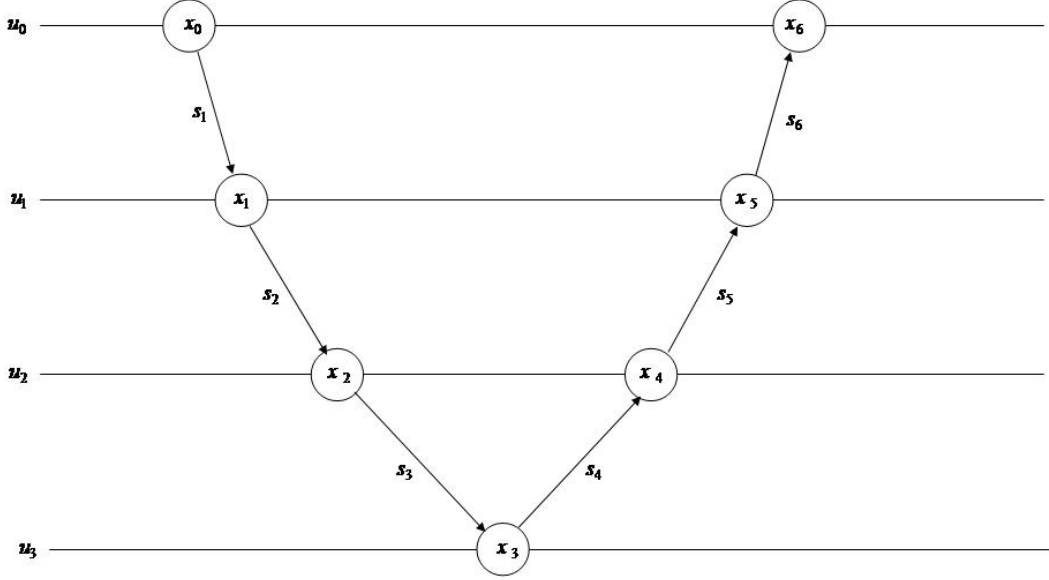


**Figure 1.11** Schematic illustration of the bending ray method ( $k = 3$ ).

$$S = \{x_0, x_1, \dots, x_k, \dots, x_{2k}\}, \quad (1.26)$$

where each  $x$  stands for the horizontal coordinate of each reflector at each CIP position. The traveltimes can then be expressed explicitly as

$$T = \frac{1}{2} \sum_{i=1}^{2k} (u_{i-1} + u_i) ds_i, \quad (1.27)$$

where  $u_i = 1/\alpha_i$  is the P-wave slowness and  $u_i = u_{2k-i}$ . For ray tracing, we may consider  $x_k$  as the reflection point, and the endpoints,  $x_0$  and  $x_{2k}$ , of the ray path are fixed. Fermat's principle can then be expressed as

$$\nabla_S(S) = 0 \quad (1.28)$$

which states that seismic energy travels along a path for which the first-order variation with all neighbouring paths is zero.

Under the assumption of locally flat reflectors within migrated CIP gathers, equation (1.28) can be differentiated to give

$$\frac{\partial T}{\partial x_i} = \frac{1}{2} \left[ \frac{(u_i + u_{i+1})}{ds_{i+1}} (x_i - x_{i+1}) + \frac{(u_i + u_{i-1})}{ds_i} (x_i - x_{i-1}) \right], \text{ for } i = 1, \dots, 2k-1. \quad (1.29)$$

Using a second order accurate representation of the derivatives, equation (1.28) gives a tri-diagonal linear equation system

$$\begin{pmatrix} \frac{u_0+u_1}{s_1} + \frac{u_1+u_2}{s_2} & -\frac{u_1+u_2}{s_2} & 0 & \dots & 0 \\ -\frac{u_1+u_2}{s_2} & \frac{u_1+u_2}{s_2} + \frac{u_2+u_3}{s_3} & -\frac{u_2+u_3}{s_3} & \ddots & \vdots \\ 0 & \ddots & \ddots & \ddots & 0 \\ \vdots & \ddots & -\frac{u_3+u_2}{s_{2k-2}} & \frac{u_{2k-3}+u_{2k-2}}{s_{2k-2}} + \frac{u_{2k-2}+u_{2k-1}}{s_{2k-1}} & -\frac{u_{2k-2}+u_{2k-1}}{s_{2k-1}} \\ 0 & \dots & 0 & -\frac{u_{2k-2}+u_{2k-1}}{s_{2k-1}} & \frac{u_{2k-2}+u_{2k-1}}{s_{2k-1}} + \frac{u_{2k-1}+u_{2k}}{s_{2k}} \end{pmatrix}$$

$$\cdot \begin{pmatrix} x_1 \\ x_2 \\ \vdots \\ x_{2k-2} \\ x_{2k-1} \end{pmatrix} = \begin{pmatrix} \frac{u_0+u_1}{s_1} x_0 \\ 0 \\ \vdots \\ 0 \\ \frac{u_{2k-1}+u_{2k}}{s_{2k}} x_{2k} \end{pmatrix} \quad (1.30)$$

with unknowns  $\{x_i\}$ , which can be solved iteratively. As we assumed that the CIP gathers after migration are locally flat which means at each common image point the medium becomes 1D, the slowness variables are symmetric following  $u_i = u_{2k-i}$ , for  $i = 0, \dots, 2k$ .

Figure 1.12 shows a synthetic test illustrating the bending ray-tracing procedure. There is a three layer 1D medium with P-wave velocities equal to 1500m/s, 3000m/s and 5000m/s, from top to bottom respectively. This model depicts a simple background velocity field employed in the bending ray-tracing scheme at a CIP position under the assumption of local flatness. Imagine there is a reflection event coming from the bottom of this model recorded by the receiver whose offset equals 975m. In order to map this reflection event to its corresponding position in a ray-parameter domain CIP gather, we have to calculate its ray path first and then its ray parameter value. The green dotted line is the initial ray path in the bending ray tracing scheme which usually consists of two straight lines from the shot to the reflection point and from the reflection point to the receiver. The solid black line is the true ray path for the specified reflection event and the yellow dashed line indicates the resultant ray path after 5 iterations. The stopping criterion in this iterative process is

set such that the summation of the absolute changes for all the ray segments is less than a threshold which is set to be  $10^{-4}$  of the maximum offset in my test.

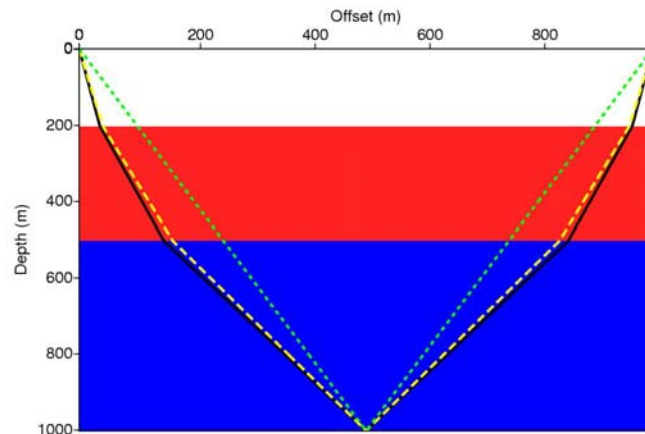


**Figure 1.12** Synthetic example of bending ray tracing method for a P-P wave.

This velocity field used in this ray tracing scheme can be constructed from local well logs or seismic tomography inversion, either travel time or waveform inversion. Because of the limited resolution of tomography and the sparse availability of well logs, a smooth velocity model is normally used for this ray tracing. This has a certain theoretical background in that ray tracing is based upon a short wave-length (high frequency) approximation. Also from a practical perspective, rapid variations in the velocity field can cause seismic rays to be refracted at or beyond the critical angle, which make the ray tracing algorithm unstable. In this thesis, the velocity fields for ray tracing are constructed from well logs by extrapolating the low-pass filtered velocity information along picked geological horizons.

## 1.6 The dataset for demonstration in the thesis

Throughout this thesis, there are two datasets involved. The first North Sea one is adopted from Chapter 2 to Chapter 5 and the inclusive well data have already been used in section 1.3 and 1.4. In this section, I will introduce this North Sea dataset solely and the other one, which consists both P-P and P-S waves, will only be used and depicted in Chapter 6.

The North Sea dataset comes from the book *Quantitative Seismic Interpretation* (Avseth et al., 2005), where it is employed to demonstrate several case studies.

Prestack seismic data from a 2D line are available from the Glitne Field, a turbidite reservoir of Tertiary age, located in the South Viking graben in the North Sea. A stacked section from CDP 2000 to 2400 is displayed in Figure 1.13 and a producing well was drilled at CDP 2232 which has already been displayed in Figure 1.2.

This dataset was processed by the processing team in Norsk Hydro back in 1994, for true amplitude recovery aiming at the ensuing AVO analysis. The work flow includes the following main steps: spherical divergence correction, prestack FK time migration, Radon-transform multiple removal, and surface consistent offset balancing. According to the information in Avseth et al. (2005), I have interpreted three horizons around the producing area, which are the top of the Balder formation, the top of the Heimdal formation and the top of the Chalk formation, respectively from top to bottom in Figure 1.13, where the black curves denotes the well position. These horizons will be used to confine the window in the inversion and also as reference positions in identifying geological formations. Oil has been encountered just below the top of the Heimdal horizon in a reservoir of about 30 meters in thickness.

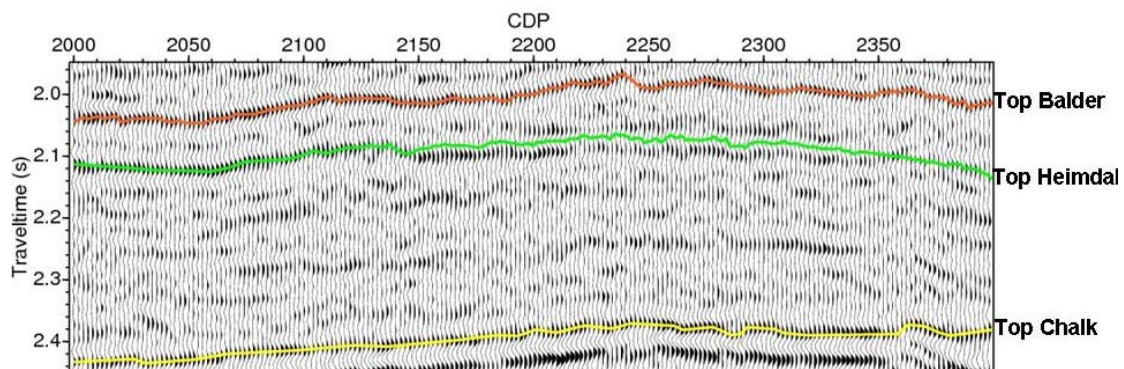


**Figure 1.13** The stack section of a turbidite reservoir of Tertiary age in the North Sea with geological horizons and well log.

## 1.7 Overview of this thesis

The main purpose of this thesis is to demonstrate the practical application of ray impedance inversion and elastic parameter inversion through ray impedance. The flowchart for the whole process of P-P waves is shown in Figure 1.14. A similar flow for the ray impedance inversion of P-S waves is followed in Chapter 6, which also includes a joint analysis of the inversion results from both waves.

In the preparation stage, prestack seismic data available to us for ray impedance inversion are normally processed by the third party and all in the form of offset-domain CIP gathers. Considering this nature of the data and the available techniques, these CIP gathers are transformed from the offset domain into the ray-parameter domain through the bending ray-tracing algorithm, as summarised in section 1.5.4. Then constant ray-parameter profiles are constructed by partially stacking the CIP gathers and form the input of mixed-phase wavelet estimation and seismic reflectivity inversion.

In Chapter 2, I will deal with the wavelet issue which is essential in most inversion procedures as well as seismic processing. I advocate a practical workflow starting from the mixed-phase wavelet estimation based on the high-order statistics (HOS), which can preserve the phase information of signals. The estimated wavelets through HOS are used in the well-to-seismic tie and can be further refined after the well is correlated to the seismic. Furthermore, the conditions of using HOS are documented and also discussed in this chapter.

A quantitative Cauchy-constraint reflectivity inversion is presented in Chapter 3, after the wavelets are extracted. This technique can reduce the ambiguity in choosing the parameter controlling the sparseness of the reflectivity inversion result, as the quality of seismic reflectivity sequences will directly affect the blocky impedance inversion results. The Cauchy-constraint reflectivity inversion results are further improved in bandwidth by a data merging technique in the frequency domain with the least-squares reflectivity deconvolution results.

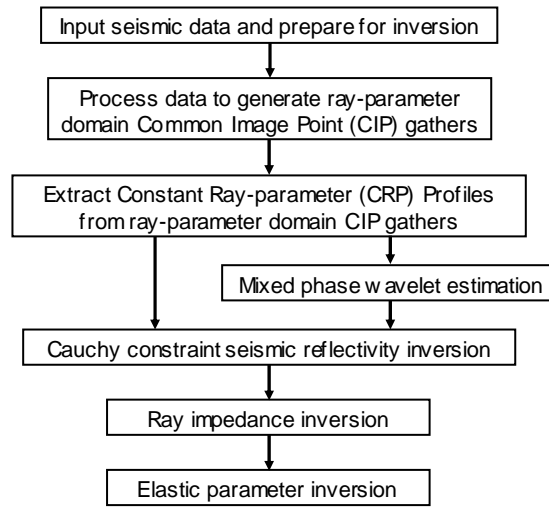


**Figure 1.14** Flowchart of the inversion procedure in this thesis.

After prestack seismic data are inverted into sparse seismic reflectivity sequences regarding different ray parameters, the generalised linear inversion (Cooke and Schneider, 1983), which is originally deployed to invert AI from post stack data, is applied to each reflectivity profile with a specific ray parameter value. The inversion results are utilised to identify rock properties and facilitate quantitative interpretation. This technique is also adopted in the EI inversion, and the results from RI and EI inversion are compared in terms of the ability to separate oil-bearing sand and cap rock in an example from the North Sea.

It has also been demonstrated in Chapter 5 that we can further invert elastic parameters from ray impedance values. A stable inversion for P- and S-wave impedance directly from ray impedance is accomplished together with resolution analysis. Compared with those conventional schemes, which normally utilise the linear approximation of the Zoeppritz equations, our scheme does not eliminate the density term nor introduce a Gardner's relation to absorb this term, which makes it theoretically more accurate than the conventional schemes, provided the inverted ray impedance profiles are accurate.

In Chapter 6, a joint analysis of the inversion results from P-P and P-S wave data is carried out in the common ray-parameter domain after the ray impedance inversion is



implemented for both waves. This incurs another novel definition of converted-wave ray impedance. It will be demonstrated that the converted-wave ray impedance is a good link connecting prestack converted-wave data with well logs. To register corresponding events of P-P and P-S waves, I make a practical approach through a least-squares inversion scheme which integrates the horizon interpretation results to form an initial match. This joint analysis is carried out on a multicomponent dataset from southwestern China, representing a tight gas sand reservoir.

The final conclusion and future work are summarised in Chapter 7.

### Appendix 1.A Derivation of acoustic and elastic ray impedance

Based on the quadratic expression (1.17), the fluid-fluid term  $R_f$  (1.18) can be expressed in the recursive form:

$$\begin{aligned} R_f(p(\theta_i)) &= \frac{\alpha_{i+1}\rho_{i+1}\cos\theta_i - \alpha_i\rho_i\cos\theta_{i+1}}{\alpha_{i+1}\rho_{i+1}\cos\theta_i + \alpha_i\rho_i\cos\theta_{i+1}} \\ &\approx \frac{1}{2} \ln \left( \frac{\alpha_{i+1}\rho_{i+1}}{\cos\theta_{i+1}} \bigg/ \frac{\alpha_i\rho_i}{\cos\theta_i} \right) \end{aligned} \quad (1.A.1)$$

Note equation (1.A.1) is also the reflection coefficient expression for oblique-incidence in acoustic medium.

Since

$$\Delta\mu \approx \beta^2\Delta\rho + 2\rho\beta\Delta\beta \text{ and } p = \frac{\sin\varphi}{\beta}$$

where  $\varphi$  is the angle to relate shear wave velocity with a specified seismic ray, the second term  $-\frac{2\Delta\mu}{\rho}p^2$  in (1.17) can be expanded as

$$-\frac{2\Delta\mu}{\rho}p^2 \approx -2\left(\frac{\Delta\rho}{\rho} + \frac{2\Delta\beta}{\beta}\right)\sin^2\varphi \approx -2(\nu+2)\frac{\Delta\beta}{\beta}\tan^2\varphi \quad (1.A.2)$$

where we assume that the P-SV wave reflection angle  $\varphi$  is small and let

$$\nu = (\Delta\rho/\rho)/(\Delta\beta/\beta).$$

Following the derivation of equation (6) in Wang (1999), we further have the approximation

$$\Delta\varphi \approx \frac{\Delta\beta}{\beta} \tan \varphi$$

derived from Snell's law. Then we obtain the expressions

$$-\frac{2\Delta\mu}{\rho} p^2 \approx -2(\nu+2)\tan\varphi\Delta\varphi \approx 2(\nu+2)\frac{\Delta\cos\varphi}{\cos\varphi} \approx \frac{1}{2}\ln\frac{\cos^{4(\nu+2)}\varphi_{i+1}}{\cos^{4(\nu+2)}\varphi_i}. \quad (1.A.3)$$

Combining (1.A.1) and (1.A.3), the reflectivity in (1.17) is expressed as

$$R_{pp}(p(\theta, \varphi)) \approx \frac{1}{2} \ln \left[ \left( \alpha_{i+1} \rho_{i+1} \frac{\cos^{4(r+2)}\varphi_{i+1}}{\cos\theta_{i+1}} \right) / \left( \alpha_i \rho_i \frac{\cos^{4(r+2)}\varphi_i}{\cos\theta_i} \right) \right] \quad (1.A.4)$$

which satisfies the recursive requirement in (1.19). Comparing (1.A.4) and (1.19) we have the ray impedance expression (1.20).

#### Appendix 1.B A simple verification regarding the tau-p transform in CMP gathers

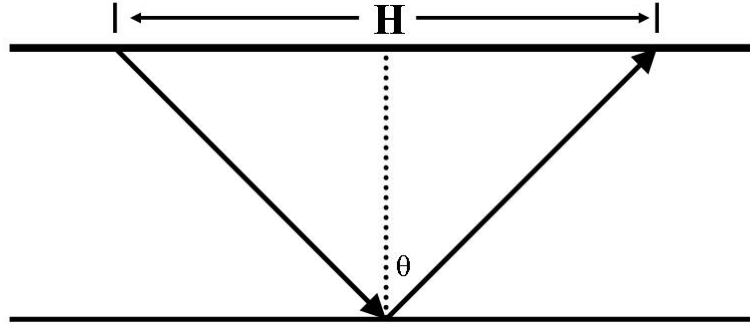


**Figure 1.15** A simple ray-path geometry for a reflection in a CMP gather.

For a reflection from a horizontal event, the geometry is shown in Figure 1.15, where  $H$  is the offset between the source and the receiver and  $\theta$  is the incidence/reflection angle, we have the following expression from trigonometry:

$$\alpha T = 2\sqrt{\left(\frac{H}{2}\right)^2 + \left(\frac{\alpha T_0}{2}\right)^2}, \quad (1.B.1)$$

where  $\alpha$  is the medium velocity,  $T$  and  $T_0$  are the two-way traveltimes for the oblique reflection and the normal reflection respectively.

From equation (1.B.1), we have the instantaneous slope

$$\frac{dT}{dH} = \frac{H}{\alpha^2 T} = \frac{\frac{H}{2}}{\frac{\alpha T}{2}} \frac{1}{\alpha} = \frac{\sin \theta}{\alpha} = p. \quad (1.B.2)$$

It means that for reflections coming from a flat event, the instantaneous slope in CMP gathers is equal to the horizontal slowness of a specific seismic ray.



## **Chapter 2**

### **Mixed-phase wavelet estimation**

#### **2.1 Introduction**

Seismic wavelet estimation is an important issue in seismic data processing and inversion since it is not always possible for us to measure the seismic wavelet directly. Moreover during the process of wave propagation, the wavelet excited by a seismic source that has a fixed amplitude and phase spectrum will alter both in amplitude and phase, and the resultant wavelet is usually mixed phase which may be fairly different to the source wavelet. The reason for alteration could be earth absorption, near surface effects, inter-bed multiples, NMO stretch or processing artefacts. With the development of modern seismic techniques, nowadays geophysics practitioners are no longer satisfied with extracting zero-phase or minimum-phase wavelets only, although they are still quite useful. In seismic inversion, only after the extraction of the mixed-phase wavelet can we have a reliable estimation of the reflectivity series.

There are two major categories of wavelet extraction methods: purely statistical and those using well logs. The former means estimating the wavelet from the seismic data alone and the latter utilises well-log information in addition to the seismic data. There are good practices for both techniques and the shortcomings for them are typical as well. Statistical methods tend to have difficulty in estimating the phase spectrum stably since real seismic data can hardly meet the strict prerequisites of using statistical information, while the well-related methods depend critically on a good tie between the seismic data and the well logs. In absence of check-shot and VSP surveys, a very common mistake occurs when we carry out the depth-to-time conversion which converts the logs sampled in depth to two-way traveltime.

In order to make use of the advantages of both methods, I advocate a practical wavelet estimation workflow integrated with a well-tie practice:

1. Calculate the amplitude spectrum from the autocorrelation of the seismic data.
2. Estimate a constant phase spectrum and then the mixed-phase wavelet using the statistical information of the seismic data.
3. Correlate the well-logs to the seismic traces.
4. Refine the wavelet by using the correlated well-logs.
5. Repeat step 3 and 4 if necessary.

This workflow is a practical solution for general exercises when the well-to-seismic correlation, which usually requires a check-shot survey, is not available.

In real seismic data, wavelets differ from trace to trace and vary with traveltime as well. This suggests that we should extract a large set of wavelets for each seismic section. However attempting to estimate variable wavelets will introduce more uncertainty than the data are able to resolve, and as a consequence, we only extract a single “average” wavelet for an entire seismic section as a common practice, i.e., the wavelet will not vary from CMP to CMP but does for different offsets.

## 2.2 High-order statistics of seismic data

Moments and cumulants are higher order covariance functions which are very useful in describing both deterministic and stochastic signals. For the sake of completeness, this section summarises the basics of high-order statistics (HOS) and their applicability for seismic signal analysis, together with the prerequisites of using the statistical wavelet estimation method.

The  $k$  th-order moment function of a real stationary discrete-time signal,  $x(t)$ , is defined as (Mendel, 1991)

$$m_k^x(\tau_1, \tau_2, \dots, \tau_{k-1}) = E\{x(t) \cdot x(t + \tau_1) \cdot \dots \cdot x(t + \tau_{k-1})\}, \quad (2.1)$$

where  $E\{\cdot\}$  denotes statistical expectation. Equation (2.1) defines the population moment, i.e. the moment from the infinite ensemble of sequences  $x(t)$ . It is a

hypothetical quantity and any sample values of the moment,  $\hat{m}_k^x$ , which is normally measured from finite data, are distinguished from population values by a superscript circumflex (and the same hereinafter).

Cumulants may be expressed through moments. The  $k$  th-order cumulant function of a real stationary process is given by (Velis and Ulrych, 1996)

$$c_k^x(\tau_1, \tau_2, \dots, \tau_{k-1}) = E\{x(t) \cdot x(t + \tau_1) \cdots x(t + \tau_{k-1})\} - E\{g(t) \cdot g(t + \tau_1) \cdots g(t + \tau_{k-1})\}, \quad (2.2)$$

where  $g(t)$  is an equivalent Gaussian process that has the same second-order statistics as  $x(t)$ . Cumulants not only display the amount of higher order correlation, but also provide a measure of the distance of the random process from Gaussian nature. For the third or higher odd order, if  $x(t)$  is Gaussian,  $c_k^x(\tau_1, \tau_2, \dots, \tau_{k-1}) = 0$ . The second-, third- and fourth-order cumulants of a zero mean  $x(t)$  is given explicitly as (Mendel, 1991)

$$c_2^x(\tau) = E\{x(t)x(t + \tau)\}, \quad (2.3)$$

$$c_3^x(\tau_1, \tau_2) = E\{x(t)x(t + \tau_1)x(t + \tau_2)\}, \quad (2.4)$$

$$\begin{aligned} c_4^x(\tau_1, \tau_2, \tau_3) = & E\{x(t)x(t + \tau_1)x(t + \tau_2)x(t + \tau_3)\} \\ & - c_2^x(\tau_1)c_2^x(\tau_2 - \tau_3) - c_2^x(\tau_2)c_2^x(\tau_3 - \tau_1) \\ & - c_2^x(\tau_3)c_2^x(\tau_1 - \tau_2). \end{aligned} \quad (2.5)$$

We shall observe that the second-order cumulant  $c_2^x(\tau)$  is just the autocorrelation of  $x(t)$  (zero-mean). This autocorrelation contains no phase information so that a non-minimum phase or non-zero phase wavelet can not be recovered from second-order statistics. The third-order cumulant is a two-dimensional function whose value at the origin is called skewness. It preserves phase information but for a symmetrically distributed (e.g. Laplace, Uniform, Gaussian), zero-mean random process, the third-order cumulant is zero. Hence, for generally zero-mean seismic data, we would not be able to use the third-order statistics to recover the phase information. The fourth-order cumulant is a three-dimensional function whose value at the origin is named kurtosis. Kurtosis is usually nonzero for most seismic data and the fourth-order cumulant has

been employed to estimate mixed-phase wavelet (e.g., Lazear, 1993, Velis and Ulrych, 1996).

Considering a convolutional seismic model

$$x(t) = w(t) * r(t) + n(t), \quad (2.6)$$

where  $w(t)$  is a seismic wavelet,  $r(t)$  is a reflectivity function,  $*$  is a convolutional operator and  $n(t)$  is a term for noise, the Bartlett-Brillinger-Rosenblatt equation (Mendel, 1991) denotes a relationship among the high-order statistics for the convolutional model is,

$$c_k^x(\tau_1, \dots, \tau_{k-1}) = c_k^r(\tau_1, \dots, \tau_{k-1}) * m_k^w(\tau_1, \dots, \tau_{k-1}) + c_k^n(\tau_1, \dots, \tau_{k-1}), \quad (2.7)$$

where  $c_k^x(\tau_1, \dots, \tau_{k-1})$ ,  $c_k^r(\tau_1, \dots, \tau_{k-1})$  and  $c_k^n(\tau_1, \dots, \tau_{k-1})$  are the  $k$  th-order cumulant of the seismic data, the reflectivity sequence and the noise respectively, and  $m_k^w(\tau_1, \dots, \tau_{k-1})$  is the  $k$  th-order moment of the wavelet. For  $r(t)$  is independent, identically distributed (IID) and non-Gaussian, the cumulant of  $r(t)$  becomes

$$c_k^r(\tau_1, \dots, \tau_{k-1}) = \begin{cases} \gamma_k^r, & \text{for } \tau_1 = \dots = \tau_{k-1} = 0, \\ 0, & \text{otherwise,} \end{cases} \quad (2.8)$$

where  $\gamma_k^r = c_k^r(0, \dots, 0)$  is the origin value of the reflectivity cumulant. Meanwhile, if the additive noise  $n(t)$  is assumed to be Gaussian (but need not be white), which means its third and higher order cumulants vanish, Equation (2.7) will be simplified to

$$c_k^x(\tau_1, \dots, \tau_{k-1}) = \gamma_k^r m_k^w(\tau_1, \dots, \tau_{k-1}), k > 2. \quad (2.9)$$

This equation states that the  $k$  th-order cumulants of the seismic data differ from the  $k$  th-order moments of the seismic wavelet only by a scalar. Therefore it has been the starting point for most of the mixed-phase wavelet estimation methods based on high-order statistics (Lazear, 1993; Velis and Ulrych, 1996; and references therein).



### 2.3 The validity of the prerequisites in using HOS

Here I will first introduce the synthetic models employed in the following test. Figure 2.1a is a zero-mean mixed-phase wavelet whose amplitude spectrum and phase spectrum are displayed in Figure 2.1b and 2.1c respectively. This wavelet has a dominant frequency of 25Hz and the passband at -3dB is about 30Hz. The amplitude spectrum is plotted as dB and the same hereinafter. The linear component of the phase spectrum has been removed for display purposes, which is corresponding to a time-shifted wavelet.

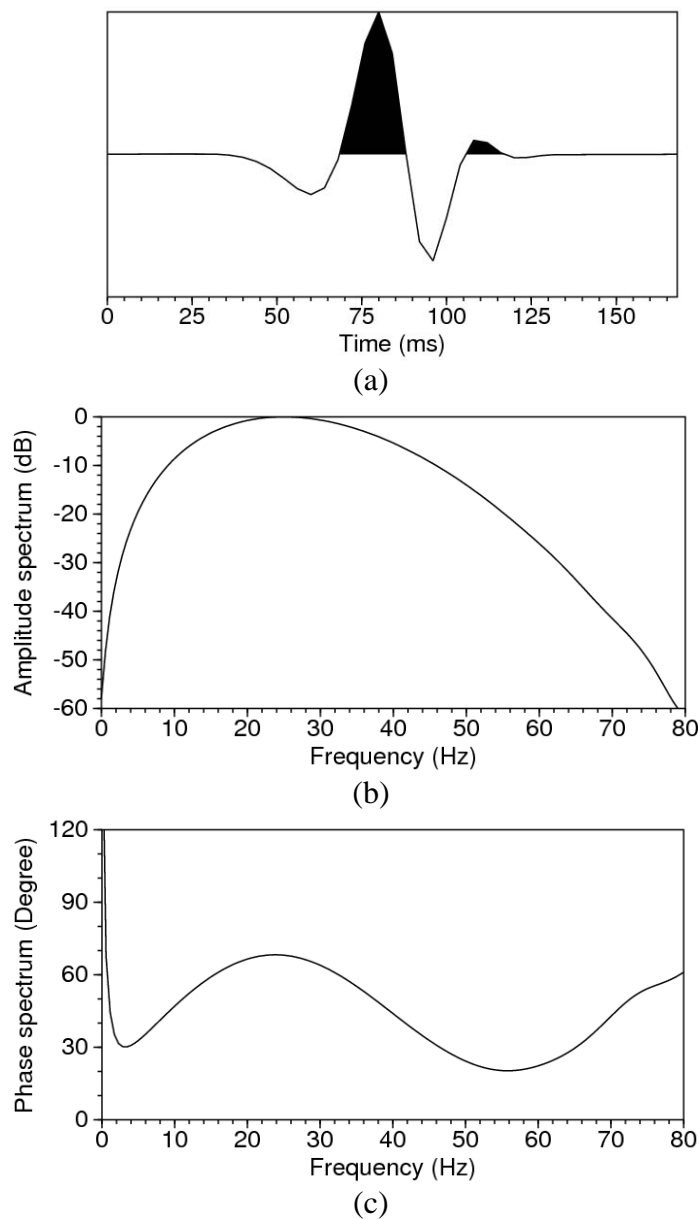


**Figure 2.1** (a) A synthetic zero-mean mixed-phase wavelet and its amplitude spectrum is plotted in (b) and the time-shifted phase spectrum in (c).

### **Reflectivity characteristic**

The amplitude distributions of seismic reflectivity sequences are usually leptokurtic (or less formally, spiky) (White, 1988), that is, they are more heavy-tailed than a Gaussian distribution. This property forms the basis of HOS method as the cumulants of a Gaussian series tend to be zero. Lazear (1993) proved that, the farther a reflectivity-sequence amplitude distribution is away from Gaussian, the closer to zero its non-zero lag cumulants are.

Walden and Hosken (1985) discussed the actual statistical properties of seismic reflectivity sequences through real well-log analysis, from which we know that seismic reflectivities are not white (normally spectrally blue) and hence not independent. Their spectra fall off towards zero at lower frequency instead of remaining approximately flat (white) as that of a random sequence would. Although the whiteness assumption for seismic reflectivities is very popular in current seismic processing (Yilmaz, 2001), White (1988) suggested a more hygienic solution than a faulty assumption of white reflectivities. If there is a well available, the colouring of seismic reflectivities can be estimated and one can apply a prefiltering to remove it. In this way the assumption of white innovations are satisfied and the colouring can also be recovered afterwards if necessary. It is also recommended by Velis and Ulrych (1996) to whiten the data before carrying out wavelet estimation to increase the effective bandwidth, which can be done by applying a zero-phase deconvolution. Figure 2.2a displays a seismic reflectivity sequence converted from real well log data, which are originally recorded at a depth interval of 0.125m, corresponding to a two-way travel-time interval of 0.2ms by using a typical velocity 2500 *m/s* of this area. Its amplitude spectrum Figure 2.2b indicates that this sequence is not strictly white but blue at the low frequency end (e.g. 0-500Hz), which conforms to Walden and Hosken (1985). After convolving with a zero-phase whitening filter (Figure 2.2c), this sequence (Figure 2.2d) is whiter which can be seen from the amplitude spectrum in Figure 2.2e. This convolution is reversible and the colour can be recovered at any time.

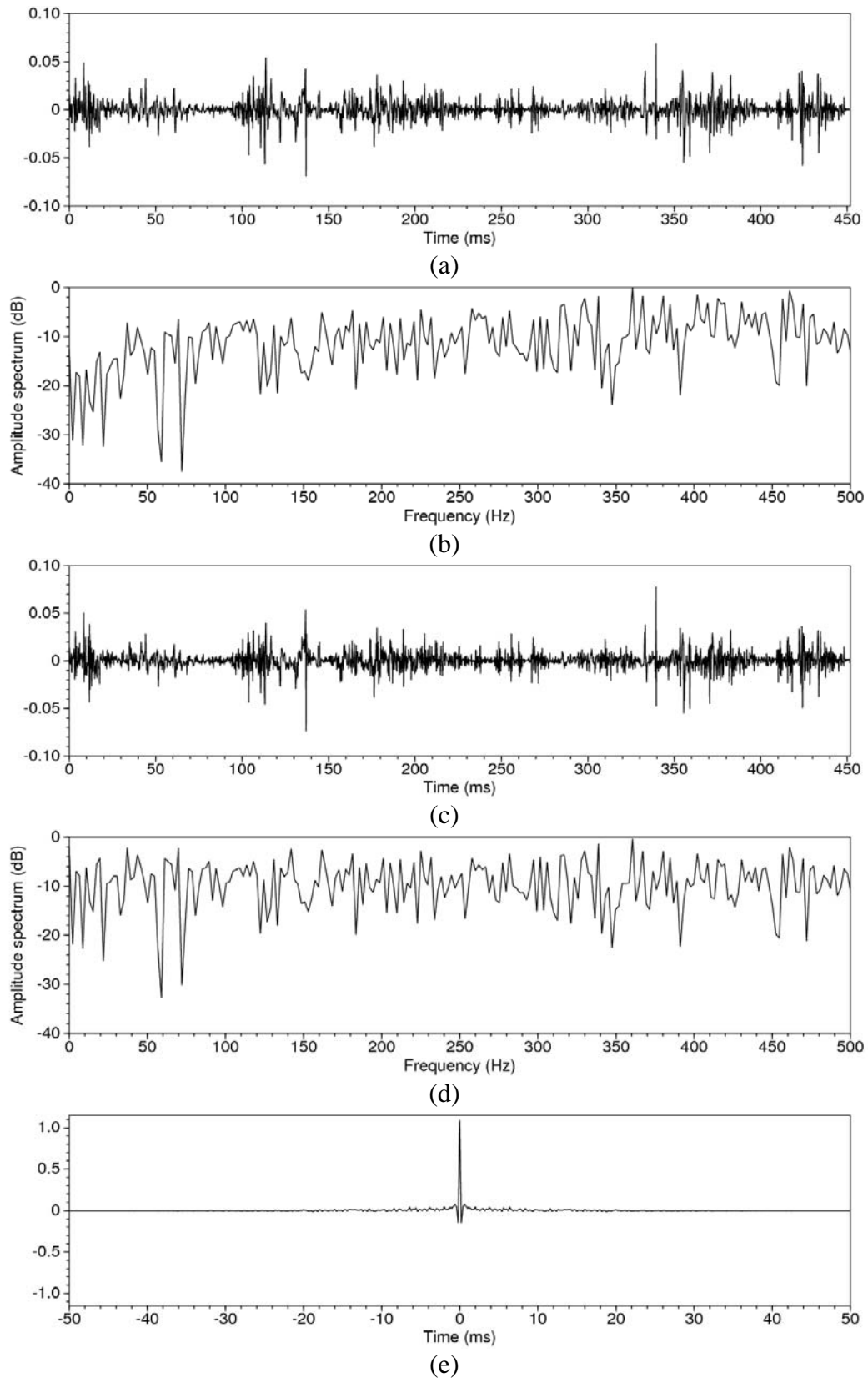


**Figure 2.2** (a) A seismic reflectivity sequence. (b) The amplitude spectrum of the sequence in (a). (c) The equivalent white sequence corresponding to (a). (d) The amplitude spectrum of the sequence in (c). (e) The whitening filter convolved with (a) to obtain (c).

Seismic reflectivities are less likely to be totally independent even when their spectra are white. Whiteness (lack of correlation) only confirms independence in the case of Gaussian sequences (White, 1988). However real applications based on HOS (Lazear, 1993; Velis and Ulrych, 1996) indicate that the restriction of independence can be alleviated if the problem is solved by a least-squares matching scheme.

### **Data bandwidth**

The sensitivity of kurtosis to wavelet phase has been studied by various authors (Levy and Oldenburg, 1987, White, 1988) when they estimated a residual phase shift present in the seismic data after standard deconvolution and stacking. Essentially, they recognised that if the effective bandwidth  $B$  of seismic data is smaller than the central frequency  $f_0$ , the kurtosis is then insensitive to phase changes. This also suggests that there is a threshold bandwidth below which wavelet phase can not be determined in the applications of HOS-based methods.

### **Data amount**

Equation (2.8) and in turn equation (2.9) are strictly valid in the limitation of an infinite amount of data and in reality the additive noise term in equation (2.7) is likewise not strictly zero even the noise is Gaussian. In practice neither the cumulant of the noise is zero nor is the cumulant of the reflectivity sequence a multidimensional spike at zero lag. For the wavelet shown in Figure 2.1a and the white reflectivity sequence displayed in Figure 2.2d, a synthetic trace is generated with 4ms sample interval, shown in Figure 2.3. Figures 2.4a and 2.4b compare the fourth-order moment (FOM) slice (at  $\tau_3 = 0$ ) of the wavelet and the fourth-order cumulant (FOC) slice (at  $\tau_3 = 0$ ) of the synthetic trace, and they differ very much not and only by a scalar.

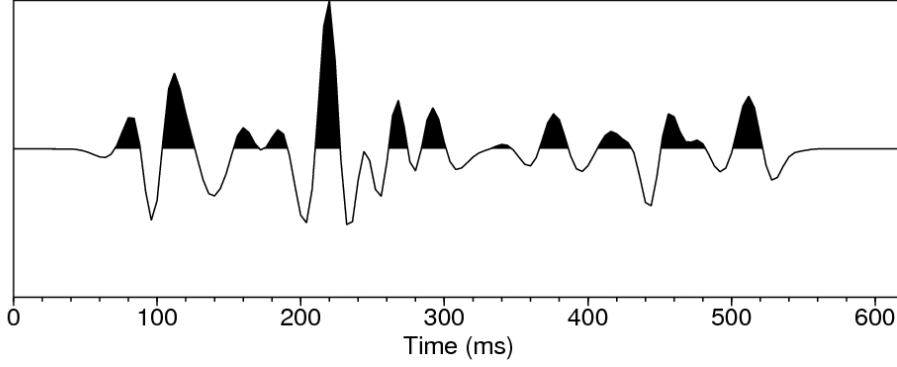


**Figure 2.3** A synthetic trace by convolving the mixed-phase wavelet (Figure 2.1a) and the white reflectivity sequence (Figure 2.2c).

To approximate the wavelet moment by using the seismic trace cumulant, one could apply a 3D smoothing-tapering window to the seismic trace cumulant (Velis and Ulrych 1996). Equation (2.9) may be rewritten as

$$\hat{m}_4^w(\tau_1, \tau_2, \tau_3) = \frac{1}{\gamma_4^r} a(\tau_1, \tau_2, \tau_3) \hat{c}_4^x(\tau_1, \tau_2, \tau_3), \quad (2.10)$$

where  $a(\tau_1, \tau_2, \tau_3)$  is a 3D window function that can be written as

$$a(\tau_1, \tau_2, \tau_3) = d(\tau_1)d(\tau_2)d(\tau_3)d(\tau_2 - \tau_1)d(\tau_3 - \tau_2)d(\tau_3 - \tau_1), \quad (2.11)$$

for which Velis and Ulrych (1996) recommended a Parzen window  $d(\tau)$  defined by

$$d(\tau) = \begin{cases} 1 - 6(|\tau|/L)^2 + 6(|\tau|/L)^3, & |\tau| \leq L/2, \\ 2(1 - |\tau|/L)^3, & L/2 \leq |\tau| \leq L, \\ 0, & |\tau| > L. \end{cases} \quad (2.12)$$

where  $L$  defines the region involved in computation. Figure 2.4c shows a slice of the 3D Parzen window. Figure 2.4d shows the FOC slice ( $\tau_3 = 0$ ) of the synthetic trace after applying the 3D Parzen window, which is now very similar to Figure 2.4a, the FOM slice ( $\tau_3 = 0$ ) of the zero-mean wavelet. For comparison purposes, Figure 2.4e displays the FOC slice (at  $\tau_3 = 0$ ) of a long seismic trace (2500 samples) without tapering, which offers an direct impression that more data can lead to accurate estimation.

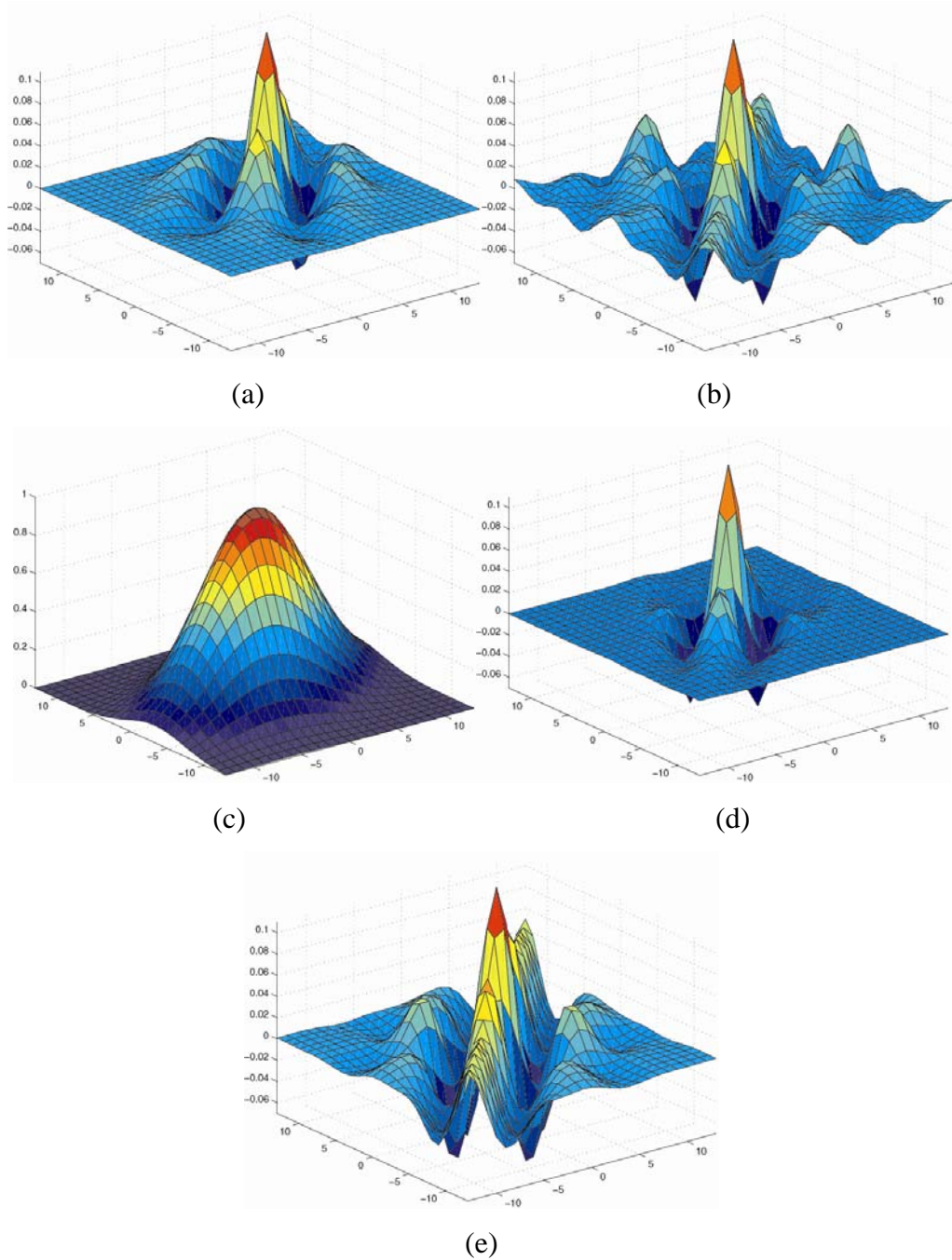


**Figure 2.4** (a) A fourth-order moment (FOM) slice of the wavelet in Figure 2.1a. (b) A fourth-order cumulant (FOC) slice of the synthetic trace shown in Figure 2.1b. (c) A slice of Parzen window. (d) Approximate FOM slice of wavelet by windowing FOC of the seismic trace. (e) FOC slice of a very long seismic trace.

The long seismic trace leading to the FOC slice in Figure 2.4e is generated by convolving a random reflectivity sequence with the mixed-phase wavelet displayed in Figure 2.1a. The synthetic reflectivity sequence, shown in Figure 2.5a with 50000 samples and 0.2ms intervals, is converted from a Gaussian random sequence by

raising each value to its power of 2 with its individual sign preserved. The probability density function (PDF) of this non-Gaussian sequence is displayed in Figure 2.5b. Whereas the synthetic seismic trace is shown in Figure 2.5c, which has been resampled to 4ms and will be employed in further experiments.

In the practice of residual phase correction, it also requires a considerable amount of data (Levy and Oldenburg, 1987; Longbottom et al., 1988; White, 1988). Particularly White (1988) pointed out that the amount of data needed to estimate the phase to reach certain accuracy is related to the extent to which the bandwidth exceeds the threshold. He advocated testing the time gate and number of traces needed to compute a reliable phase correction. Probably a practical criterion to judge whether the amount of data is enough, as suggested by Longbottom et al. (1988), is like this: check the results generated from different subsets of the original data to see whether the results are consistent. If an inadequate amount of data is employed to measure the phase, then the estimation results would vary wildly when the number of samples involved in the computation decreases.

### **Noise**

Wavelet estimation is usually carried out after processing has made the data fairly stationary, which is a reasonable assumption throughout daily geophysical practice. Given sufficient effort, modern techniques of acquisition and processing are generally capable of suppressing coherent noise in the seismic data largely and hence to neglect this kind of noise here is a reasonable practice. In obtaining equation (2.9), the noise term in (2.6) is assumed to be Gaussian and random. These assumptions are normal and popular in some seismic processing procedures.

Lazear (1993) discussed the sensitivity to Gaussian white noise in using HOS to estimate a wavelet. There is an increasing degradation of the wavelet when the noise-to-signal ratio becomes larger. This is due to the finite length of the Gaussian white noise in reality that prevents its cumulant from being zero. Hence the data cumulants are distorted by perturbations of noise cumulants from zero.

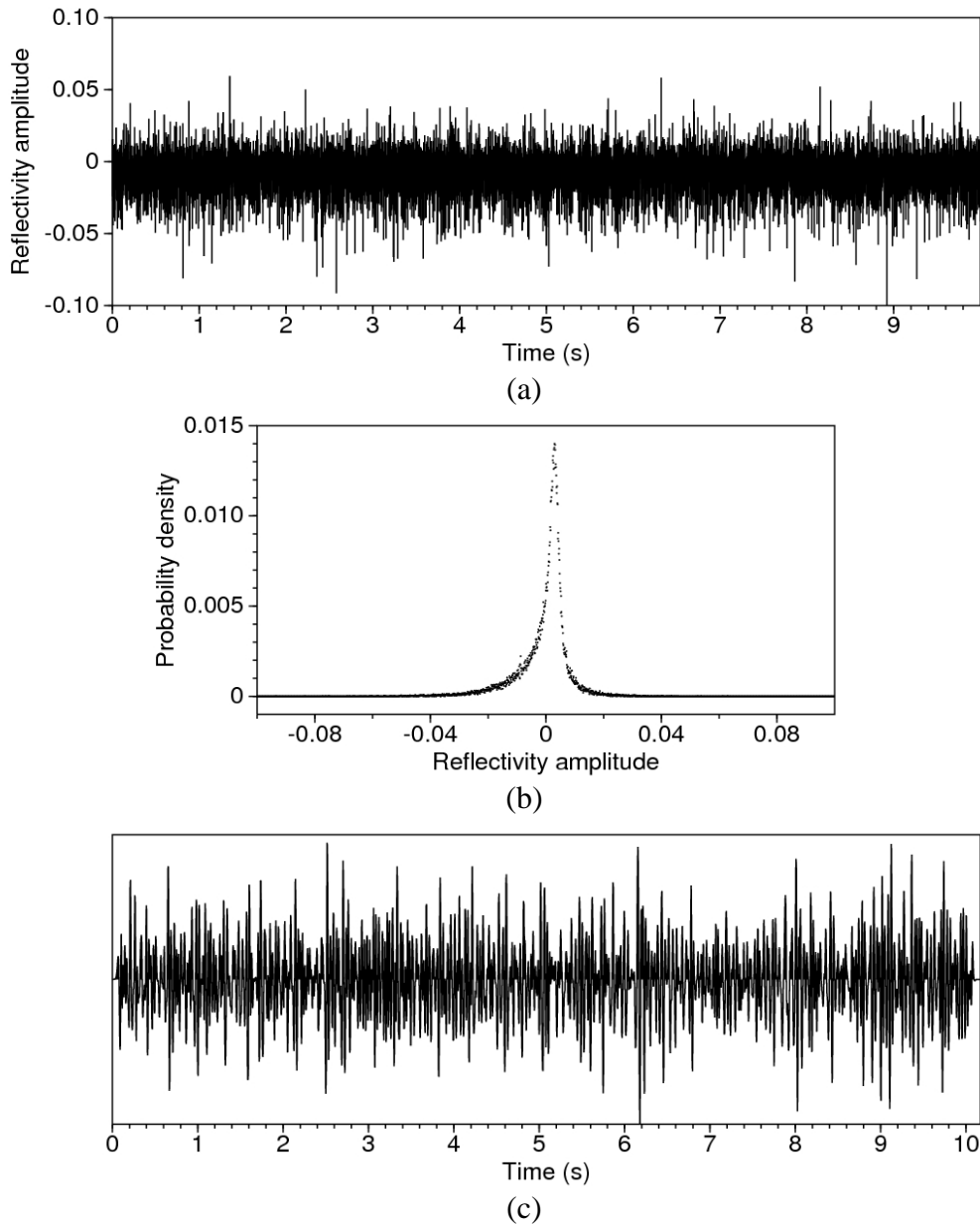


**Figure 2.5** (a) A random non-Gaussian sequence denoting reflectivity coefficients. (b) The probability density function of (a). (c) The long synthetic seismic trace.

## 2.4 Constant phase estimation

Recognising that seismic reflectivity sequences have leptokurtic amplitude distributions, White (1988) and Longbottom et al. (1988) introduced a constant phase correction method that renders the seismic data maximally non-Gaussian. The rationale behind their algorithm is that convolving any white reflectivity series with an arbitrary wavelet renders the outcome data less white but more Gaussian (van der Baan, 2008). Maximising the kurtosis means recovering the original reflectivity series



since kurtosis is a measurement of the deviation from Gaussianity. This basic thought comes from the minimum entropy deconvolution (Wiggins 1978) which tried to design a thorough deconvolution operator. However Wiggins' method suffers severe problems in practice, such as the operators are not stable and they often severely band-pass filter seismic data. Whereas White (1988) and Longbottom et al. (1988) searched for a constant-phase rotation (independent of frequency) that maximises the non-Gaussianity of seismic data, requiring only a single degree of freedom and thus stabilises the performance of their algorithm.

The phase correction is normally applied after standard deconvolution and stacking to account for the residual phase existing in the data. Although the authors stated that the relation between phase correction and the phase of the seismic wavelet can only be settled by case studies (White, 1988), the principle has been much written about in constant-phase wavelet estimation (e.g. van der Baan, 2008). The optimum phase is estimated by applying a series of constant-phase rotations to the data, as denoted by

$$c(t) = x(t)\cos\theta - H[x(t)]\sin\theta, \quad (2.13)$$

where the composite trace  $c(t)$  is made up of the original trace  $x(t)$  and its Hilbert transform  $H[x(t)]$  and  $\theta$  denotes the phase rotation angle. If the trace  $c(t)$  is normalised to unit power, the measured kurtosis of the composite trace is

$$\hat{k}(\theta) = \sum c^4(t)/N, \quad (2.14)$$

where  $N$  is the total number of samples of  $c(t)$  and again the superscript circumflex indicates the calculated kurtosis is a sample value. The most likely wavelet phase is corresponding to the angle that maximises kurtosis value. For the synthetic seismic trace shown in Figure 2.5c, its kurtosis variation with rotation angle is plotted in Figure 2.6a, with the maximum kurtosis occurs at 28 degrees. The corresponding constant-phase wavelet, which possesses the same amplitude spectrum as the synthetic wavelet, is plotted in Figure 2.6b. The correlation coefficient between the constant phase wavelet and the synthetic wavelet (Figure 2.1a) is 0.90.

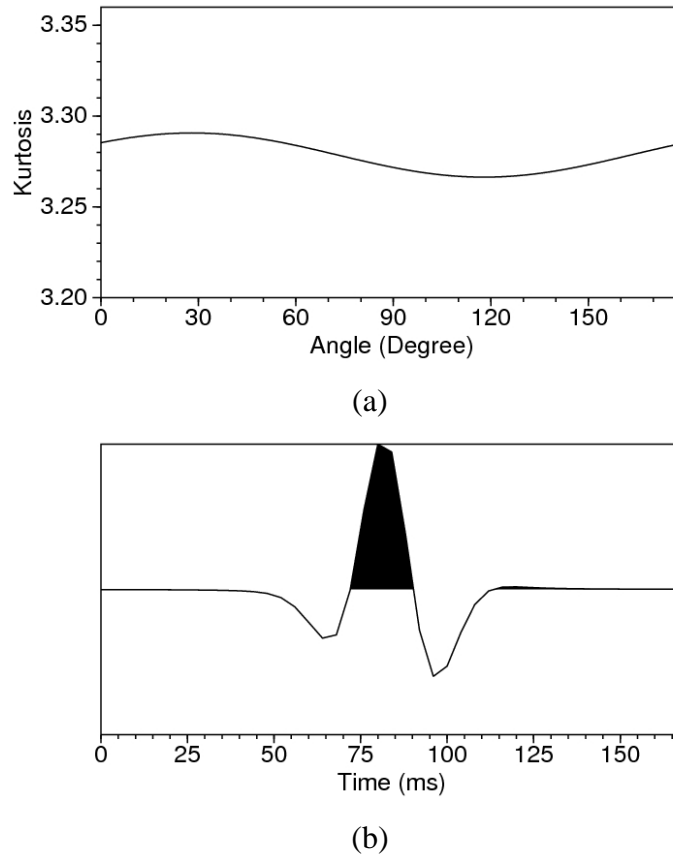


**Figure 2.6** (a) Kurtosis variation with rotation angle for the seismic trace in Figure 2.5c. (b) Constant-phase wavelet corresponding to the maximum kurtosis.

### 2.5 Mixed-phase wavelet estimation by iterative linear inversion

In this section, the constant-phase wavelet is updated using an iterative linear inversion method to solve a fourth-order moment matching problem depicted by equation (2.9). This technique has been prevalent in the signal processing area (Giannakis, 1987; Mendel, 1991) and was introduced into seismic exploration by Lazear (1993). Afterwards various authors have modified its application to be more practical and robust (Velis and Ulrych, 1996; Liang et al., 2002; Lu and Wang, 2007 etc).

The wavelet can be estimated by an inversion method that minimises the error in a least-squares sense between the calculated fourth-order moment of the wavelet to be estimated and the windowed fourth-order cumulant of the seismic trace,

$$J(w) = \sum_{\tau_1=-q}^q \sum_{\tau_2=-q}^q \sum_{\tau_3=-q}^q [\tilde{m}_4^w(\tau_1, \tau_2, \tau_3) - \hat{m}_4^w(\tau_1, \tau_2, \tau_3)]^2, \quad (2.15)$$

where  $q$  is the assumed effective length of the wavelet to be estimated, and  $\tilde{m}_4^w(\tau_1, \tau_2, \tau_3)$  is the windowed fourth-order cumulant of the seismic trace (equation 2.10). The objective function  $J(w)$  is a nonlinear multi-dimensional cost function since it involves high-order covariance computation.

Velis and Ulrych (1996) used a simulated annealing technique to solve the optimization problem in equation (2.15). However, the simulated annealing algorithm involves a trade-off between convergence to a global minimum and the speed of the algorithm. As a constant-phase wavelet, which is fairly close to the mixed-phase wavelet, is available from previous step, therefore, an iterative linear inversion method is adopted here to speed up the computation. Denoting the three time lags by a vector, this non-linear minimisation problem (2.15) is formulated in a matrix-vector form as

$$\mathbf{F}\Delta\mathbf{w} = \mathbf{e}, \quad (2.16)$$

where  $\mathbf{F}$  is a matrix of the Fréchet derivatives of the moment function at lag  $j$  with respect to the current wavelet sample  $w(i)$ :

$$F(j, i) = \partial \hat{m}_4^w(j) / \partial w(i), \quad (2.17)$$

which is calculated numerically here,  $\Delta\mathbf{w}$  is the wavelet updating vector, and  $\mathbf{e}$  is the residual vector formed by

$$e(j) = \tilde{m}_4^w(j) - \hat{m}_4^w(j). \quad (2.28)$$

Then the model updating vector is solved by

$$\Delta\mathbf{w} = (\mathbf{F}^T \mathbf{F} + \eta \mathbf{I})^{-1} \mathbf{F}^T \mathbf{e}, \quad (2.29)$$

where  $\eta$  is the so-called stabilising factor. It is set proportional to the maximum of the diagonal value of  $\mathbf{F}^T \mathbf{F}$ . Finally, the wavelet is updated by

$$\mathbf{w}^{(n+1)} = \mathbf{w}^{(n)} + \Delta \mathbf{w}, \quad (2.30)$$

where  $n$  is the iteration number. The whole process will stop when the residual energy is less than a threshold percentage of the whole initial wavelet energy, e.g. 0.0001 used here.

Using the constant phase wavelet in Figure 2.6b as an initial model to the iterative mixed-phase wavelet inversion, the resultant wavelet is shown in Figure 2.7, which is very similar to the true wavelet by having a correlation coefficient of 0.94.

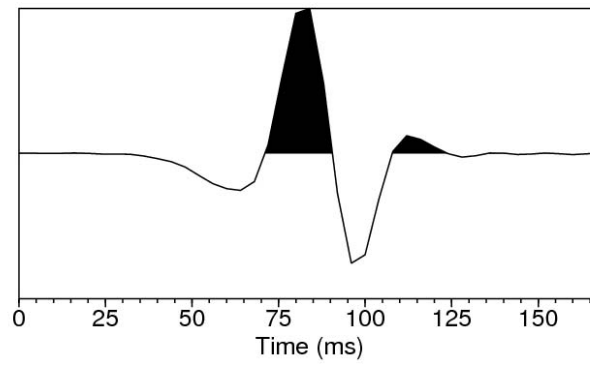


**Figure 2.7** Estimated mixed-phase wavelet using iterative inversion scheme.

## 2.6 Mixed-phase wavelet estimation in practice

In this section, I will apply the above mixed-phase estimation strategy to a real seismic example. Unlike the previous synthetic test where the true amplitude spectrum is available, we have to estimate the wavelet amplitude spectrum first, which is quite common and robust to achieve by using the autocorrelation (second-order statistics) of the seismic data. Here I just summarise this process as the following several steps:

- a. Define the analysis window.
- b. Taper both ends of the window.
- c. Calculate the autocorrelation of the data window.
- d. Calculate the amplitude spectrum of the autocorrelation.
- e. Approximate the amplitude spectrum of the wavelet by taking the square root of the autocorrelation spectrum.

The assumptions behind this application are white reflectivity sequences and Gaussian random noise. However the autocorrelation in step c is usually windowed in order to attenuate sampling errors.

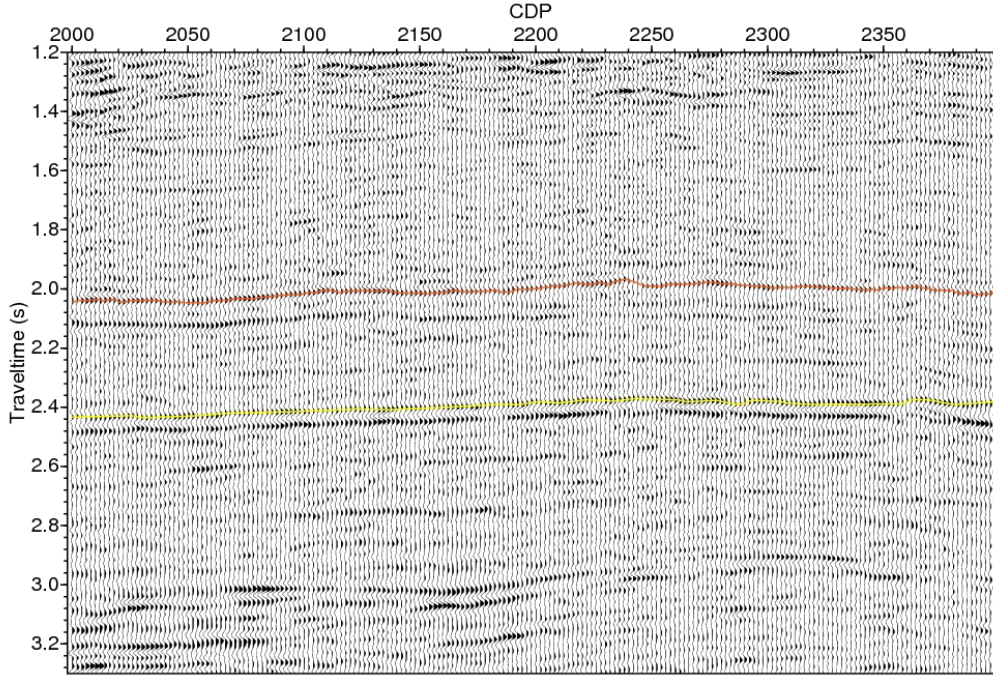


**Figure 2.8** The real seismic profile used for estimating wavelet.

Figure 2.8 shows a real seismic profile from the Glitne Field in the North Sea (Avseth et al., 2005) which is introduced in section 1.6. There is a well drilled at CDP 2232 that has been demonstrated in Figure 2.2. The top of the Balder formation (orange) and the top of the Chalk formation (yellow) are highlighted. For a reasonably accurate estimation, a large amount of data is required. Longbottom et al. (1988) pointed out that for simulations with a 40 Hz signal bandwidth and a Laplace IID sequence ( $k = 6$ ), at least 5000 data samples are needed to keep the standard error in phase estimation down to about  $10^\circ$ . However signals from nearby traces are far from independent and the effective number of samples is at least an order less than the real one (Longbottom et al., 1988). In our estimation here, the analysis window is taken from 1.25s to 3.25s with 101 traces around CDP2232 (50 each side plus the central trace), which contains a reasonable amount of samples according to the published literatures (e.g. White, 1988; Longbottom et al., 1988 and van der Baan, 2008).

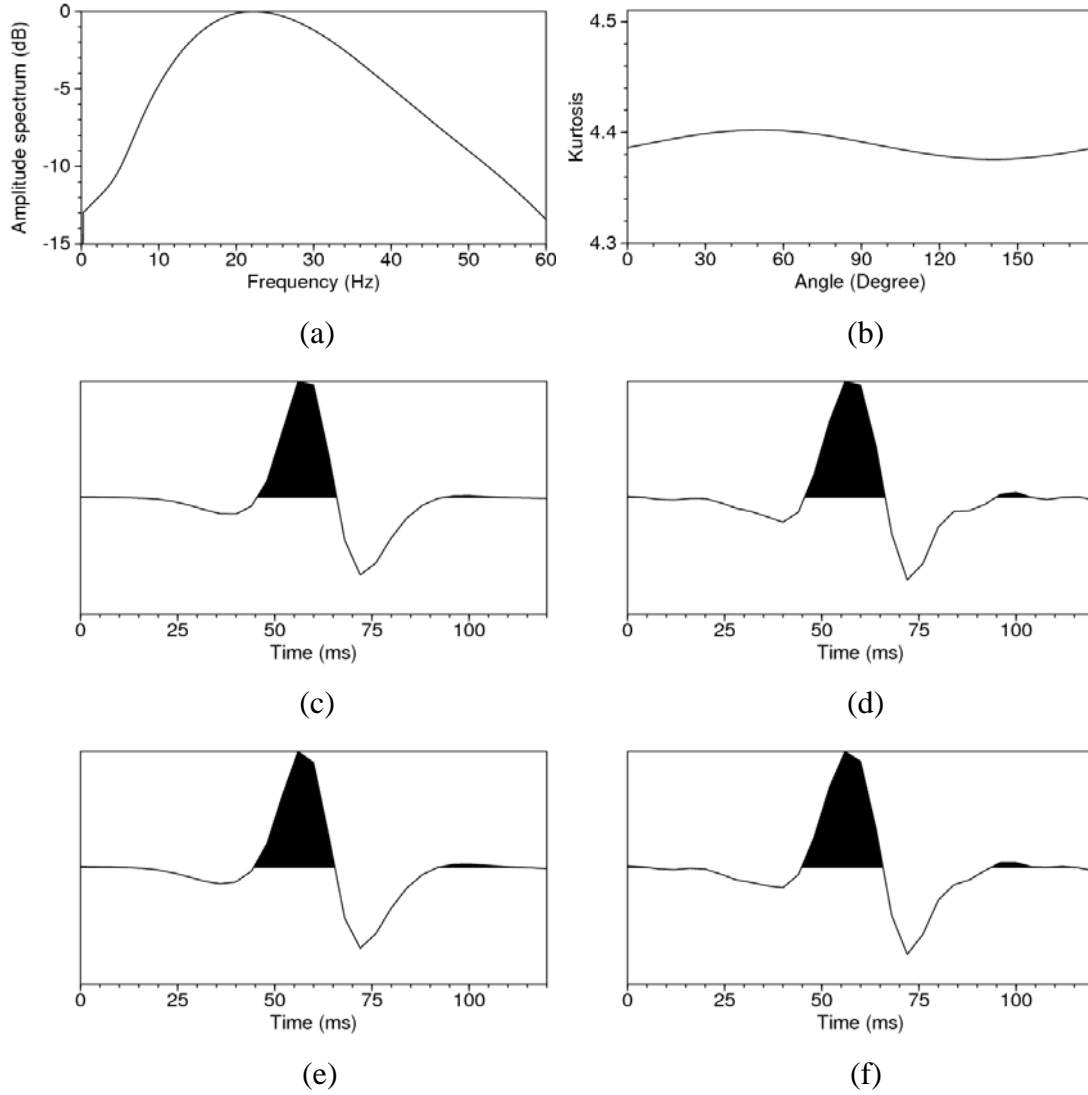
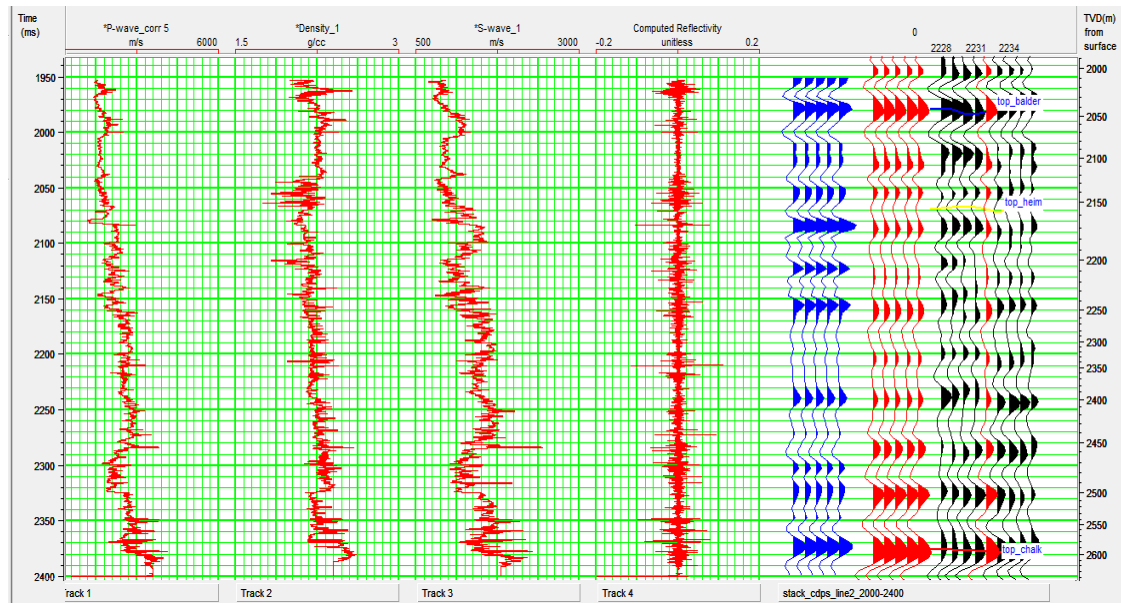


**Figure 2.9** (a) Estimated wavelet spectrum from the data. (b) The kurtosis variation with rotation angle. (c) The estimated constant-phase wavelet from the 3-second window. (d) The estimated mixed-phase wavelet from the 3-second window. (e) The estimated constant-phase wavelet from the 1.5-second window. (f) The estimated mixed-phase wavelet from the 1.5-second window.

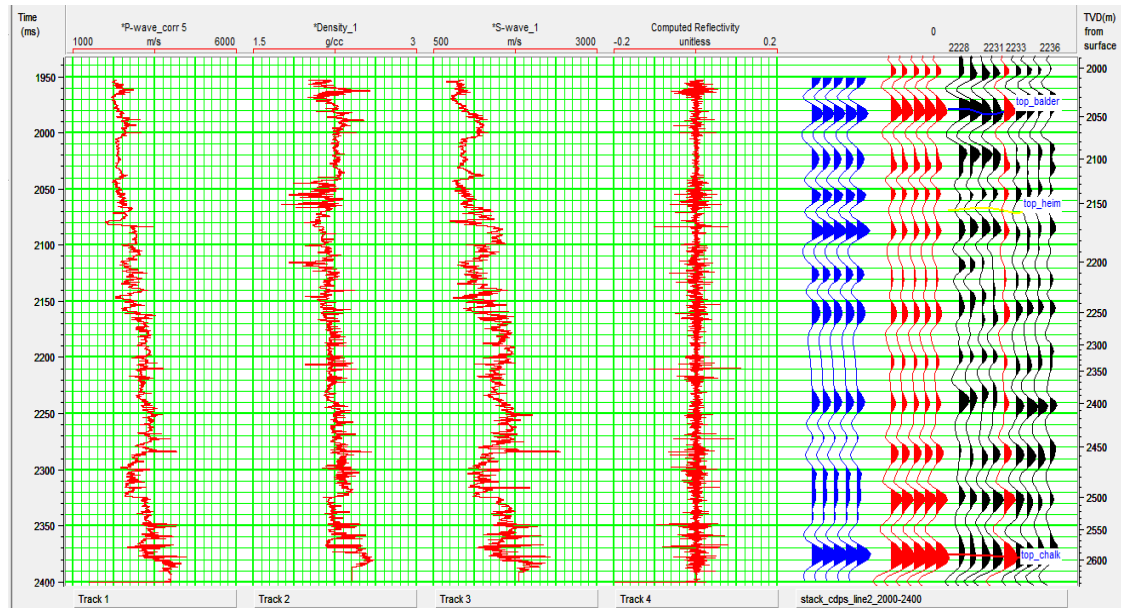
The estimated wavelet amplitude spectrum using the method described above is plotted in Figure 2.9a. Generally this spectrum is wide enough for statistical wavelet estimation, with a passband of -6dB from 8Hz to 42Hz and a dominant frequency of 21Hz. The kurtosis variation with rotation angle regarding these data is plotted in Figure 2.9b, suggesting a favourite constant-phase wavelet with a rotation angle of  $48^\circ$  degrees (Figure 2.9c). The mixed-phase wavelet using the constant-phase as an initial model through the iterative inversion is shown in Figure 2.9d. A useful QC

method as suggested by Longbottom et al. (1988), is to halve the window size to 1s (1.75s to 2.75s here) and then re-estimate the wavelets, which are shown in Figure 2.9e and 2.9f. In this case the constant phase is  $50^\circ$  and both the two wavelets are similar to those estimated from the 3-second window.

After the statistical mixed-phase wavelet estimation, it is desired to generate a synthetic trace from the well logs and tie the well to the seismic data. In doing this, to stretch or squeeze the synthetic trace in the well-tie practice should be largely avoided but only to shift it. For this North Sea data, our best well-tie performance without stretching is shown in Figure 2.10a, indicating a correlation coefficient of 0.5631 between the seismic trace and the synthetic trace using the statistically estimated wavelet. As the well now is tied to the seismic data, another category of reliable wavelet estimation method using the well-log data can be applied. Figure 2.10b displays the correlation between the seismic data and a new synthetic trace with an improved correlation coefficient of 0.6131. The new wavelet, shown in Figure 2.11, is generated from the Walden and White (1998) method by *Hampson-Russell* software, with an effective length of 100ms, a Papoulis lag window length of 200ms, a relative variance ratio of 1 and a white noise factor of 1%. It is very similar to the one estimated from HOS, indicating the statistical method can be used as an alternative when no well log is available.



(a)



(b)

**Figure 2.10** Correlation between the seismic data and the synthetic trace generated from the wavelets of (a) HOS method and (b) Walden and White (1998) method. The five blue traces are repeated reflectivity series convolved with the corresponding wavelet and the five red traces are the same as the single red one, which represents the real seismic trace in the well-tie position.



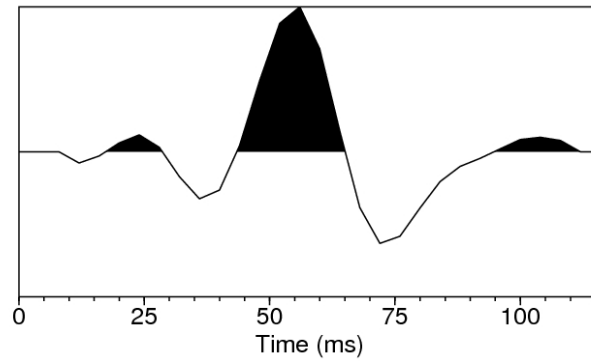


**Figure 2.11** Wavelet estimated using Walden and White (1998) method when the best well-tie is achieved.

## 2.7 Discussion

HOS can preserve the phase information of a system within  $180^\circ$  phase rotations so that before using HOS to estimate wavelets, the polarity needs to be determined first. For marine seismic data, it is easy to be identified at the water bottom and generally any known geological interface with strong and distinct reflection can help us to make the decision.

Both the synthetic test and the real application suggest that wavelet estimation based on HOS is a practical solution whenever well-log data are available or not, given the data bandwidth exceeds a certain threshold. The variance of the estimate is dependent on the kurtosis of the data, in addition to the inverse dependence on the bandwidth-duration product (White, 1988).

## **Chapter 3**

### **Seismic reflectivity inversion**

After the construction of constant-ray-parameter profiles, the inversion procedure from seismic data to ray impedance regarding different ray-parameter values is the same as that of elastic impedance inversion regarding different angles. Both ray impedance inversion and elastic impedance inversion can make use of the poststack impedance inversion scheme, which can be applied on ray-parameter stacks for ray impedance inversion or angle stacks for elastic impedance inversion. Well information can be integrated into inversion by using the explicit expression of ray impedance, as we did in elastic impedance.

In our impedance inversion scheme, the wavelet is assumed to be determined before the impedance inversion and will not change during the course of inversion. The whole procedure can be subdivided into two steps: the first is a reflectivity inversion from constant-ray-parameter profiles and the second is an impedance inversion from the inverted reflectivity profiles. These two inversions can be combined into a one-step inversion process from seismic data to impedance values directly, as most commercial software does. However we prefer this two-step inversion scheme since we can easily impose a sparseness constraint upon the reflectivity inversion and quantitatively control the reflectivity inversion results.

#### **3.1 Introduction**

The inversion of seismic reflectivity sequences is closely related to least-squares deconvolution (Robinson and Treitel, 1980) which tries to remove the effect of wavelets, with an ideal result to be the seismic reflectivity sequences. In practice, a pre-whitening technique is necessary to maintain the numerical stability, by adding a

small value on each diagonal element of the autocorrelation matrix. This is a standard procedure in classical seismic deconvolution processing (Robinson and Treitel, 1980), which regards both the reflectivity sequence and the noise distribution to be Gaussian from a statistical point of view. The results from this traditional deconvolution are densely spiky, i.e. not sparse, and can hardly serve as the reflectivity sequences for blocky impedance inversion. Indeed, the amplitude distributions of seismic reflectivity sequences are usually leptokurtic (Walden and Hosken, 1986), that is, they are more heavy-tailed than a Gaussian distribution. Based on this observation, different methods have been developed for reflectivity inversion, aiming to recover the non-Gaussianity of the reflectivity sequences as well as to provide a significant increase in effective bandwidth from the band-limited seismic observations. Oldenburg et al. (1983) proposed a linear programming scheme via the Fourier transform to solve seismic reflectivity. Debeye and van Riel (1990) adopted an  $L_p$  norm instead of the  $L_2$  least-squares norm in reflectivity inversion. Amundsen (1991) introduced a long-tailed probability density distribution Cauchy norm in carrying out reflectivity inversion, to supersede the Gaussian norm which will lead to the least-squares solution. This Cauchy constraint inversion principle is then applied to many inversion problems (Sacchi and Ulrych, 1995, 1996) to obtain sparse solutions. In this chapter, I review and improve the reweighting strategy advocated by Sacchi (1997) by casting a Cauchy constraint on the seismic reflectivity distribution, which turns the deconvolution processing into an iterative inversion. The seismic reflectivity inversion results will be sparser and more suited to be seismic reflectivity sequences for a blocky impedance inversion. Furthermore I also try to quantitatively estimate the Cauchy parameter, improving the strategy proposed by Jensås et al. (2008) who applied it in blocky AVO inversion.

From a statistical point of view, an inverse problem solution is not limited to a single set of predicted model parameters but can be represented by a probability density function (PDF) describing the model space. A Bayesian setting is a reasonable choice adopted by many geophysical inverse problems, which makes it possible to combine available prior knowledge with the information contained in the measured geophysical data (Tarantola and Valette, 1982; Tarantola, 1987; Scales and Tenorio, 2001; Ulrych et al., 2001). The Bayesian concept is widely recognised and accepted both in statistics and in geophysics, although the specific model definition and the

corresponding solution of an actual problem may be complicated. The solution to a Bayesian inversion problem is represented by the posterior distribution. However in this chapter I try to make use of the Bayesian setting to derive and optimise an inversion process, leaving the discussion of this method to the references mentioned above.

## 3.2 Regularisation using a Cauchy priori model

### 3.2.1 Seismic reflectivity inversion by time-domain deconvolution

A seismic trace  $\{d_k\}$  can be described using the convolution model as

$$d_k = \sum_j w_j R_{k-j} + n_k, \quad (3.1)$$

where  $\{w_j\}$  is the seismic wavelet,  $\{R_j\}$  is the seismic reflectivity series, and  $\{n_k\}$  is noise. The goal here is to recover the reflectivity series  $\{R_j\}$  from the recorded seismic trace  $\{d_k\}$ .

Suppose we can find a set of reflectivity series  $\{R_j\}$  such that the residuals are minimised in the least-squares sense. The objective function is defined as

$$J = \sum_k \left( d_k - \sum_j w_j R_{k-j} \right)^2. \quad (3.2)$$

The minimisation of  $J$  is accomplished by solving  $\partial J / \partial R_j = 0$ , which leads to the following matrix-vector system

$$\mathbf{C}_w^T \mathbf{C}_w \mathbf{r} = \mathbf{C}_w^T \mathbf{d}, \quad (3.3)$$

where  $\mathbf{C}_w$  is the convolution matrix containing the wavelet  $\{w_j\}$  properly padded with zeros in order to express discrete convolution. However, to ensure numerical stability, solution to equation (3.3) is stabilised by adding a small damping factor to the diagonal of the matrix  $\mathbf{C}_w^T \mathbf{C}_w$ . In signal processing, this damping step is called pre-whitening (e.g. Robinson and Treitel, 1980), and the solution is given by

$$\mathbf{r} = (\mathbf{C}_w^T \mathbf{C}_w + \eta \mathbf{I})^{-1} \mathbf{C}_w^T \mathbf{d}, \quad (3.4)$$

where  $\eta$  is the pre-whitening parameter.

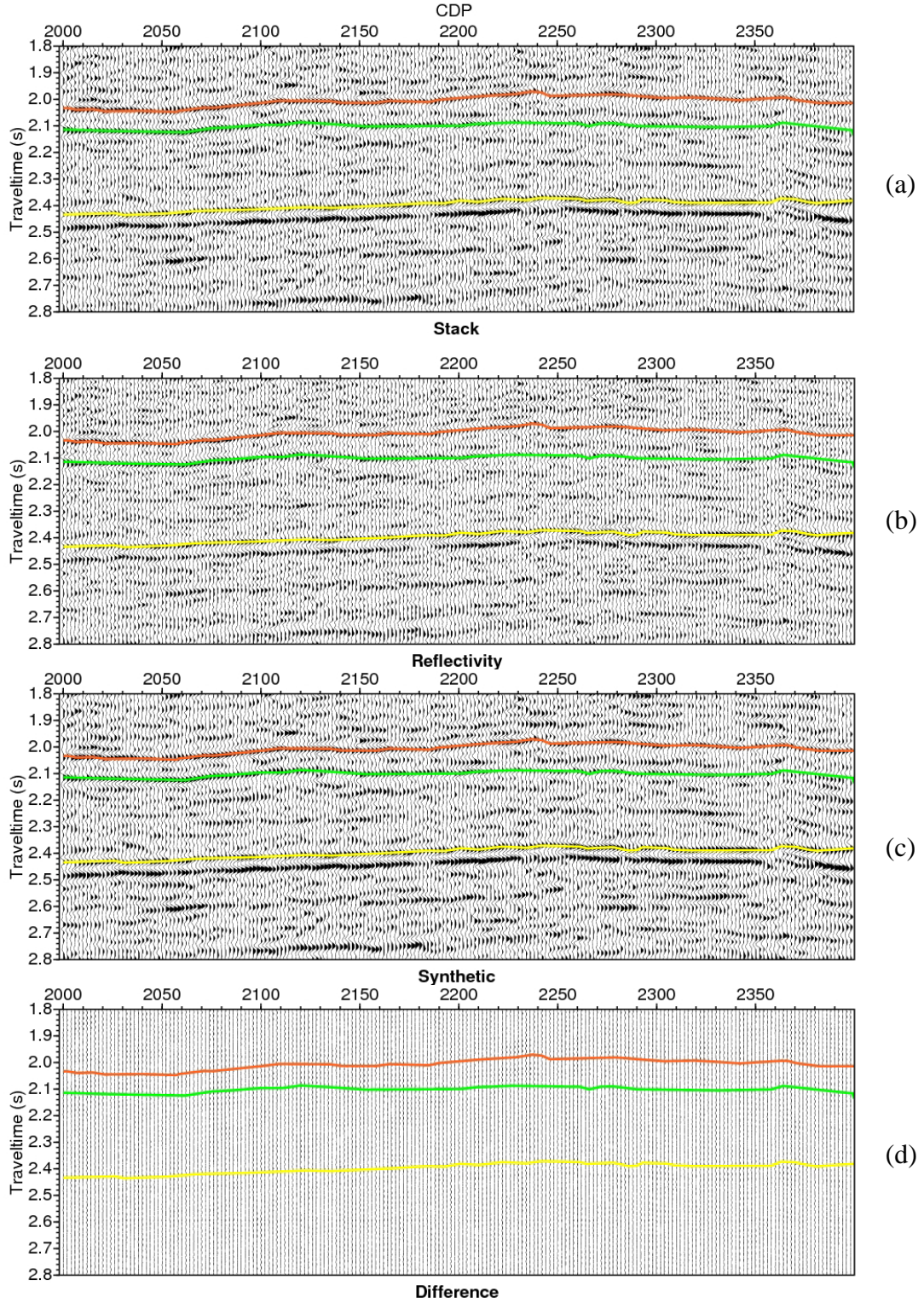


**Figure 3.1** Deconvolution illustrations. (a) An original seismic section. (b) Deconvolved seismic reflectivity. (c) Synthetic seismic section by convolving (b) with the wavelet. (d) Difference between the original and synthetic seismic sections caused by pre-whitening in the matrix inversion.

Figure 3.1a is the stack section from the same North Sea dataset introduced in section 1.6, and Figure 3.1b is the seismic reflectivity section obtained from equation (3.4) with  $\eta$  equal to 1% of the maximum diagonal value in  $\mathbf{C}_w^T \mathbf{C}_w$ . In Figure 3.1b, the deconvolution result does not show the seismic reflectivity is spiky as we wanted. Nevertheless if we convolve the result with the wavelet to generate a synthetic seismogram (Figure 3.1c), the synthetic profile is close to the original input. Figure 3.1d is the residual errors, caused by the pre-whitening technique. Although the pre-whitening causes slight accuracy loss, it is necessary in most linear inversion processes to maintain the numerical stability. To be more quantitative, the energy loss is 13.18%, 6.64% and 6.09% for  $\eta$  to be 1, 0.1 and 0.01 respectively of the maximum diagonal value, and for  $\eta = 0.001$  numerical instability starts to emerge. The result shown in Figure 3.1b is also the starting point for the following iterative inversion with Cauchy constraint.

The least-squares reflectivity inversion is actually assuming a Gaussian constraint applied on the model term. It can be derived by using a similar Bayesian procedure as described in the next section 3.2.2.

### 3.2.2 The Cauchy priori model

Deconvolution with pre-whitening is equivalent to applying a Gaussian prior distribution on reflectivity sequences. In the previous section, the example has demonstrated that the traditional deconvolution results are not sparse and spiky enough to generate blocky impedance profiles. Another constraint or algorithm is necessary in calculating this kind of reflectivity sequence. In this section, I intend firstly to obtain a sparse and spiky solution to the deconvolution problem by imposing a regularisation strategy based on a Cauchy criterion (Amundsen, 1991; Sacchi, 1997).

The probability density function (PDF) for a general Cauchy distribution can be written as

$$p(x) = \frac{1}{\pi} \frac{\lambda}{\lambda^2 + (x - x_0)^2} \quad (3.5)$$

where  $x_0$  is the parameter specifying the location of the peak of the distribution, and  $\lambda$  is the scale parameter which specifies the half-width at half-maximum of the

probability density. Figure 3.2 is a schematic comparison regarding the PDFs between the Cauchy distribution and the Gaussian distribution, both of which have the same central probability density. We find that the Cauchy distribution has a longer tail, which is closer to the real seismic reflectivity distribution (Walden and Hosken, 1986). A Cauchy distribution has an explicit expression for its cumulative distribution function (CDF)

$$P(x) = \frac{1}{\pi} \tan^{-1} \left( \frac{x - x_0}{\lambda} \right) + \frac{1}{2}. \quad (3.6)$$

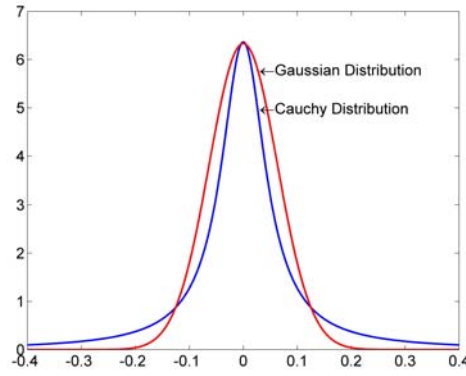


**Figure 3.2** Schematic comparison of PDF between a Gaussian distribution and a Cauchy distribution.

For a  $N$ -dimensional reflectivity sequence  $\mathbf{r} = \{R_0, R_1, \dots, R_{N-1}\}$ , whose components are independent of each other, the joint probability of  $\mathbf{r}$  is,

$$p(\mathbf{r}) = p(R_0)p(R_1) \cdots p(R_{N-1}) = \prod_{i=0}^{N-1} \frac{1}{\pi} \frac{\lambda}{\lambda^2 + R_i^2}. \quad (3.7)$$

In this expression,  $R_i$  is referred as  $x$  in equation (3.5) and (3.6) and its mean value is zero.

If we consider that the seismic data are contaminated with noise which has a zero mean and a Gaussian distribution, the conditional distribution of the data is given by

$$p(\mathbf{d} | \mathbf{r}) = (2\pi)^{-N/2} |\mathbf{C}_d|^{-1/2} \exp \left[ -\frac{1}{2} (\mathbf{d} - \mathbf{C}_w \mathbf{r})^T \mathbf{C}_d^{-1} (\mathbf{d} - \mathbf{C}_w \mathbf{r}) \right], \quad (3.8)$$

where  $p(\mathbf{d} | \mathbf{r})$  means the probability of  $\mathbf{d}$  given  $\mathbf{r}$ ,  $\mathbf{C}_d$  is the noise (data misfit) covariance matrix, and  $|\mathbf{C}_d|$  is the determinantal value of matrix  $\mathbf{C}_d$ .

For simplicity  $\mathbf{C}_d$  can be expressed as a diagonal matrix  $\sigma^2 \mathbf{I}$  where  $\sigma^2$  is the variance of the noise. However, it is difficult to estimate the noise variance reliably in practice and various authors have developed different approaches to this problem. There is a category of methods using the correlation coefficients of traces to derive  $\sigma^2$  in dealing with the weighted stacking problem (Robinson, 1970; White, 1977, 1984; Rietsch, 1980; Tyapkin and Ursin, 2005; Liu et al., 2009). In our approach, as the deconvolution process shown in Figure 3.1 achieves a fairly reasonable result, the noise variance is estimated from the residuals in Figure 3.1d.

According to Bayes's theorem which relates the posterior distribution  $p(\mathbf{r} | \mathbf{d})$  of a model  $\mathbf{r}$  (i.e. the solution of the inversion) to any knowledge about the model available before the inversion (the a priori model  $p(\mathbf{r})$ ) and our ability to describe the probability  $p(\mathbf{d} | \mathbf{r})$  of the data given the model, the a posteriori probability of the model under the current data is

$$p(\mathbf{r} | \mathbf{d}) = \frac{p(\mathbf{d} | \mathbf{r})p(\mathbf{r})}{p(\mathbf{d})}, \quad (3.9)$$

where the probability of the observed data  $p(\mathbf{d})$  is usually a constant and serves as a scalar factor only. The prior assigns the degree of plausibility that a model is correct. Once the prior probability is assigned, the problem remaining is how to compute a model. A natural rule is to compute the so called maximum a posteriori (MAP) estimator which maximises  $p(\mathbf{r} | \mathbf{d})$  by setting  $\partial p(\mathbf{r} | \mathbf{d}) / \partial \mathbf{r} = 0$ . Combining a Cauchy prior of the reflectivity distribution with the Gaussian distribution of the data misfits, the probability  $p(\mathbf{r} | \mathbf{d})$  for given data  $\mathbf{d}$  is expressed as

$$p(\mathbf{r} | \mathbf{d}) \propto \exp \left[ -\frac{1}{2} (\mathbf{d} - \mathbf{C}_w \mathbf{r})^T \mathbf{C}_d^{-1} (\mathbf{d} - \mathbf{C}_w \mathbf{r}) + \sum_{i=0}^{N-1} \ln \left( \frac{1}{\pi} \frac{\lambda}{\lambda^2 + R_i^2} \right) \right]. \quad (3.10)$$

The MAP estimator leads to minimising the objective function

$$J = \frac{1}{2} (\mathbf{d} - \mathbf{C}_w \mathbf{r})^T \mathbf{C}_d^{-1} (\mathbf{d} - \mathbf{C}_w \mathbf{r}) + N \ln(\pi \lambda) + \sum_{i=0}^{N-1} \ln \left( 1 + \frac{R_i^2}{\lambda^2} \right). \quad (3.11)$$



The objective function should be minimised iteratively because the Cauchy term is nonlinear in terms of the unknown variable vector  $\mathbf{r}$  and hence its derivative also consists of the unknown variables. Setting  $\partial J / \partial \mathbf{r} = 0$ , we obtain the solution

$$\mathbf{r} = \left( \mathbf{C}_w^T \mathbf{C}_d^{-1} \mathbf{C}_w + \frac{2}{\lambda^2} \mathbf{P} \right)^{-1} \mathbf{C}_w^T \mathbf{C}_d^{-1} \mathbf{d}, \quad (3.12)$$

where  $\mathbf{P}$  is a diagonal matrix defined as (Wang, 2003b)

$$\mathbf{P} = \text{diag} \left\{ \left( \frac{R_0^2}{\lambda^2} + 1 \right)^{-1}, \left( \frac{R_1^2}{\lambda^2} + 1 \right)^{-1}, \dots, \left( \frac{R_{N-1}^2}{\lambda^2} + 1 \right)^{-1} \right\}. \quad (3.13)$$

Solution (3.12) is given iteratively and the Cauchy distribution parameter  $\lambda$  controls the sparseness of the model vector  $\mathbf{r}$ . We need an initial estimate of the reflectivity series which can come from the least-squares inversion result.

### 3.3 Estimation of the Cauchy parameter and application

The quality of the Cauchy constraint inversion result is sensitive to the Cauchy parameter  $\lambda$ . Traditionally the value of  $\lambda$  is selected according to empirical experience which may lead to a wrong result. Here I introduce an automatic algorithm to estimate  $\lambda$  adaptively, following Jensås et al. (2008) in blocky AVO inversion.

As shown in the objective function (3.11), the term sensitive to  $\lambda$  is given as

$$Q = N \ln(\pi\lambda) + \sum_{i=0}^{N-1} \ln \left( 1 + \frac{R_i^2}{\lambda^2} \right), \quad (3.14)$$

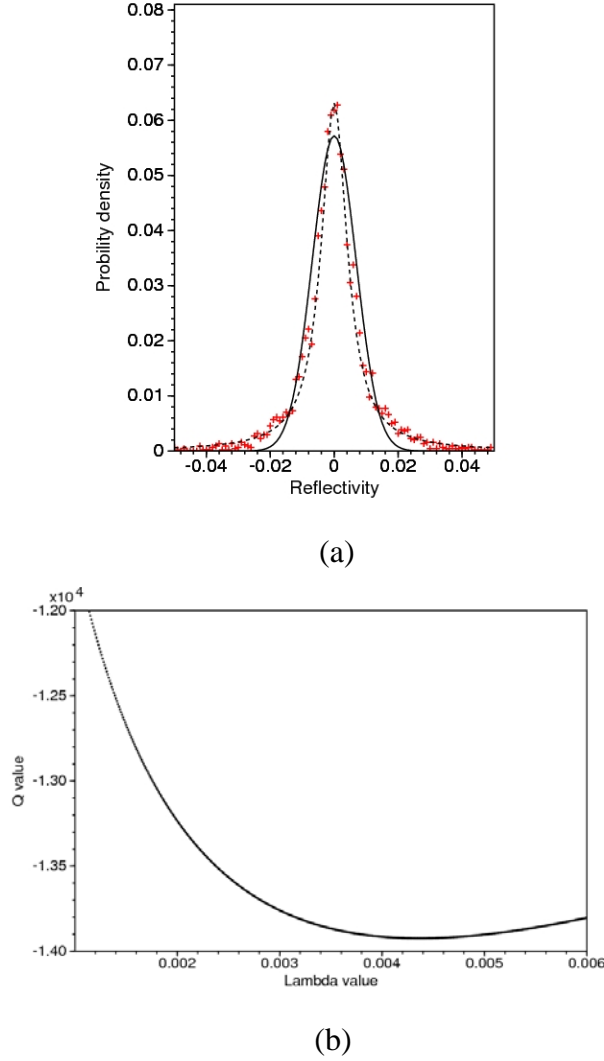
which is the negative log-likelihood (Freedman et al., 1978) of the Cauchy distribution. Setting  $\partial p(\mathbf{r} | \mathbf{d}) / \partial \lambda = 0$  leads to  $\partial Q / \partial \lambda = 0$  and the maximum likelihood estimation is then used to find the most reasonable parameter, which minimises the negative log likelihood function (3.14). Proceeding as usual, we find an optimum value for  $\lambda$  by solving

$$\frac{\partial Q}{\partial \lambda} \equiv \frac{N}{\lambda} - \frac{2}{\lambda^3} \sum_{i=0}^{N-1} R_i^2 \left( 1 + \frac{R_i^2}{\lambda^2} \right)^{-1} = 0. \quad (3.15)$$

That is, we find a particular  $\lambda$  that fulfils

$$\sum_{i=0}^{N-1} \frac{R_i^2}{\lambda^2 + R_i^2} = \frac{N}{2}. \quad (3.16)$$

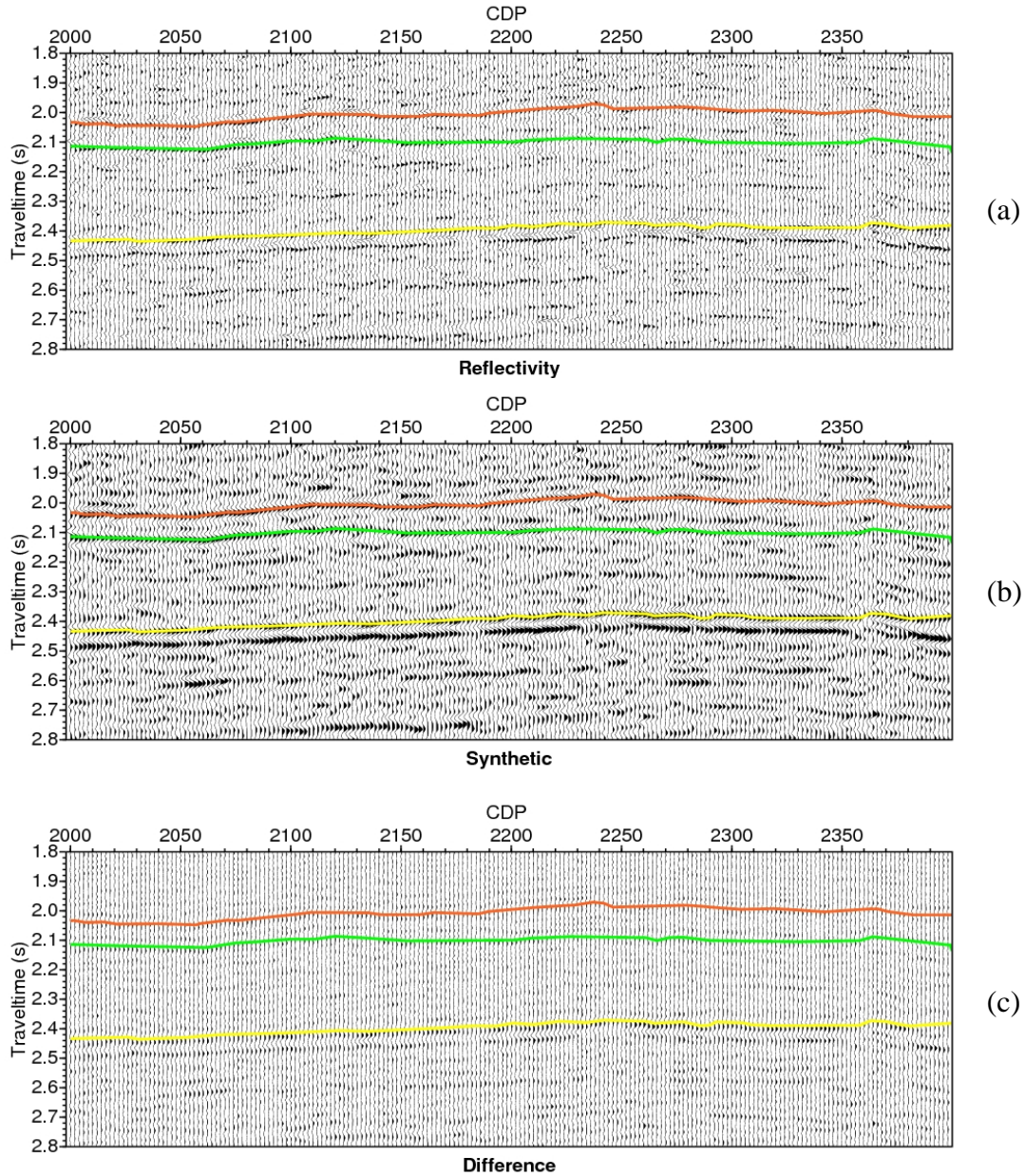
From (3.16)  $\lambda$  can be solved numerically by a Newton algorithm.



**Figure 3.3** (a) Histogram of the reflectivity amplitudes (red marks) with its best-fit Gaussian (solid line) and Cauchy (dashed line) curves. (b) The  $Q$  function plotted versus the Cauchy parameter  $\lambda$ . The estimated  $\hat{\lambda}$  value corresponding to the minimum  $Q$  value is 0.0042. Estimation is based on the well shown in Figure 1.2.

Solving (3.16) for  $\lambda$  needs information about the reflectivity coefficients. As there is a well (Figure 1.2) drilled in this area, it is very straightforward to employ the reflectivity series calculated from the well logs to estimate  $\lambda$ . Figure 3.3a displays the histogram of the reflectivity amplitudes (red marks) and the best-fit Gaussian (solid line) and Cauchy (dashed line) curves under a least-squares sense. It can be seen that the reflectivity sequence is better described with a Cauchy distribution, whose

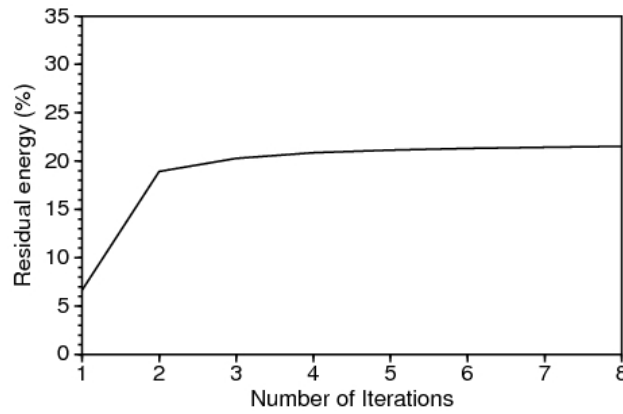
parameter is 0.0049. However Figure 3.3b certifies that for this example dataset, the estimated parameter  $\hat{\lambda}$  from (3.16) is 0.0042 by plotting the  $Q$  values in (3.14) against  $\lambda$ .



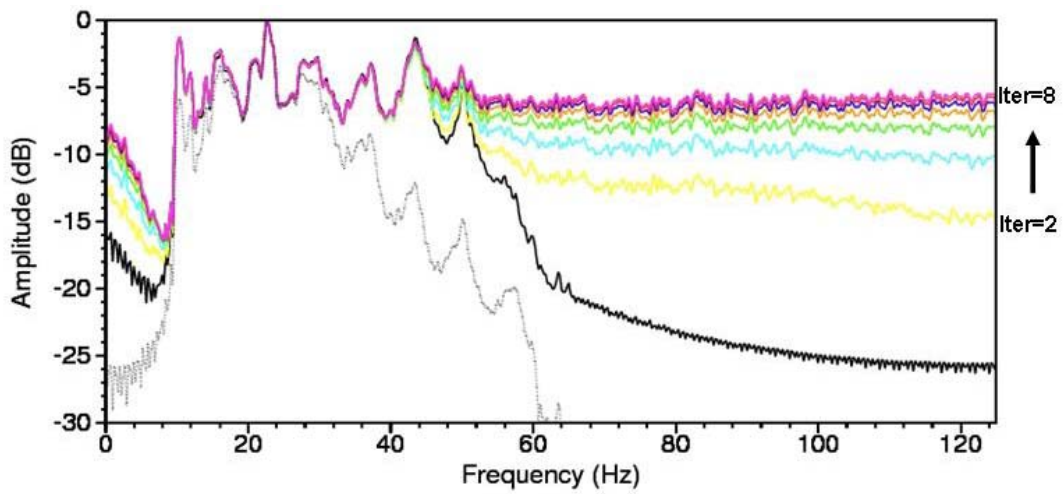
**Figure 3.4** (a) Sparse seismic reflectivity sequences under the Cauchy constraint using the optimum parameter. (b) Synthetic seismic section by convolving (a) with the wavelet. (c) Difference between the original and synthetic seismic sections caused by the Cauchy constraint inversion.

Figure 3.4a shows the Cauchy constraint reflectivity inversion result using the parameter  $\hat{\lambda}$  optimized from equation (3.16). Again the synthetic (Figure 3.4b) and the residual (Figure 3.4c) profiles are generated. For the Cauchy constraint inversion results with different iterations, we calculate the differences between the synthetic seismograms and the original seismic profile. The solid curve in Figure 3.5 indicates the residual energy variations with different iterations in contrast to the original input data energy (%). The first iteration produces a least-squares solution with the minimum energy residual, and the second iteration shows a big jump in the amount of residual energy. This is because the application of the Cauchy constraint suppresses small seismic reflectivity values, and hence the synthetic will have more residuals than the least-squares solution (iteration 1). However, further iterations that make the result spikier (shown later in Figure 3.6) and sparser (shown later in Figure 3.7) will not increase the residual very much, and the iterative inversion finally converges in terms of residual energy.

Figure 3.6 displays the amplitude spectra of the resultant seismic reflectivity sequences for different iterations, together with the grey one denoting the spectrum of the original stack section. The black curve is the spectrum of the deconvolution result without Cauchy constraint (Figure 3.1b) and all the others are Cauchy constraint solutions after different iterations (colour curves from bottom to top denoting iterations from 2 to 8), which gradually flatten the amplitude spectrum in the high-frequency components of the reflectivity sequences. This picture clearly shows the whitening progress of the reflectivity sequences during the iterative Cauchy constraint inversion in minimising equation (3.11), which makes the inverted reflectivity series spikier.



**Figure 3.5** Convergence rate of the iterative inversion with Cauchy constraint.

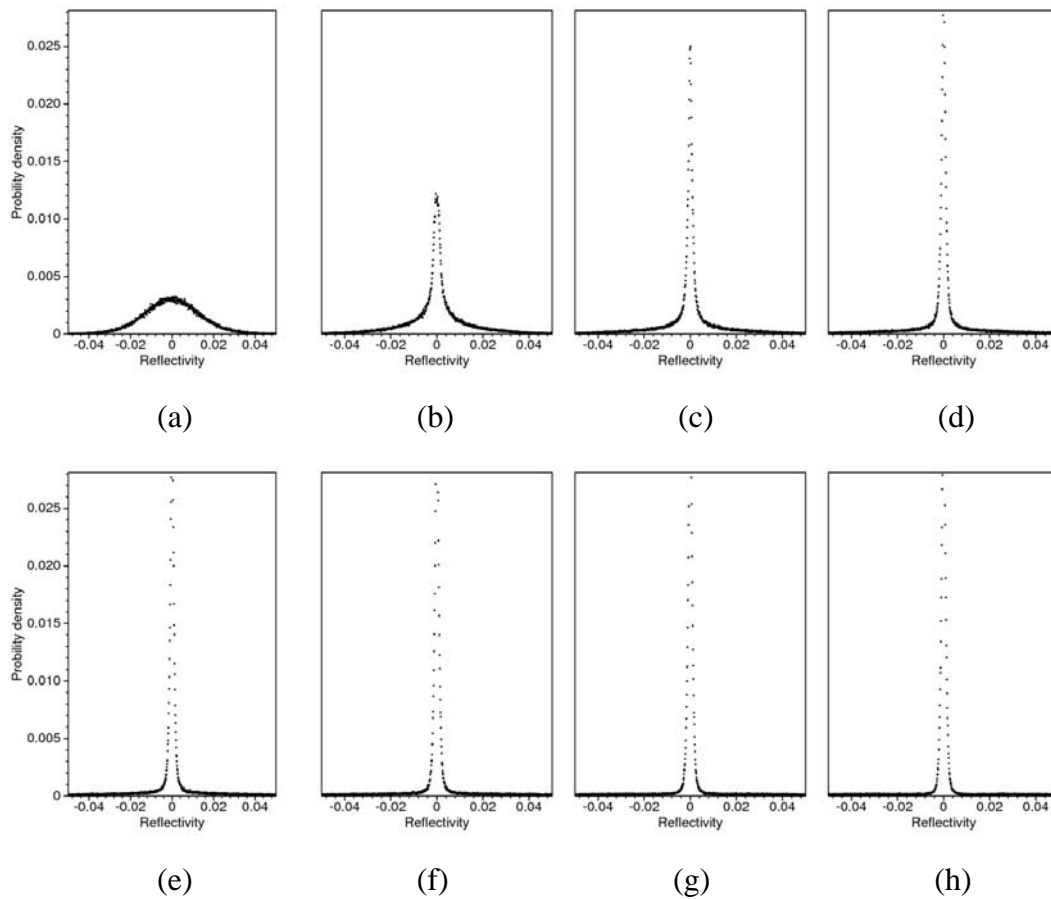


**Figure 3.6** The amplitude spectra of the original seismic profile (grey), the least-squares inversion result (black) and the seismic reflectivity sequences after different numbers of iterations in Cauchy constraint inversion (colour).

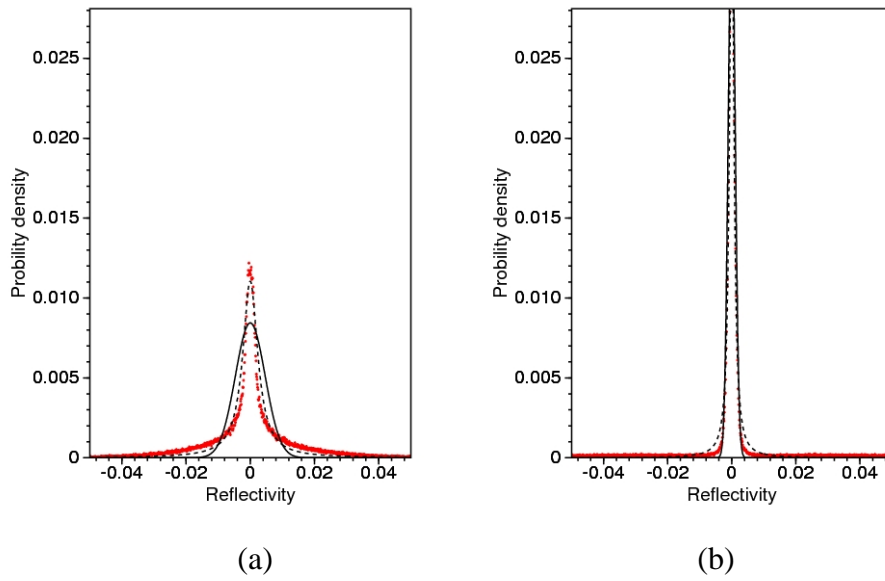
### 3.4 Statistical information of reflectivity series with different constraints

Figure 3.7 displays the histograms of the reflectivity sequences after each iteration. We can observe that the seismic reflectivity distribution from the conventional least-squares deconvolution is Gaussian and we expect all the others are more likely to be Cauchy. However, curve fitting to those distributions will reveal that the Cauchy constraint reflectivity inversion results gradually change toward a Gaussian distribution. Figure 3.8 compares the best Cauchy (dashed line) and Gaussian (solid line) fittings to the results of iteration 2 and iteration 8. Here “best fit” is achieved under a least-squares sense. The second iteration is the first time using the Cauchy

constraint in the inversion, and as expected the reflectivity distribution is close to Cauchy. This trend is best fitted in Figure 3.8a by a dashed curve (covered by original distribution red dots) with a Cauchy parameter  $\lambda = 0.002830$ . However, after 8 iterations, as shown in Figure 3.8b, the seismic reflectivity distribution can be fitted either by a Gaussian function (the solid line) with the standard deviation  $\sigma = 0.001092$  or Cauchy distribution with  $\lambda = 0.000824$ , which are close to each other and difficult to be judged as a better fit. Nevertheless both distributions can indicate that the reflectivity series after 8 iterations are sparser (with more zeroes) than the least-squares inversion result denoted by Figure 3.7a.



**Figure 3.7** The histograms of seismic reflectivity after a different number of iterations. (a)-(h) indicate the probability density function of seismic reflectivity after 1 to 8 iterations respectively.



**Figure 3.8** (a) A Cauchy fitting (dashed line, merged with the original distribution dots) of the reflectivity distribution after the first Cauchy constraint distribution compared with the best-fit Gaussian distribution (solid line). (b) After the 8th iteration, the reflectivity distribution changes towards Gaussian (solid line) rather than Cauchy (dashed line).

Finally, detailed comparisons have been made at the well location at CDP 2232 and plotted in Figure 3.9, where (a) is the acoustic impedance well log, (b) is the original stack section, (c) is the Gaussian constraint least-squares inversion result, (d) is the Cauchy constraint inversion result after 2 iterations, (e) is the Cauchy constraint inversion result after 8 iterations and (f) is the QC panel denoting the synthetic traces generated from (c) – (e) through convolution with the same wavelet, all of which are close to the original seismic trace (b). The three main horizons are labelled for clarity. The Gaussian constraint result (b) preserves all the reflections but each of them is not spiky at all to render a blocky impedance inversion result. The Cauchy constraint result after 2 iterations (c) has preserved major reflectors which are spikier. After 8 iterations, the Cauchy constraint inversion result (d) is spikier even more than (c), but a number of minor reflectors are eliminated, e.g., the Top Heimdal horizon at 2.07s. These minor reflectors may be crucial for identifying a reservoir and should be preserved. In this case we will use the inversion result after the 2nd iteration (the 1st Cauchy constraint inversion) for future impedance inversion.

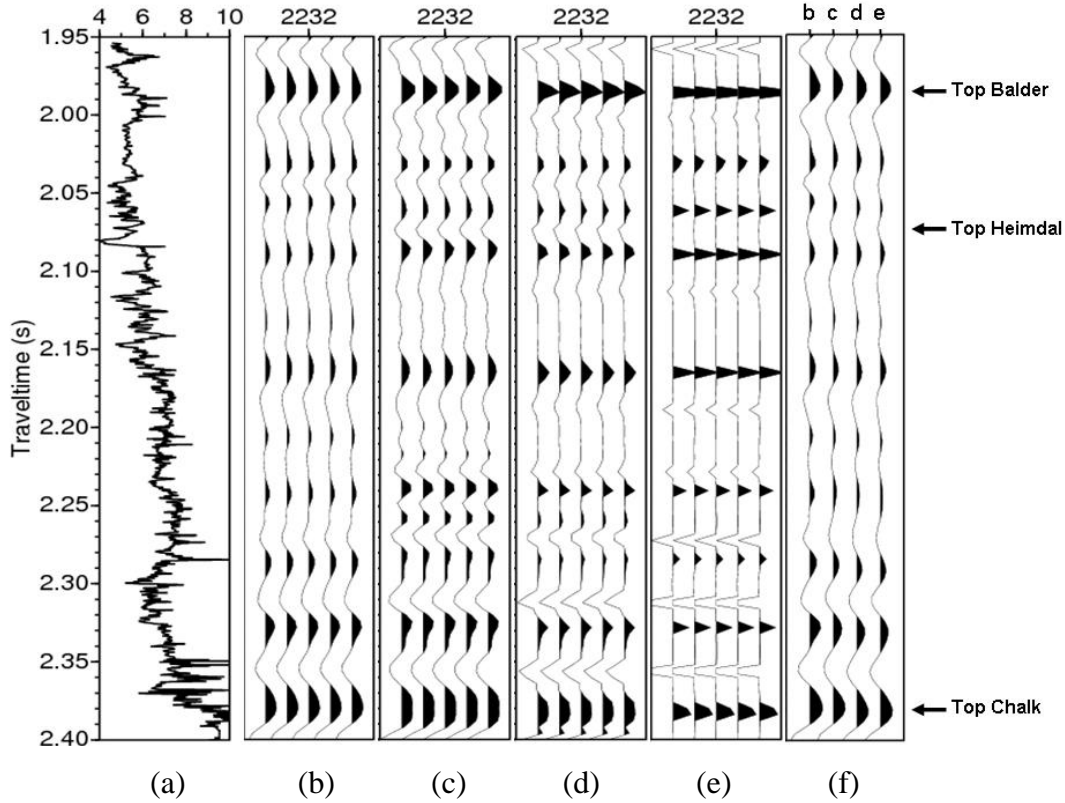


**Figure 3.9** (a) The computed acoustic impedance well log at CDP 2232. (b) The original stack section. (c) The Gaussian constraint least-squares inversion result. (d) The Cauchy constraint inversion result after 2 iterations. (e) The Cauchy constraint inversion result after 8 iterations. (f) The QC panel of synthetic traces generated from different reflectivity sequences.

### 3.5 Conclusions of sparseness constraint reflectivity inversion

The recovery of reflectivity from seismic is a non-unique inversion problem and many norms have been applied to obtain a stable result but at the cost of resolution loss. Conventional reflectivity inversion produces a least-squares solution with a Gaussian distribution. Cauchy constraint reflectivity inversion can make the reflectivity series spikier and sparser, and hence its results are more suitable for blocky impedance inversion. The essential Cauchy parameter plays a key role in controlling the spikiness and sparseness of the seismic reflectivity inversion result, which can be estimated quantitatively, based on available well logs. Generally the Cauchy constraint inversion after several iterations will achieve very spiky and sparse reflectivity sequences. As a consequence some minor geological structures are



eliminated, which is not desirable in doing seismic inversion or geological interpretation. Therefore we need to investigate in detail that which part of the seismic reflection profile is suppressed by the reflectivity inversion process and choose the most reasonable and beneficial parameters in this procedure.



## Chapter 4

### Ray impedance inversion and application

Ray impedance inversion, similar to elastic impedance inversion, can make use of the traditional acoustic impedance inversion algorithm after the seismic reflectivity traces are sorted according to different ray-parameter values. In this chapter, I adopt the generalised linear inversion (GLI) algorithm (Cooke and Schneider, 1983) to transform the reflectivity profiles obtained in Chapter 3 to impedance profiles. The GLI algorithm solves all the impedance values related to the reflection coefficients simultaneously by calculating the inverse of a matrix, which is more stable than the recursive inversion scheme (Cooke and Schneider, 1983). This GLI algorithm with a least-squares norm minimises the squared differences between the reflectivity sequences of the inferred model and those obtained through the reflectivity inversion method introduced in Chapter 3.

#### 4.1 Preparation for ray impedance inversion

In section 1.6.1 I have introduced the basic information of the seismic data which will be used in the following ray impedance inversion. This dataset has already been processed into the offset domain CIP gathers by the processing team of Norsk Hydro. For the prestack CIP gathers, there are 30 offsets ranging for 175m to 2350m with 75m intervals. Figure 4.1a displays the CIP gather at CDP 2232 where the only available well for this 2D line was drilled. As amplitude preserving time migration has already been applied on this data, a ray-tracing method (described in section 1.5.4) is used to transform the CIP gathers from the offset domain to the ray-parameter domain. The transformed gather corresponding to the one in Figure 4.1a is shown in Figure 4.1b, whose ray-parameter range starts from 0 to 0.3 s/km with 101 traces. The increase in the number of traces after the transform does not introduce extra

information related to waveform variations with offset into the ray impedance inversion but only makes sure that we do not lose it.

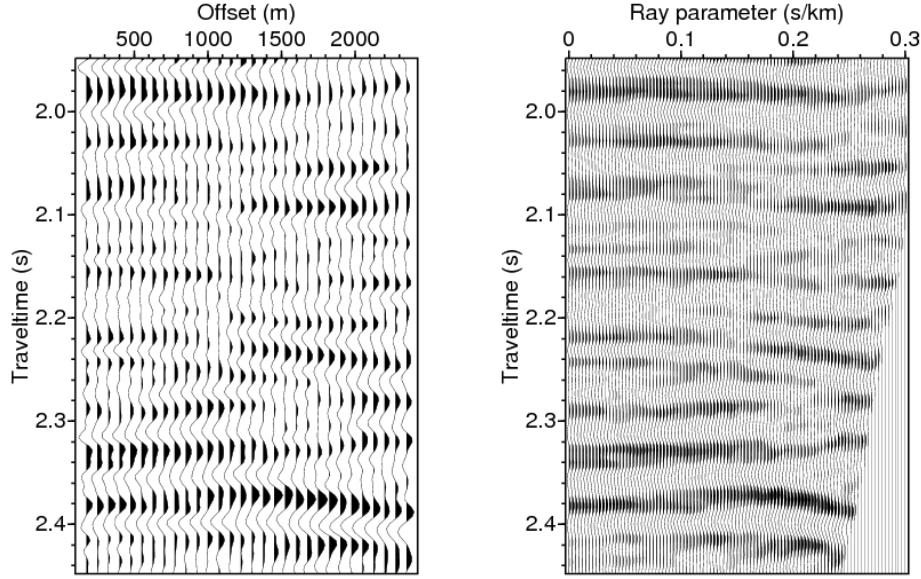


**Figure 4.1** CIP gathers at CDP 2232 in (a) the offset domain and (b) the ray-parameter domain

Velocity model building has been paid much attention for a long time as it is very important to many geophysical issues. There are many methods to achieve this from the basic velocity analysis to ray-based tomography (e.g. Jones, 2010). For our bending ray-tracing method, a smooth interval velocity field is needed to calculate the ray-parameter values (see section 1.5.4). This kind of velocity field is usually obtained by converting an RMS velocity using the Dix equation. As for this dataset here shown in Figure 4.1, no RMS velocity is available and we will build a velocity field from the P-wave velocity well log, which has already been tied to the seismic. Figure 4.2 shows the velocity field used to transform the CIP gathers from the offset domain (Figure 4.1a) to the ray-parameter domain (Figure 4.1b).

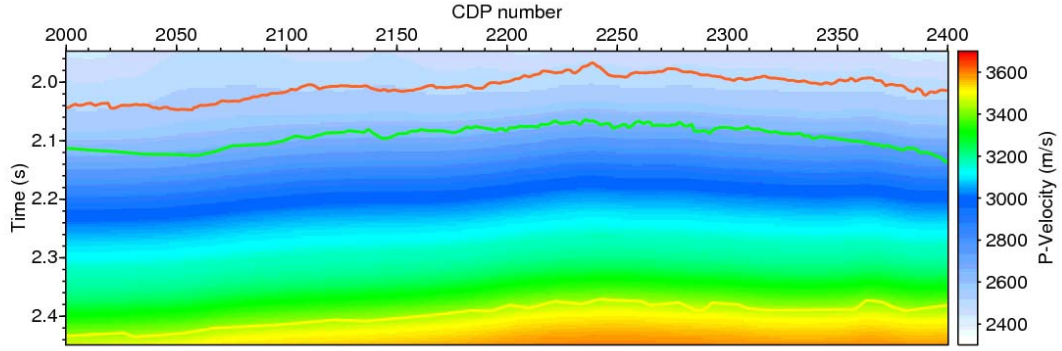
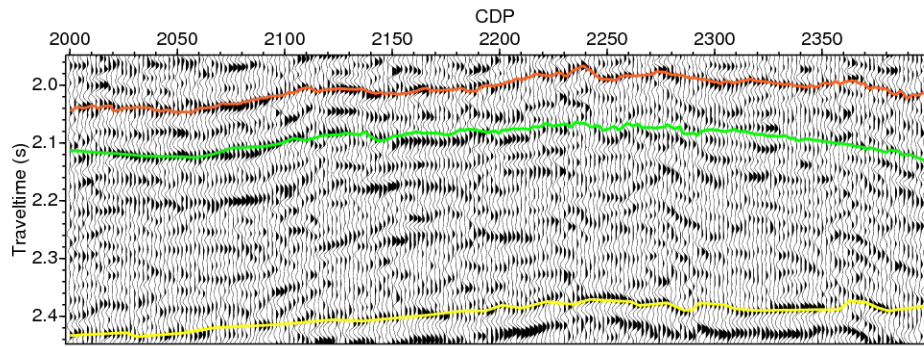
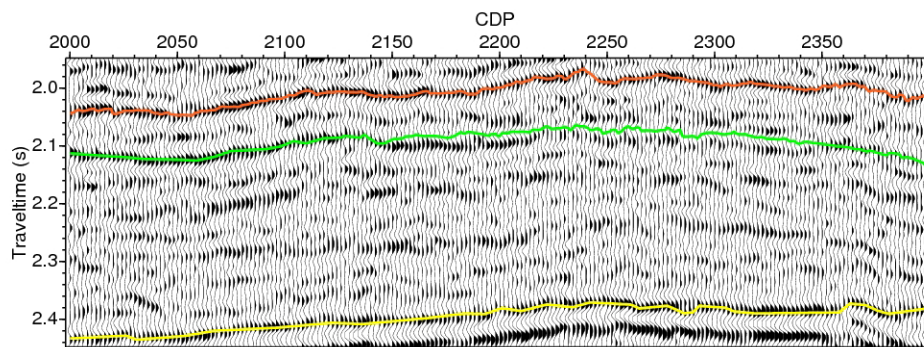


**Figure 4.2** Interval velocity field in the ray-tracing to transform the CIP gathers from the offset domain to the ray-parameter domain.

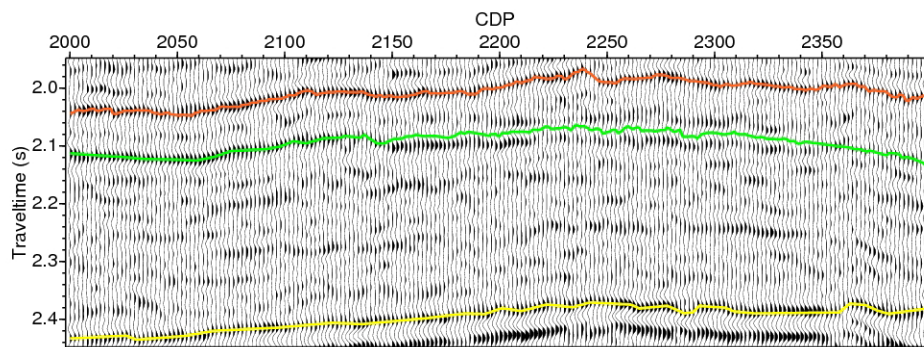
Based on the ray-parameter range after the above transform, several partial stacks at different ray-parameter values are generated, among which two are displayed in Figure 4.3a and 4.3b, representing the near stack ( $p = 0.05s/km$ ) and the far stack ( $p = 0.2s/km$ ). For comparison, the full stack is displayed in Figure 4.3c, which was utilised to invert acoustic impedance for many years. However, from Hendrickson (1999), it is no longer the case and the inverted impedance values should be calibrated to a different angle or ray-parameter value. The partial stack construction procedure is similar to the practice in elastic impedance inversion when building the angle stacks. In the future, I will refer the partial stacks defined on different ray-parameter values as constant-ray-parameter profiles. From those constant-ray-parameter profiles, seismic wavelets are estimated using the method described in Chapter 2 and then the Cauchy constraint reflectivity inversion depicted in Chapter 3 is carried out. The obtained reflectivity sections form the input to the ray-impedance inversion carried out in this chapter.



(a)



(b)



(c)

**Figure 4.3** The constant ray-parameter profiles at (a) 0.05 s/km and (b) 0.2 s/km. (c) The full stack.

## 4.2 Ray impedance inversion

After we defined the concept of ray impedance in Chapter 1, the reflection coefficients regarding the same ray parameter value can be written as

$$R_{pp}(p) = \frac{RI_{i+1}(p) - RI_i(p)}{RI_{i+1}(p) + RI_i(p)} \quad (4.1)$$

Equation (4.1) is expressed in a similar form in poststack acoustic impedance inversion without the independent variable  $p$ . Hence the ray-impedance inversion can make use of the existing poststack impedance inversion scheme if it is carried out on the ray-parameter domain stacks. Here the reflectivity profiles inverted from the constant-ray-parameter sections using the Cauchy constraint reflectivity inversion described in Chapter 3 are already available to use.

Written in matrix-vector form, (4.1) is expanded using a Taylor series as

$$\mathbf{R}_{pp}(\mathbf{RI}) \approx \mathbf{R}_{pp}(\mathbf{RI}_0) + \mathbf{G} \cdot (\mathbf{RI} - \mathbf{RI}_0) \quad (4.2)$$

where  $\mathbf{RI}$  is the impedance profile to be solved for,  $\mathbf{RI}_0$  is the initial model for the impedance profile and  $\mathbf{G}$  is the partial derivative matrix of the reflectivity coefficients with respect to ray impedance values. Here  $\mathbf{G}$  is calculated explicitly and the truncated Taylor expansion (4.2) can be solved for the updating vector  $\delta\mathbf{RI} = \mathbf{RI} - \mathbf{RI}_0$  and thus the impedance values will be obtained iteratively.

Examining equation (4.2), we will find that the number of unknowns (impedance values) is one more than the number of the sample points in a seismic reflectivity trace, supposing both sample intervals are identical. This character determines one source of the non-uniqueness of the solution to this inversion problem. In order to have a good solution, we need a reasonable impedance profile to be the initial model and it can serve as the hard constraint as well if necessary. Indeed the main function of the initial model is to compensate the low-frequency loss in seismic data. In my approach, a least-squares conjugate gradient scheme is adopted to solve this impedance inversion problem described by equation (4.2).

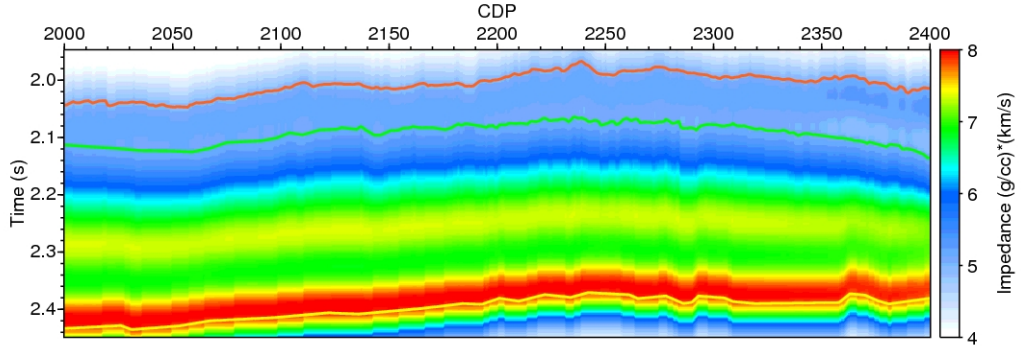
### **4.2.1 Initial model building**

The initial impedance models are built for constant-ray-parameter profiles at different ray-parameter values. They are constructed explicitly through the definition of ray impedance from the P- and S-wave velocity plus density models, which will also be used in the future simultaneous elastic inversion in Chapter 5. The three elastic models are constructed from available well logs after 1) a number of controlling geological horizons have been picked and 2) a good well-tie is achieved. First a low-pass filter is applied on each well log to keep the low-frequency components only, with a 4-6Hz high cut. This frequency range is chosen because those components under 5Hz are almost missing in the seismic data, which will be applied a 4-6Hz low cut as well. The three elastic parameter models are constructed initially at the well location, and then extrapolated to the other locations following the picked horizons. Outside the well location, the model values are obtained through linear interpolation within each controlling horizon pair, according to those low-pass-filtered values between the corresponding horizons at the well location. In this ray-impedance inversion on the North Sea dataset, there are three controlling horizons which are the tops of Balder, Heimdal and Chalk formations. Figure 4.4 displays the three initial impedance models, corresponding to those profiles shown in Figure 4.3.

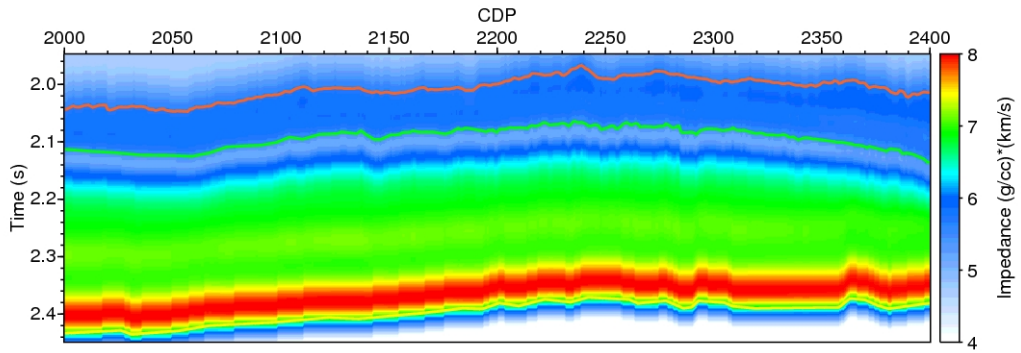
### **4.2.2 Reflectivity scalar**

In order to tune the relative amplitudes in the seismic data to their genuine scale, we need to derive a scalar for a whole constant-ray-parameter profile at a certain ray-parameter value. It can be calculated by dividing the RMS value of the average seismic trace around the well by the RMS value of the synthetic trace obtained from the well logs convolved with the estimated wavelet. This is usually carried out in a window around the target depth. Alternatively one can derive the scalar by a direct amplitude comparison at a known geological interface between the seismic trace and the synthetic trace. The latter method is normally adopted when an interface generates very strong reflections. However for the ray-impedance inversion in this thesis, I adopt the former strategy with averaging the five consecutive traces adjacent to the well, since this method is more stable.

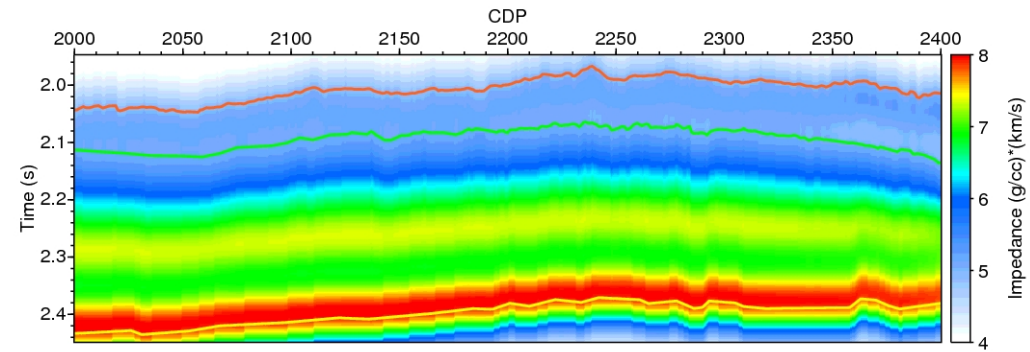




(a)



(b)



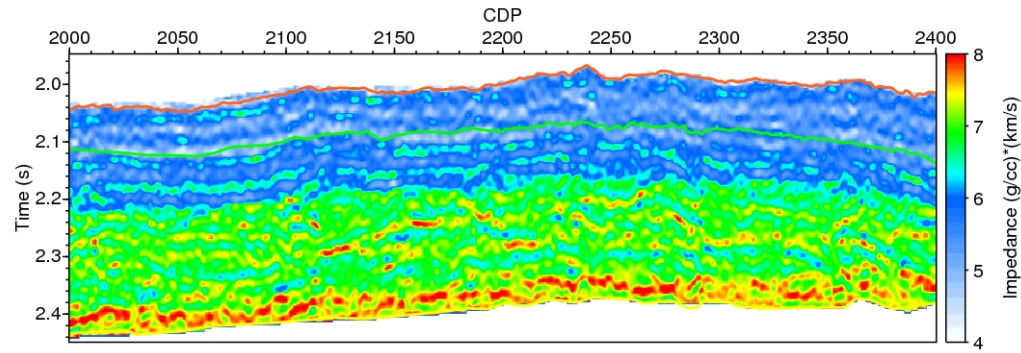
(c)

**Figure 4.4** Initial ray-impedance models with different ray-parameter values at (a) 0.05 s/km, (b) 0.2 s/km and (c) the acoustic impedance model.

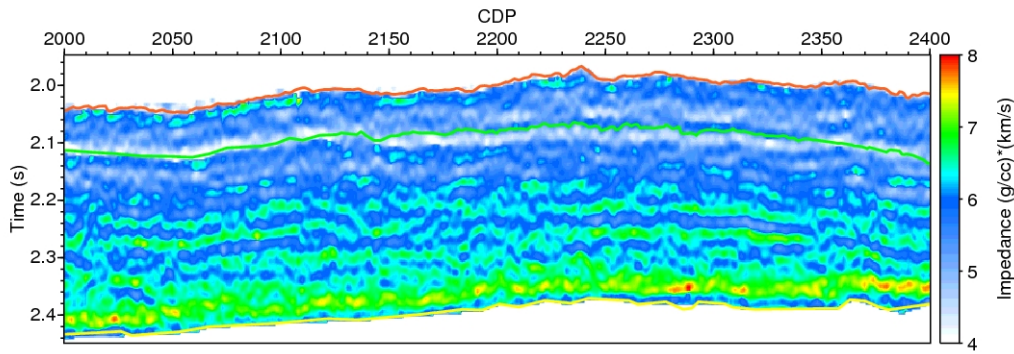
### 4.2.3 Ray impedance inversion result

Figure 4.5 displays the ray impedance inversion results at different ray-parameter values, where the values outside the inversion window are intentionally set to be zero for a better view. The approximately inverted acoustic impedance from the near stack can be regarded as the ray impedance at ray-parameter 0s/km. These results are compared with the well-log synthetic ray impedance values at the well location (CDP

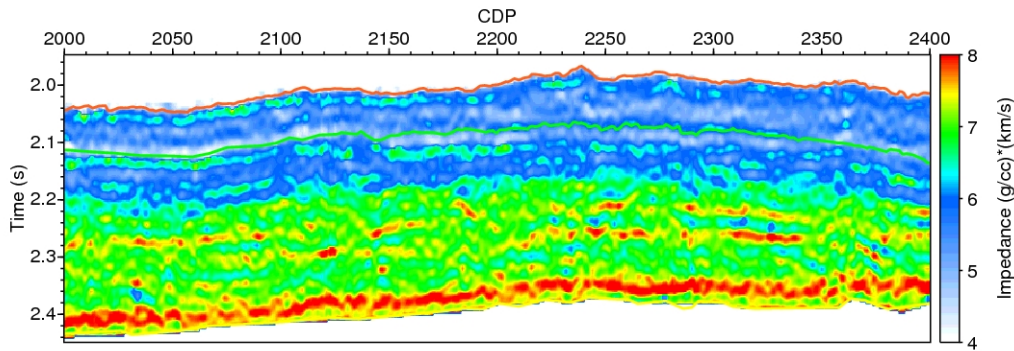
2232), which are displayed as the black curves in Figure 4.6. The red curves there are the inverted ray impedance and extracted from the results shown in Figure 4.5. The blue curves denote the initial ray impedance model traces extracted from the models in Figure 4.4.



(a)



(b)



(c)

**Figure 4.5** Ray impedance inversion results with different ray-parameter values at (a) 0.05 s/km and (b) 0.2 s/km. (c) The inverted acoustic impedance.

From these ray impedance results, we can not expect to see details that are not present on the original seismic profiles. After the reflectivity inversion depicted in Chapter 3,

the bandwidth of seismic profiles is expanded because of the compression in wavelet shapes, no new seismic events can be created, i.e., all the finer scale details presented in the inversion results here originate from the seismic profiles.

According to the previous research in this area (e.g. Avseth 2000), the oil reservoir in this well emerges from the Top Heimdal (TWT  $\sim 2.07$ s), with the cap-rock being silty shale. The pay zone consists of two facies which are fairly different in lithology and hence there is a strong reflection interface between them (TWT  $\sim 2.08$ s). In this well, the upper part of the reservoir is mainly clean sand characterised by relatively lower ray impedance values and the lower part is silty sand which has higher ray impedance values compared with the cap-rock and the top clean sand. The combined thickness of the whole reservoir is about 35 meters in depth, which is beyond the theoretical seismic resolution criterion of one-fourth wavelength (The nominal velocity in this area is 2500m/s and the principal frequency is 25Hz). From the inverted ray impedance profiles (Figure 4.5), the reservoir as a whole is mainly distinguished as a low ray-impedance zone located between CDP 2150 and CDP 2350, just below the Top Heimdal which is denoted by the green curve in each image.

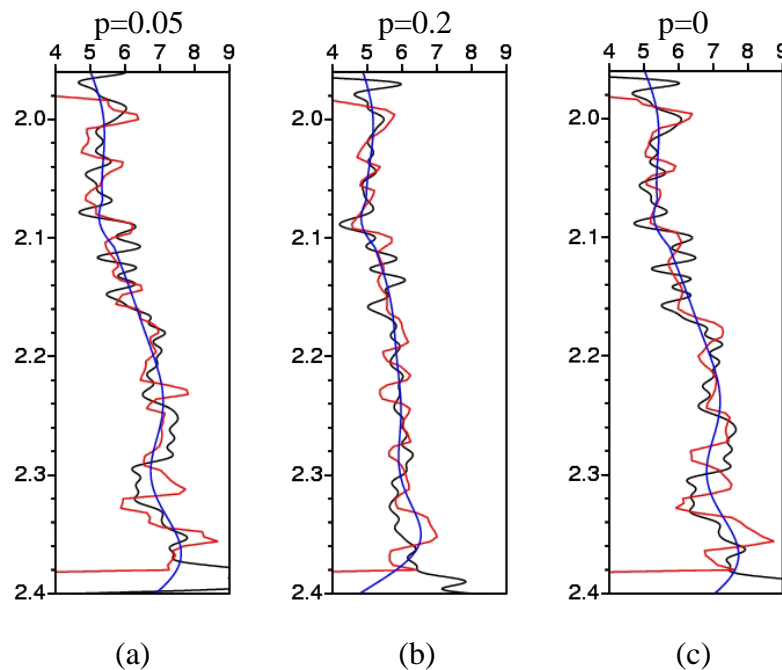


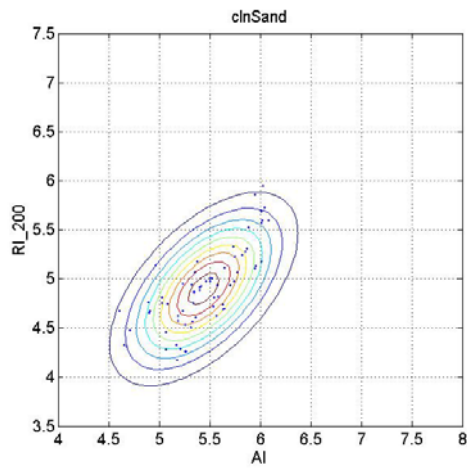
**Figure 4.6** Ray impedance inversion results (red curves) compared with the initial models (blue curves) and the synthetic values from the well-logs (black curves). (a) – (c) are corresponding to (a) – (c) in previous Figures 4.4 - 4.5.

From the comparisons displayed in Figure 4.6, generally all the inversion results fit the low frequency variations of the well log synthetics but the discriminability of the inversion results is limited by seismic resolution. In Figure 4.6a, the whole reservoir (TWT ~2.07s - ~2.10s) can be distinguished as two different parts from the inversion result however in Figure 4.6b and 4.6c it is characterised by low impedance values as a whole. This is because the two parts of the reservoir are very different in elastic properties and neither of them is thick enough to be beyond the seismic resolution. They can only be discriminated as a whole or through combinations with adjacent rocks. Considering the consistency of the inversion results, I will take the inverted ray impedance profile with ray parameter 0.2 s/km (Figure 4.5b and 4.6b) and the acoustic impedance profile (Figure 4.5c and 4.6c) in the following analysis.

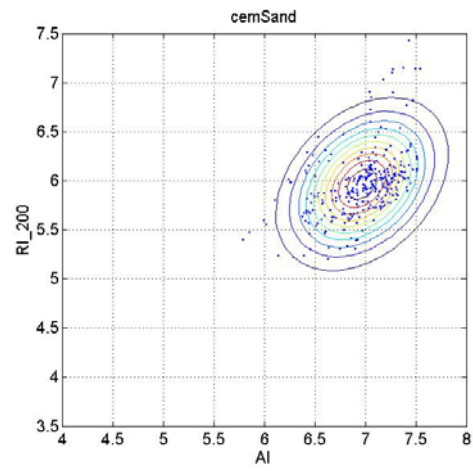
### **4.3 Lithology discrimination from the ray impedance inversion result**

Ray impedance is an elastic parameter which can indicate the lithological property of a rock. It has been demonstrated in Chapter 1 that the crossplot of RI and AI is preferable to discriminate different facies rather than the crossplot between EI and AI from a modelling perspective of view. However it will be even more useful if we can discriminate different rock properties from the ray impedance inversion results.

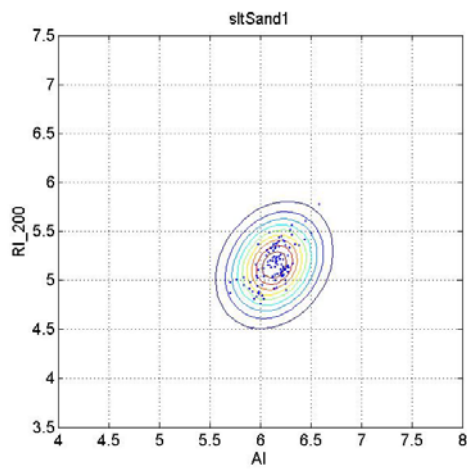
First I generate the bivariate probability density functions (PDFs) of acoustic impedance (AI) versus ray impedance at 0.2s/km (RI\_200) in Figure 4.7 for the six different facies identified in the well. These bivariate PDFs are overlain with the corresponding bivariate scatter plot of each facies. The centre of each contour plot stands for the most likely set of AI and RI\_200 values for each facies. Each bivariate PDF suggests the probabilities of certain pairs of AI and RI\_200 values indicating certain rock types. From these bivariate PDFs, we can also observe that the variations of AI and RI\_200 combinations within a given facies, and for different facies the combinations can have overlaps in bivariate PDFs. However, the most likely set of AI and RI\_200 values for a given facies has a unique character in this well. For example, cemented sand (Figure 4.7b) will likely have relatively large values of both AI and RI\_200, whereas oil-bearing sands (Figure 4.7a and 4.7c) and oil-free shales (Figure 4.7e and 4.7f) will more likely have smaller values of AI but different RI\_200 values.



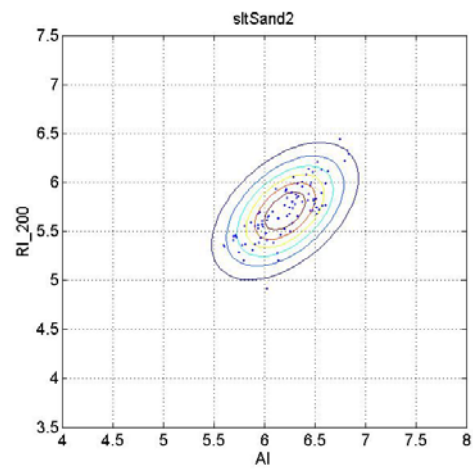
(a)



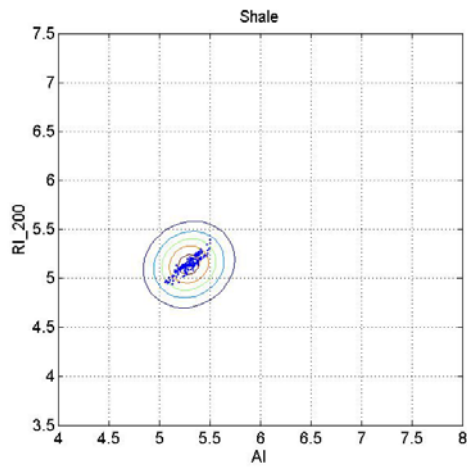
(b)



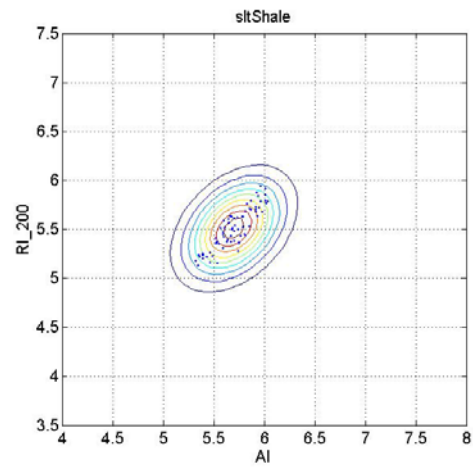
(c)



(d)



(e)



(f)

**Figure 4.7** Bivariate probability density functions for different facies. (a) Clean sand. (b) Cemented sand. (c) Silty sand (type 1, oil-bearing). (d) Silty sand (type 2, oil-free). (e) Shale. (f) Silty shale.

In order to better assess the discriminability for oil-bearing sand and oil-free shale, I lump all oil-bearing sand together into one group and all oil-free shale into another group, and plot them together in the same crossplot (Figure 4.8). These samples come from the well logs. In spite of some overlaps, the separation between oil-bearing sand and oil-free shale is fairly good, since the former tends to have relatively lower RI\_200 and larger AI values than the latter. But neither of the two properties is able to distinguish lithologies solely and hence both AI and RI\_200 values are needed to discriminate facies and possibly pore fluids in this case. A linear discriminant from the bivariate PDF values of shale and oil-bearing sand is set up for later lithology identification (solid line in Figure 4.8)

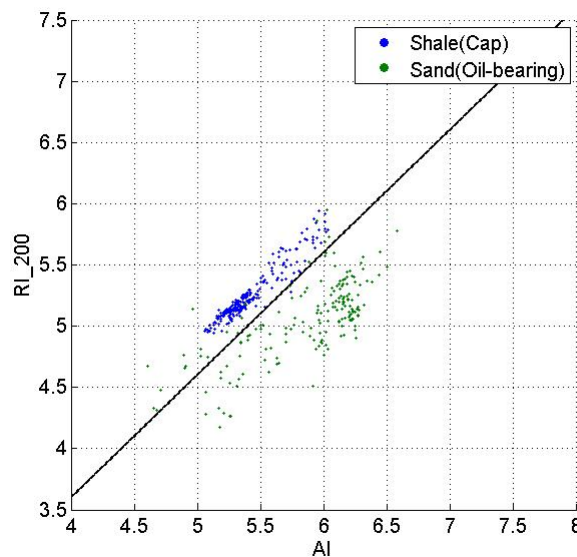
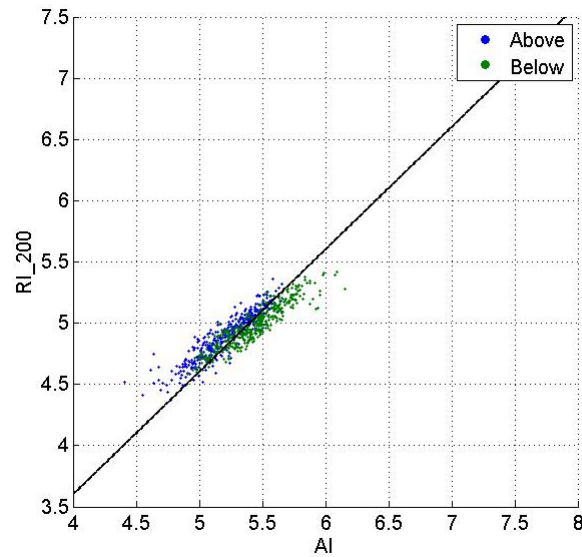


**Figure 4.8** Joint crossplot of oil-bearing sand and oil-free sand (generated from well logs). The solid line denotes where the discriminant values equal zero to separate these two facies.

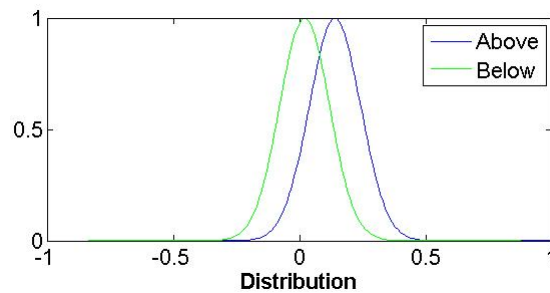
From the inversion result shown in Figure 4.5(b) and 4.5(c), I extract the sample ray-impedance values above and below the Top Heimdal horizon (the middle green curve) which indicates the top of the oil reservoir. The sample value at each CDP position (either below or above Top Heimdal) is the averaged one within a thickness of TWT 28ms. This thickness is about the real thickness of the reservoir (35m in depth with an average velocity ~2500m/s in this area). I use the average values based on the consideration that each of them is a robust representative in its position that a seismic



dataset can resolve for. The crossplot is shown in Figure 4.9a where the cap-rock (blue) and the reservoir sand (green) can be distinguished by the discriminant indicated by the black line in Figure 4.8. Although the separation between these two rock types is not as obvious as in the log-based result (Figure 4.8) since the values are averaged in a window, it is still very useful for us to interpret the inversion results. If we project these points along their major axis (the black line in Figure 4.8 and 4.9a), the distributions are shown in Figure 4.9b. The mean and standard deviation are 0.1405 and 0.1018 for the lithology above the horizon (blue) and 0.0203 and 0.0989 for the lithology below the horizon (green). So the difference of the two means over the average standard deviation is 1.1978, denoting a quantity for the lithology separation.



(a)



(b)

**Figure 4.9** (a) Crossplot of the inverted ray impedance values versus acoustic impedance values for the cap-rock (blue) and the reservoir sand (green). (b) Distributions after projecting the crossplot along the main axis (black line in a).

Figure 4.10 shows the extracted AI (top panels) and RI\_200 (middle panels) values and the predicted lithofacies (bottom panels) being present (a) above and (b) below the Top Heimdal horizon. The lithofacies is determined for each pair of AI and RI\_200 values at every CDP position (either above or below the Top Heimdal horizon), by following the linear discriminant set up before (solid line in Figure 4.8 and 4.9a). As expected, the cap-rock is mainly identified as oil-free shale and the reservoir mostly consists of oil-bearing sand. This result is very similar to the previous research of this area (e.g. Avseth, 2000).

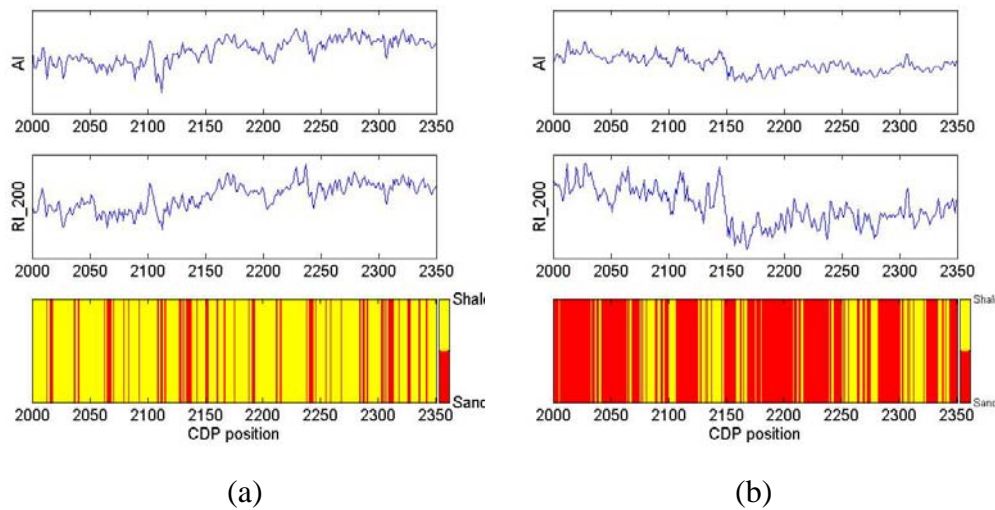


**Figure 4.10** Impedance inversion results and seismic lithofacies prediction (a) above and (b) below the Top Heimdal horizon.

#### 4.4 Comparison with elastic impedance inversion result

The workflow for elastic impedance (EI) inversion is very similar to ray impedance (RI) inversion. The major difference lies in transferring the CIP gather from the offset domain either to the ray-parameter domain (for RI inversion) or to the angle domain (for EI inversion). For EI inversion, again, I adopt the ray tracing scheme in the offset-domain CIP gathers to transform the data into angle domain and then sort them into common angle stacks. After that the EI inversion workflow is exactly the same as for RI inversion: mixed-phase wavelet estimation, Cauchy constraint reflectivity inversion and GLI impedance inversion.



For comparison with the RI inversion result at ray parameter  $p = 0.2s/km$ , the angle stack for EI inversion is chosen to be at 29 degrees, according to the average P-wave velocity of this area, 2.4 km/s (slightly different from 2.5 km/s in the reservoir area). This angle stack profile is displayed in Figure 4.11a, which looks similar to the constant-ray-parameter profile at  $p = 0.2s/km$  in Figure 4.2b. This similarity is because the angle range in generating this partial stack corresponds to the ray-parameter range of the constant-ray-parameter profile in Figure 4.2b, related by the P-wave velocity 2.4 km/s. Whereas the difference between these two profiles comes from the interval velocity variations in vertical direction, resulting in the same angle value at each depth in the common angle stack (Figure 4.11a) is not always corresponding to the same ray-parameter value in the constant-ray-parameter profile (Figure 4.2b).

Figure 4.11b and 4.10c display the initial model and the final result for EI inversion. Again the initial model is built explicitly from the three elastic models. The parameters in EI inversion are selected exactly the same as those in RI inversion whenever it is possible. Following this way, the difference in the final results between Figure 4.5b and 4.10c only originates from the two input profiles for either inversion: the seismic data (Figure 4.2b or Figure 4.11a) and the initial impedance model (Figure 4.3b or Figure 4.11b).

Now we can examine the lithology discriminability of the EI inversion result. From the data shown in Figure 4.11c, I extract the sample EI values above and below the Top Heimdal horizon at each CDP position by averaging within a thickness of the reservoir, in the same way as I did in generating Figure 4.9. These averaged values for all CDP locations are cross-plotted with the average AI values in the two layers (above or below Top Heimdal), which are shown in Figure 4.12a. Compared with the crossplot in Figure 4.9, we can observe that the inverted EI values for both facies are correlated with the inverted AI values in the same manner, making the discrimination of the cap-rock (blue) and the reservoir sand (green) difficult. If we project these points along their major axis (the black line in Figure 4.12a), the distributions are shown in Figure 4.12b. The mean and standard deviation are 0.1782 and 0.1080 for

the lithology above the horizon (blue) and 0.0922 and 0.0916 for the lithology below the horizon (green). So the difference of the two means over the average standard deviation is 0.8617, which is worse compared with the distribution shown in Figure 4.9b.

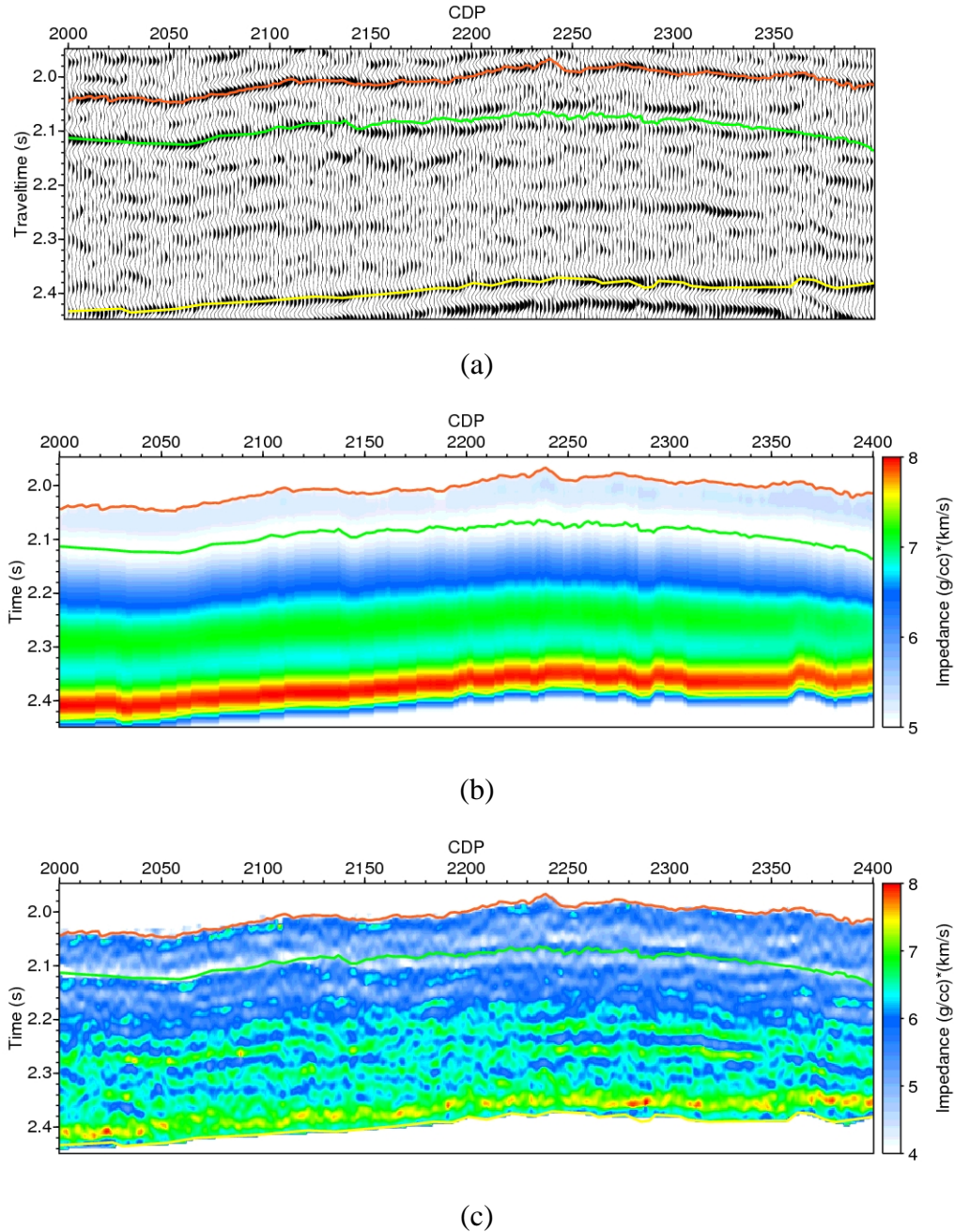
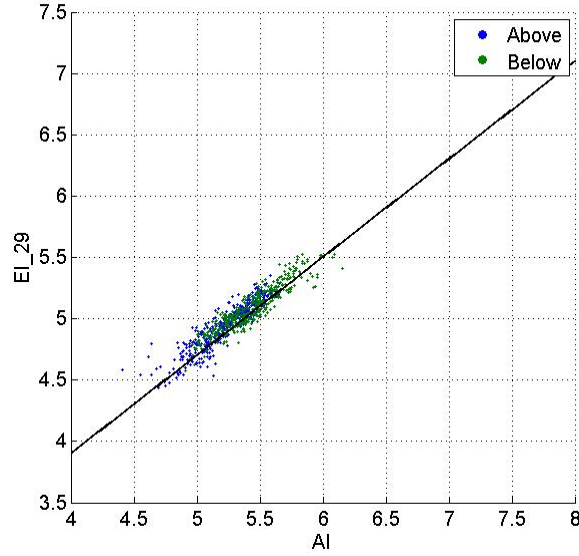
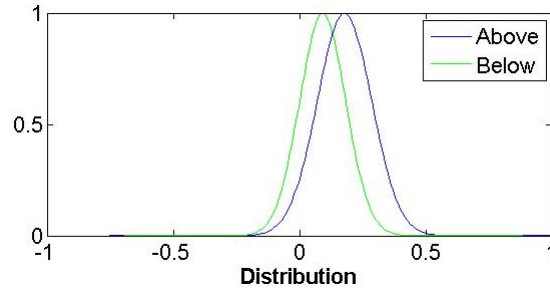


**Figure 4.11** (a) Common angle stack, (b) initial EI model and (c) inverted impedance profile for EI inversion at 29 degrees.



(a)



(b)

**Figure 4.12** (a) Crossplot of the inverted elastic impedance values versus acoustic impedance values for the cap-rock (blue) and the reservoir sand (green). (b) Distributions after projecting the crossplot along the main axis (black line in a).

Although the variations in EI inversion result (Figure 4.11c) are visibly similar to the variations in RI inversion result (Figure 4.5b), suggesting EI could be able to identify lithologies in this case study, however in the crossplot between the inverted EI and AI values, the two groups overlap more. In Figure 4.13, the AI (red), RI\_200 (green) and EI\_29 (blue) logs are plotted together, from which we can observe that for those sand facies which are well separated between AI and EI values (silt sand group1 and cemented sand), the separation between RI and AI is even better. This comparison further confirms what we have concluded from the modelling study in section 1.4 that the crossplot between RI and AI can discriminate lithologies better than the crossplot between EI and AI, as well explains that we can achieve a better discrimination of lithologies using the RI inversion results.

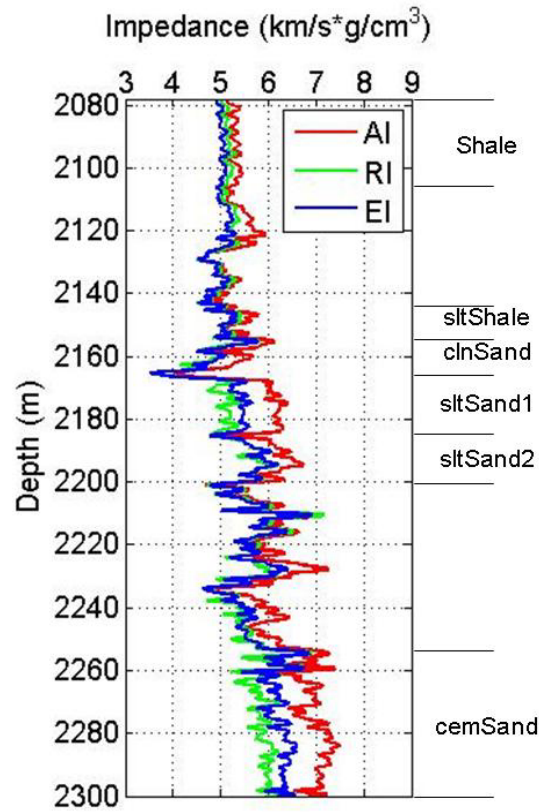


**Figure 4.13** AI, RI and EI logs plotted together to show a better discrimination ability of RI than EI.

#### 4.5 Discussion and conclusions

The uncertainty of our lithology prediction comes mainly from two aspects: the nonuniqueness of impedance inversion from seismic data and the overlap among bivariate PDFs of different facies.

For impedance inversion, and many other geophysical inversion problems as well, the nonuniqueness is a classical theme to be discussed. Seismic reflectivities are actually not sparse. The number of reflections within a seismic trace segment, whose duration is  $T$  and bandwidth is  $B$ , significantly exceeds the number of degrees of freedom  $2BT$ . Due to the restriction of seismic observation, the inversion is so non-unique that we have to impose a certain kind of constraint, sacrificing resolution in order to obtain stable results. No matter which constraint is imposed, the obtained layered models invariably have their layer properties averaged, and so is the further lithology

prediction. As a consequence, calibrating the inverted impedance by well log synthetics is necessary to have a reasonable inversion result.

Apart from the limitation of seismic resolution, the inversion nonuniqueness in GLI scheme also comes from the fact that the number of unknowns (impedance values) is one more than that of the knowns (reflectivities), supposing the sample intervals for both are identical. Hence the initial models need to be as close as possible to the real ones, reducing the nonuniqueness coming from the weak under-determined character of this inversion problem. If these models also serve as constraints, the inversion result will be more stable with further reduction of nonuniqueness, at the cost of further sacrificing resolution. Alternatively the impedance value of at least one position needs to be determined before inversion and fixed during inversion, making the number of unknowns no larger than the number of degrees of freedom in this inversion problem.

The uncertainty of lithology prediction also comes from the overlaps among bivariate PDFs of different facies. Hence the lithology identification at a single location can hardly mean anything to us. However the statistical response of a formation after the lithology identification can distinguish itself with others as Figure 4.9 and 4.10 show. This prediction, together with other analyses and interpretation results, should facilitate us in making decisions in hydrocarbon exploration and reservoir development.

Among the others, the picking of seismic horizons also represents a source of uncertainty. If the horizon is incorrectly picked, the initial impedance models will not be close to the real ones and hence will lead to biased impedance inversion results. Apart from the inaccuracy in the inversion results induced by horizon-picking mistakes, the predicted lithology may also not be the representative of the desired formation, as the horizon is wrongly positioned.

In the modelling research, the crossplot between ray impedance and acoustic impedance suggests that ray impedance can act as a good lithology indicator, as is described in section 1.4. However such crossplots are only available at those locations where well logs are available. Through inversion we can expand this discriminability

to a larger seismic scale which is more meaningful for us as we can predict lithologies wherever we have seismic data. In this way, the advantage of ray impedance over elastic impedance in discriminating different lithologies can be maintained and fully exploited.

## Chapter 5

### Simultaneous elastic parameter inversion from ray impedance

Elastic parameter inversion tried to exploit the amplitude variations of reflectivity in the prestack domain to infer those elastic attributes which may indicate pore fluids and lithological properties. Ostrander (1984) extracted Poisson's ratio to detect gas sands. Smith and Gidlow (1987) computed the relative change of P-wave and S-wave velocity by least-squares fitting of an approximation of the Zoeppritz equations. Fatti et al. (1994) used P-wave and S-wave impedance contrasts to detect gas in sandstone reservoirs. Goodway et al. (1997) suggested that Lamé's elastic parameters and their products with density could be useful tools in AVO analysis. Russell et al. (2003) introduced the attribute  $I_p^2 - cI_s^2$  with  $c$  being a function of local  $(\alpha/\beta)^2$ . The equations used in all the above elastic attribute inversions are obtained from Aki and Richards' (1980) linear simplification of the Zoeppritz equations and the reflectivity is a variable changing with angle values.

From Tarantola (1986) of elastic waveform inversion, we need three parameters to describe an elastic isotropic earth. However, in the long wavelength approximation of the model, P-wave and S-wave velocities are adequate parameters while in the short wavelength approximation, P-wave impedance, S-wave impedance and density are adequate. The inversion procedure is to optimise for P-wave related quantities first, then S-wave related quantities and finally for density. On the other side of elastic parameter inversion based on convolutional earth model, e.g. AVO or EI related elastic inversion, those parameters are normally inverted simultaneously for efficiency (e.g. Smith and Gidlow, 1987). Density in this case is not stable to be inverted and special cares are needed, e.g. absorbed into the velocity term in Smith and Gidlow

(1987).

From the ray impedance values obtained in Chapter 4, we can also further invert elastic parameters. As the definition of ray impedance explicitly contains P-wave velocity, S-wave velocity and density, we try to simultaneously invert these three elastic parameters first as all the other elastic parameters mentioned above are actually different combinations of the three basic elastic parameters.

### 5.1 Elastic parameter inversion from ray impedance

The ray impedance definition (1.22) is rewritten here for reference as

$$RI(\alpha, \beta, \rho; p) = \frac{\rho\alpha}{\sqrt{1-\alpha^2 p^2}} (1-\beta^2 p^2)^{2(\nu+2)}. \quad (5.1)$$

The objective function of elastic parameter inversion from ray impedance is

$$J(\mathbf{m}) = \|\mathbf{W}_d(\mathbf{RI}(\mathbf{m}) - \mathbf{RI}_0)\|^2 + \eta^2 \|\mathbf{W}_m(\mathbf{m} - \mathbf{m}_0)\|^2, \quad (5.2)$$

where  $\mathbf{m} = (\alpha, \beta, \rho)$  is the composite elastic parameter vector to be solved for,  $\mathbf{m}_0 = (\alpha_0, \beta_0, \rho_0)$  is the initial guess of the elastic parameter vector and  $\mathbf{RI}_0$  stands for the observed ray impedance values, i.e. the data.  $\mathbf{W}_d^T \mathbf{W}_d = \mathbf{C}_d^{-1}$  and  $\mathbf{W}_m^T \mathbf{W}_m = \mathbf{C}_m^{-1}$  are the inverses of the covariance matrix of noise (data misfits) and model respectively and  $\eta$  serves as the balancing factor for different terms. The application of the Gauss-Newton method leads to an iteratively updating scheme  $\mathbf{m}_{k+1} = \mathbf{m}_k + \delta \mathbf{m}_k$  to solve the regularised normal equations

$$\begin{aligned} & \left( (\mathbf{W}_d \mathbf{F})^T (\mathbf{W}_d \mathbf{F}) + (\eta \mathbf{W}_m)^T (\eta \mathbf{W}_m) \right) \delta \mathbf{m}_k \\ & = (\mathbf{W}_d \mathbf{F})^T \mathbf{W}_d (\mathbf{RI}_0 - \mathbf{RI}(\mathbf{m}_k)) - (\eta \mathbf{W}_m)^T (\eta \mathbf{W}_m) (\mathbf{m}_k - \mathbf{m}_0), \end{aligned} \quad (5.3)$$

where the Jacobian matrix  $\mathbf{F}$  contains the partial derivatives of the model response with respect to the model parameters. The solution to (5.3) is

$$\delta \mathbf{m}_k = (\mathbf{A}^T \mathbf{A})^{-1} \mathbf{A}^T \delta \mathbf{d}_k \quad (5.4)$$

where  $\mathbf{A}$  is the augmented matrix

$$\mathbf{A} = \begin{pmatrix} \mathbf{W}_d \mathbf{F} \\ \eta \mathbf{W}_m \end{pmatrix},$$

and



$$\delta \mathbf{d}_k = \begin{pmatrix} \mathbf{W}_d(\mathbf{RI}_0 - \mathbf{RI}(\mathbf{m}_k)) \\ -\eta \mathbf{W}_m(\mathbf{m}_k - \mathbf{m}_0) \end{pmatrix}.$$

## 5.2 Numerical test of elastic parameter inversion from ray impedance

### 5.2.1 Noise-free synthetic test

In order to verify that the iterative solution can converge to the true model in noise-free environment, I design a numerical test to demonstrate it. In Figure 5.1, the red curves denote the true elastic models in the following test, which are low-pass filtered well logs, overlain with the original ones (black curves). The filter is designed in the frequency domain with a cosine tapering function starting from 40Hz and ending at 50Hz to make the bandwidth of the elastic models close to the real seismic data. Using these elastic models, a ray impedance profile (Figure 5.2) is synthesised, indicating the ray impedance values varying with the ray parameters, as denoted by equation (5.1). Inverting elastic parameters from the noisy-free ray impedance traces, we should set the  $\eta$  in equation (5.4) to be zero, which means the second regularisation term in (5.2) is unnecessary and the inversion results should fully favour the data. This is equivalent to iteratively solving

$$(\mathbf{F}^T \mathbf{F}) \cdot \delta \mathbf{m}_k = \mathbf{F}^T (\mathbf{RI}_0 - \mathbf{RI}(\mathbf{m}_k)) \quad (5.5)$$

and then updating the model iteratively using  $\mathbf{m}_{k+1} = \mathbf{m}_k + \delta \mathbf{m}_k$ .

To recover the elastic models from the noise-free synthetic ray impedance traces, we need some initial guesses of the elastic models. Here I employ the linear regressions of the true models which are denoted by dashed lines in Figure 5.3. Again the red curves denote the true elastic models as in Figure 5.1. The inversion window starts from 2.05s and ends at 2.37 s. Three ray impedance traces at 0.05, 0.1 and 0.15 s/km are involved in this inversion. The inverted elastic parameter curves are denoted by black solid lines in Figure 5.3, which are not visible since fully overlain with the true models (red solid lines). We can see that for noise-free circumstance, it is possible to fully recover the elastic models from ray impedance traces starting with very simple initial guesses by minimising the objective function (5.2).

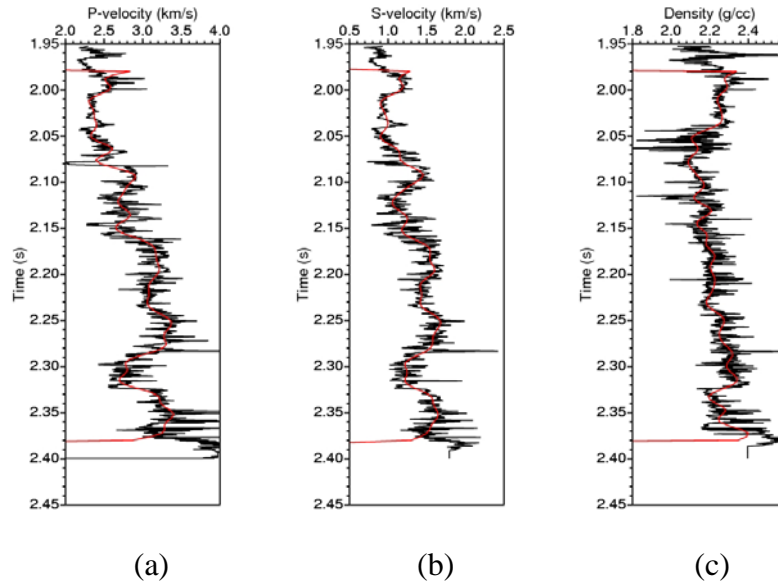


**Figure 5.1** Three well logs (black) overlain with the elastic models (red) which are low-pass filtered version of real well logs for (a) P-wave velocity, (b) S-wave velocity and (c) density.

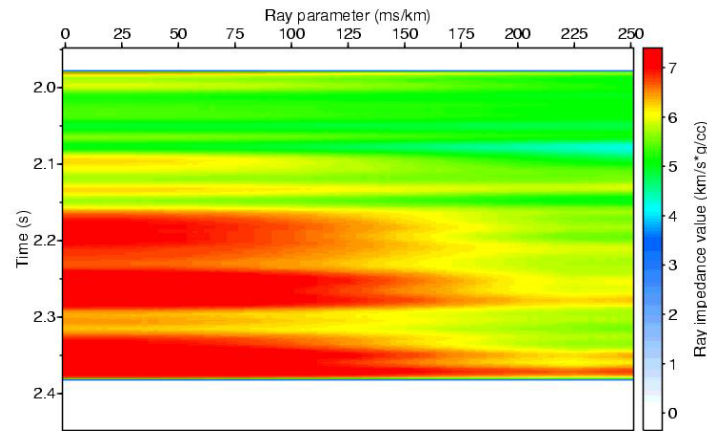


**Figure 5.2** Synthetic noise-free ray impedance traces indicating ray impedance values varying with ray parameters.

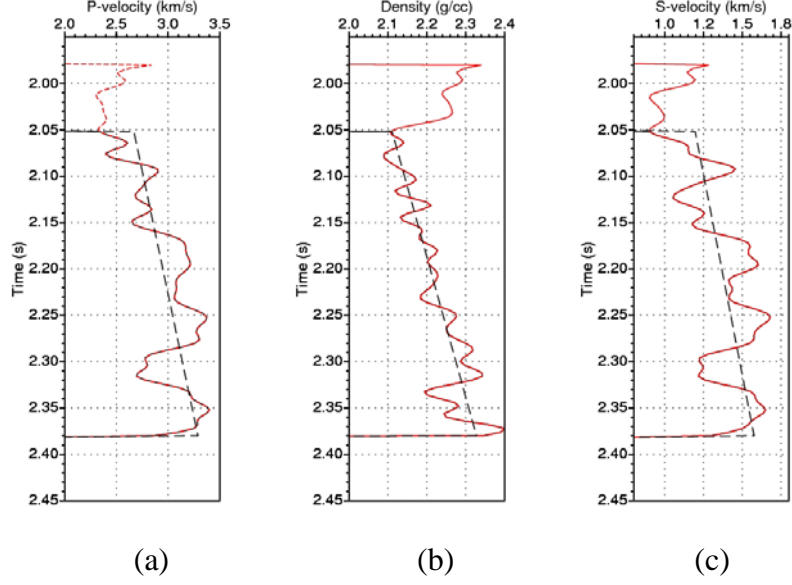


**Figure 5.3** Elastic inversion results for (a) P-wave velocity, (b) S-wave velocity and (c) density from the noise free ray impedance traces in Figure 5.2.

As the elastic parameter inversion is a multi-parameter inversion, I carry out an eigenvalue analysis by SVD (singular value decomposition) of the matrix  $\mathbf{A}^T \mathbf{A}$  to check the stability of this inversion (de Nicolao et al., 1993). Assuming in the last iteration the inverted models are already close to the true models, the three series of eigenvalues for matrix  $\mathbf{A}^T \mathbf{A}$  are calculated through SVD at each time sample point and formed together and plotted against time as three curves. These curves are displayed in Figure 5.4a. The curve of condition numbers, which denote the ratios between the largest and smallest eigenvalues for all time sample points, is plotted in Figure 5.4b. All the curves in Figure 5.4 are measured in dB (i.e. in logarithmic scale: 20 dB corresponding to a ratio of 10 in signal amplitude and 100 in energy). The large condition numbers indicate that the inversion using (5.5) is highly ill-posed and unstable so that even a small amount of noise will result in large parameter deviations and hence cause numerical instability. This problem becomes even worse if the range of ray parameters involved in the inversion is smaller, similar to the situation when the angle range is small in AVO inversion (see for example Wijngarssen and Berkhout, 1996). These kinds of inversions are normally addressed by regularisation by introducing the second constraint term in (5.2).

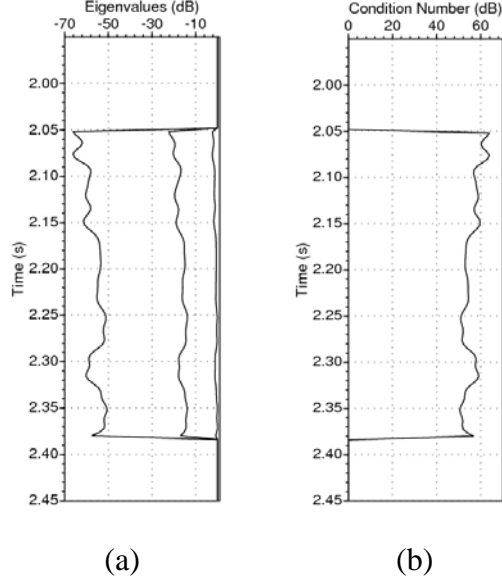


**Figure 5.4** Eigenvalue analysis for elastic parameter inversion from noise-free ray impedance traces. (a) The eigenvalue curves corresponding to the three elastic parameters. (b) The condition number curve.

### 5.2.2 Noisy synthetic test and the calculation of the weighting matrices

To be more practical, five percent Gaussian random noise is added to the ray impedance traces shown in Figure 5.2 and the noisy traces are shown in Figure 5.5. Again I try to invert the three elastic parameters from the noisy traces with the same starting models as in the noise-free inversion.

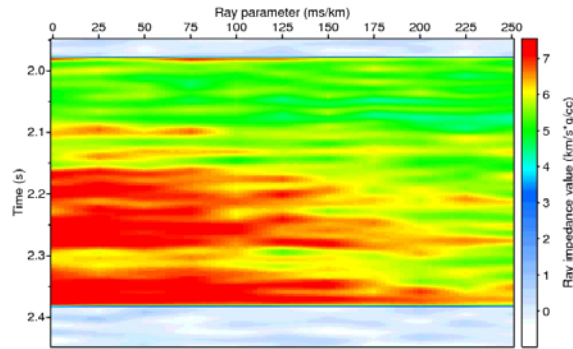


**Figure 5.5** Synthetic noisy ray impedance profile with two percent random noise added.

As the eigenvalue analysis in section 5.2.1 suggests, the multi-parameter inversion without regularisation is ill-posed and for noisy data, the balancing factor  $\eta$  should no

longer be zero. The weighting matrix  $\mathbf{W}_m$  in equation (5.4) and (5.5), which is the “square root” of the inverse covariance matrix, will play a key role in stabilising the multi-parameter inversion. The most straightforward way to generate the covariance matrix is to estimate the statistics from nearby well logs. In doing this, it is necessary to transform the appropriate well logs from the depth domain to the time domain, upscale to the seismic sampling level after being anti-aliasing filtered and then calculate the covariance from the P-wave, S-wave and density values over a proper time interval similar to the inversion window. Assuming there are  $N$  time samples in the calculation window, the  $3 \times N$  replicate matrix

$$\mathbf{X}_m = \begin{pmatrix} \alpha_1 & \cdots & \alpha_N \\ \beta_1 & \cdots & \beta_N \\ \rho_1 & \cdots & \rho_N \end{pmatrix}$$

contains the three-parameter vectors where the subscript represents the time index. The covariance matrix is estimated using

$$\mathbf{C}_m = \frac{(\mathbf{X}_m - \bar{\mathbf{X}}_m)(\mathbf{X}_m - \bar{\mathbf{X}}_m)^T}{N} \quad (5.6)$$

where  $\bar{\mathbf{X}}_m$  is formed with the expectation values of all the three parameters. To be more accurate,  $\bar{\mathbf{X}}_m$  should be time-variant. In the practice here, the initial models (dashed lines in Figure 5.3) are adopted as the time-variant expectations for each parameter.

If there is no appropriate well-log information available in the area that we carry out inversion, the covariance matrix still can be established through experimental or empirical petrophysics relationships. For instance, P-wave velocity can be related with S-wave velocity by the mud-rock relationship (Castagna et al. 1985), Gardner’s law (Gardner et al., 1974) defines a relationship between P-wave velocity and density, and there is also a similar relationship observed from experiments between S-wave velocity and density (Potter et al., 1998). As the covariance matrix  $\mathbf{C}_m$  is estimated from the deviations from the trend, at least two samples need to be calculated using the empirical relationships to form a deviation vector numerically.

For the three-parameter inversion depicted in this chapter, the covariance matrix is calculated from the real well logs shown in Figure 5.1 in a window between TWT

1.982 – 2.380s,

$$\mathbf{C}_m = \begin{pmatrix} 0.0432 & 0.0299 & -0.0005 \\ 0.0299 & 0.02424 & -0.008 \\ -0.0005 & -0.008 & 0.0012 \end{pmatrix}.$$

The units for velocity and density are  $m/s$  and  $k g/m^3$  respectively in the covariance matrix calculation.

In this multi-parameter inversion procedure, the data covariance matrix  $\mathbf{C}_d$  is a diagonal matrix

$$\mathbf{C}_d = \text{diag}\{\sigma_i^2\}, i = 1, \dots, M$$

where  $\sigma_i^2$  denotes the data misfit related to the  $i$  th ray-impedance dataset and  $M$  is the number of the ray-impedance datasets. In the  $k$  th iteration of this inversion procedure, the replicate matrix for data misfits is

$$\mathbf{X}_d = \begin{pmatrix} \varepsilon_{11} & \cdots & \varepsilon_{N1} \\ \varepsilon_{12} & \cdots & \varepsilon_{N2} \\ \vdots & \ddots & \vdots \\ \varepsilon_{1M} & \cdots & \varepsilon_{NM} \end{pmatrix}$$

where  $\varepsilon_{ij}$  is the data misfit at the  $i$  th time sample for the  $j$  th ray-impedance dataset.

I assume the misfits are zero-mean and only the diagonal elements of the covariance matrix calculated by

$$\mathbf{C}_d = \frac{\mathbf{X}_d \mathbf{X}_d^T}{N}$$

are retained, which means the misfits related to different ray-impedance datasets are uncorrelated. As the wavelet averaging effect has been largely removed in the reflectivity inversion, within each ray-impedance dataset, only a single  $\sigma_i^2$  denotes the data misfit is also reasonable. The data covariance matrix is updated after each iteration in the inversion procedure.

The elastic parameter inversion results are displayed in Figure 5.6. We can observe that the recovery of P-wave velocity and S-wave velocity is satisfactory with high accuracy while density can only be approximately recovered. From the eigenvalue and condition number analyses for matrix  $\mathbf{A}^T \mathbf{A}$ , which are shown in Figure 5.7(a)

and (b), we can find that the stability of this inversion has been improved significantly by enabling the second constraint term in equation (5.4). The poor performance of density inversion result, especially between 2.27s - 2.38s where the convergence direction is opposite to what it should be, is due to the covariance between density and P-wave velocity or S-wave velocity is positive for the whole window, although it is not true for this specific portion. Nevertheless the convergence curve denoting the residuals of  $\|\mathbf{RI}(\mathbf{m}) - \mathbf{RI}_0\|^2$  after each iteration is plotted in Figure 5.8, indicating the convergence rate is fast for the Gauss-Newton method.

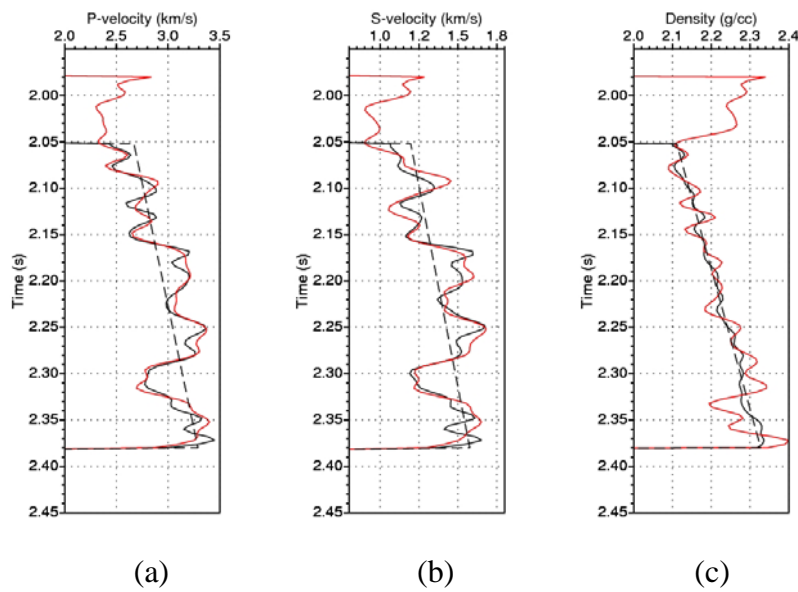


**Figure 5.6** Elastic parameter inversion results from noisy ray impedance traces for (a) P-wave velocity, (b) S-wave velocity and (c) density. Red: true model. Black solid: Inverted. Black dashed: initial model.

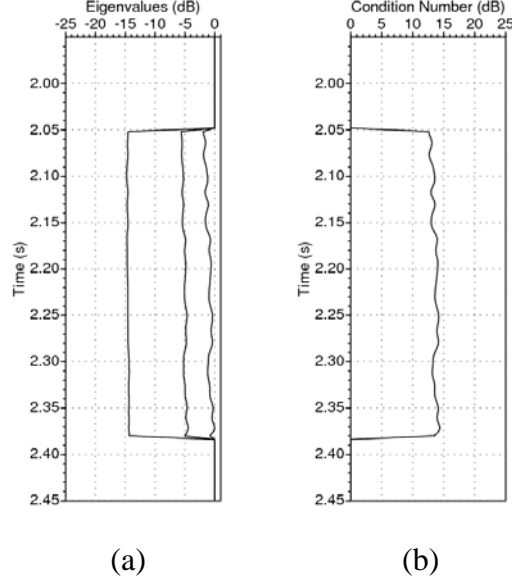


**Figure 5.7** Eigenvalue analysis for elastic parameter inversion from noisy ray impedance profiles. (a) The eigenvalue curves corresponding to the three elastic parameters. (b) The condition number curve.

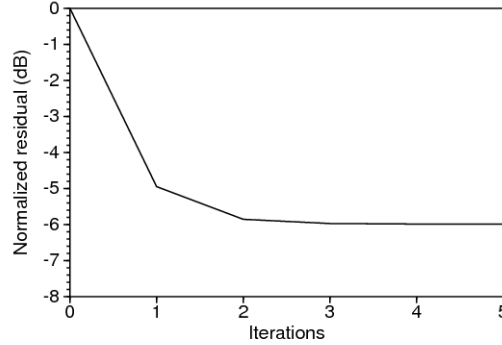


**Figure 5.8** Convergence curve of the three-parameter inversion from noisy data.

### 5.2.3 Uncertainty and resolution analysis

The uncertainty of the parameter updating estimate  $\delta \mathbf{m}$  in (5.4) can be depicted by the matrix  $(\mathbf{A}^T \mathbf{A})^{-1}$ , which is the covariance matrix of the estimated  $\delta \mathbf{m}$ . The diagonal element of  $(\mathbf{A}^T \mathbf{A})^{-1}$  represents the variance of each parameter-updating estimate in  $\delta \mathbf{m}$ . The off-diagonal element stands for the degree of correlation between these errors (Menke, 1984). For the final iteration, the relative standard deviations of the three parameter-updating estimates are plotted versus time in Figure 5.9. The references for these curves are the updated models.



It is also desirable for us to know to what extent the constraint (the second term in 5.2) influences the solution. Adopting the method of Wijngaarden and Berkhout (1996), for each parameter, the uncertainty of the constrained solution is compared to the uncertainty of the estimate when constraints are excluded ( $\eta = 0$  in 5.2). The ratio between these two uncertainty estimates,

$$\sqrt{\frac{(\mathbf{A}^T \mathbf{A})_{ii}^{-1}}{(\mathbf{F}^T \mathbf{F})_{ii}^{-1}}}$$

is defined as resolution, giving a quantitative sense of how much the solution is being determined by the data and how much by prior knowledge. The resolution value should be between 0 and 1. A resolution value approaching zero means that the inversion result depends hugely on the prior information and a resolution value of nearly 1 means that the inversion result is mainly determined by the data. For a reasonable inversion scheme, the estimate should greatly come from the data rather than the constraint, which makes the resolution approximately being 1.

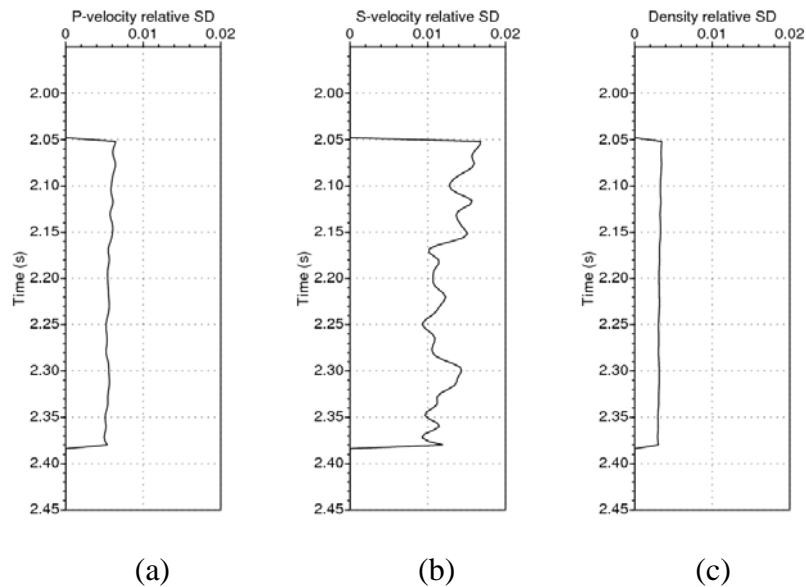


**Figure 5.9** The relative standard deviation curves for the three updating estimates in the last iteration of (a) P-wave velocity, (b) S-wave velocity and (c) density.

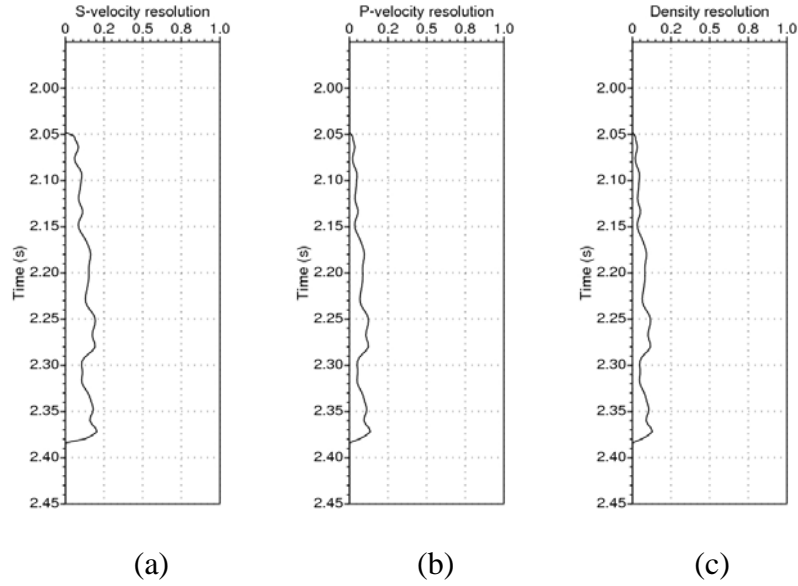


**Figure 5.10** The resolution analysis for this linearised inversion in the last iteration. The three resolution curves are for (a) P-wave velocity, (b) S-wave velocity and (c) density.

The uncertainty analysis shown in Figure 5.9 indicates that the inversion results are acceptable in terms of estimation error. However the resolution analysis shown in Figure 5.10 tells us that the inversion results mainly come from the constraints. This is because, for this ill-conditioned inversion problem, a large  $\eta$  value is adopted in order to have a stable solution. It is also clear now why the density inversion result in Figure 5.6 is very much correlated with the other two parameters.

Using offset limited data, which actually has a limitation on the range of angle or ray-parameter, e.g. for angle values up to 35-40 degrees, the three-parameter inversion can not unambiguously resolve all the elastic values (Stolt and Weglein, 1985; Debski and Tarantola, 1995). Many theoretical and numerical studies (Ursin and Tjaland, 1992; De Nicolao et al., 1993) have demonstrated that only two parameters can be effectively determined from this kind of data. Our experiments have confirmed this point through the three-elastic-parameter inversion from ray impedance. For a robust inversion in practice, one usually pursues a scheme to invert two parameters which have the most influence on offset/angle/ray-parameter dependent data, while the third one can be neglected or absorbed within the range of recorded offsets. The two parameters that are probably most frequently inverted are P-impedance and S-

impedance (Fatti et al., 1994) or intercept and gradient (Shuey, 1985). From the definition of ray impedance, it is straightforward to invert P-impedance and S-impedance simultaneously.

### 5.3 Two-parameter elastic inversion from ray impedance

For simultaneous inversion of P-impedance and S-impedance from ray impedance (other elastic parameter combinations may apply), equation (5.1) needs to be reformed as

$$\begin{aligned}
 RI(\alpha, \beta, \rho; p(\theta)) &= \frac{\rho\alpha}{\sqrt{1-\alpha^2 p^2}} (1-\beta^2 p^2)^{2(\nu+2)} \\
 &= \frac{\rho\alpha}{\cos\theta} \left(1 - \frac{\beta^2}{\alpha^2} \sin^2 \theta\right)^{2(\nu+2)} \\
 &= \frac{I_p}{\cos\theta} \left(1 - \frac{I_s^2}{I_p^2} \sin^2 \theta\right)^{2(\nu+2)}
 \end{aligned} \tag{5.7}$$

where  $\nu$  uses the same value as derived in Chapter 1.3 for the same dataset. Please note that  $\theta$  here is the exact P-wave incident angle rather than the average across the interface. Although the reflectivity appears to be a function of angle, it is different from the elastic impedance as the angle here is varying with P-wave velocity to maintain the ray parameter a constant for each constant-ray-parameter profile. Using a similar inversion scheme as equations (5.2) – (5.5), the P-impedance and S-impedance will be simultaneously inverted.

This algorithm is first tested on the same noisy synthetic dataset shown in Figure 5.5 and the inversion results are displayed in Figure 5.11. As expected, both of the two parameters can be recovered with high accuracy. This two-parameter inversion is fairly stable as the eigenvalue analysis shown in Figure 5.12 indicates the condition number is only about 3 (10dB). The convergence speed (Figure 5.13) is faster than the three-parameter inversion (Figure 5.8). The variances of both parameter-updating estimates are reasonably low (Figure 5.14) and most importantly, the resolution analysis shown in Figure 5.15 indicates that the solution mainly comes from the data rather than the constraint, making the results convincing.

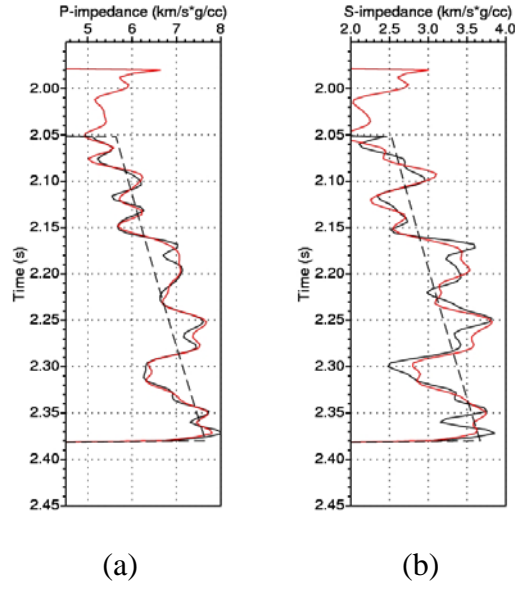


**Figure 5.11** Elastic inversion results for (a) P-impedance and (b) S-impedance from noisy ray impedance traces. Red: true model. Black solid: Inverted. Black dashed: initial model.

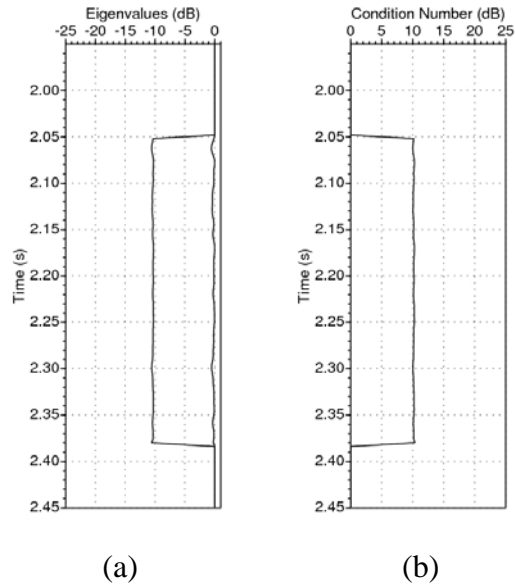


**Figure 5.12** Eigenvalue analysis for two-parameter elastic inversion from noisy ray impedance traces. (a) The eigenvalue curves corresponding to the two elastic parameters. (b) The condition number curve.



**Figure 5.13** Convergence curve of the two-parameter inversion from noisy data.

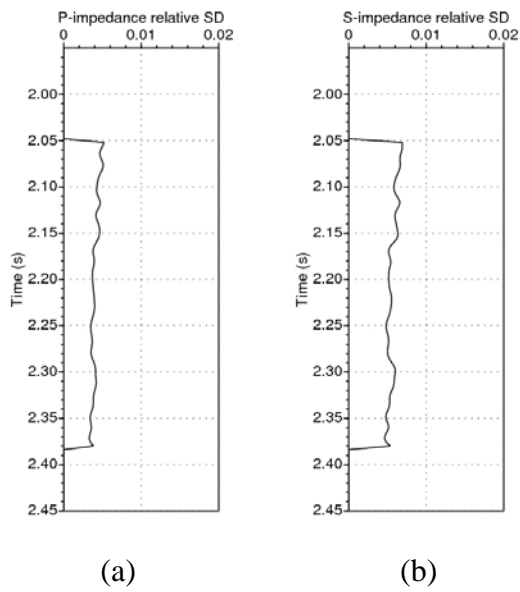


**Figure 5.14** The relative standard deviations for the two updating estimates in the last iteration of (a) P-impedance and (b) S-impedance.

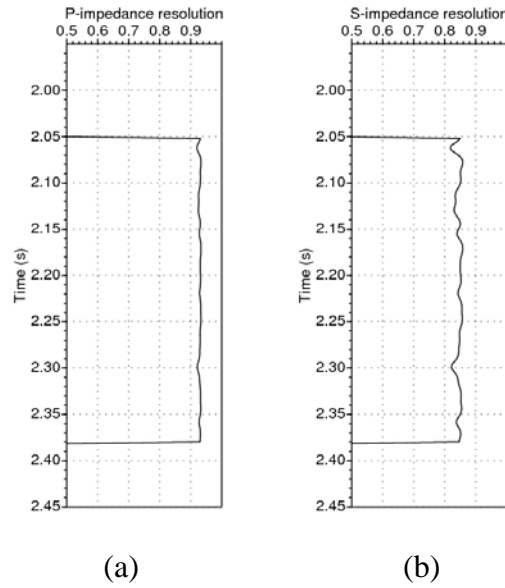


**Figure 5.15** The resolution analysis for the two-parameter inversion in the last iteration. The two resolution curves are for (a) P-impedance and (b) S-impedance.

#### 5.4 Two parameter elastic inversion from ray impedance -- real data application

The synthetic test of two-parameter elastic inversion from ray impedance has successfully recovered the P-impedance and S-impedance with high accuracy, low uncertainty and high resolution. Now this inversion is carried out on the real data. In this iterative inversion, the initial models for P-impedance and S-impedance are calculated from the P-velocity, S-velocity and density models, which are already obtained in section 4.2.1. Figure 5.16 displays the five inverted ray impedance profiles at different ray parameter values, which are obtained using the ray impedance inversion method depicted in Chapter 4. From these five profiles, I obtain the elastic inversion results for P-impedance and S-impedance which are shown in Figure 5.17. The whole inversion procedure is implemented within four iterations and after the third iteration the collective residual remains nearly unchanged (Figure 5.18). This reservoir (between CDP 2150 and CDP 2350, below Top Heimdal, the middle green curve) is characterised by low P-impedance and S-impedance. At the well location (CDP 2232), the inverted attributes (red) have a good correlation with the well logs (black) shown in Figure 5.19 especially at the reservoir position (TWT ~2.07s - ~2.10s). In the last iteration, the eigenvalue and condition number analyses (Figure

5.20) on the trace near the well indicate this inversion is fairly stable. The uncertainty and resolution analyses are shown in Figure 5.21 as important QC methods, which ensure the inversion results are trustworthy.

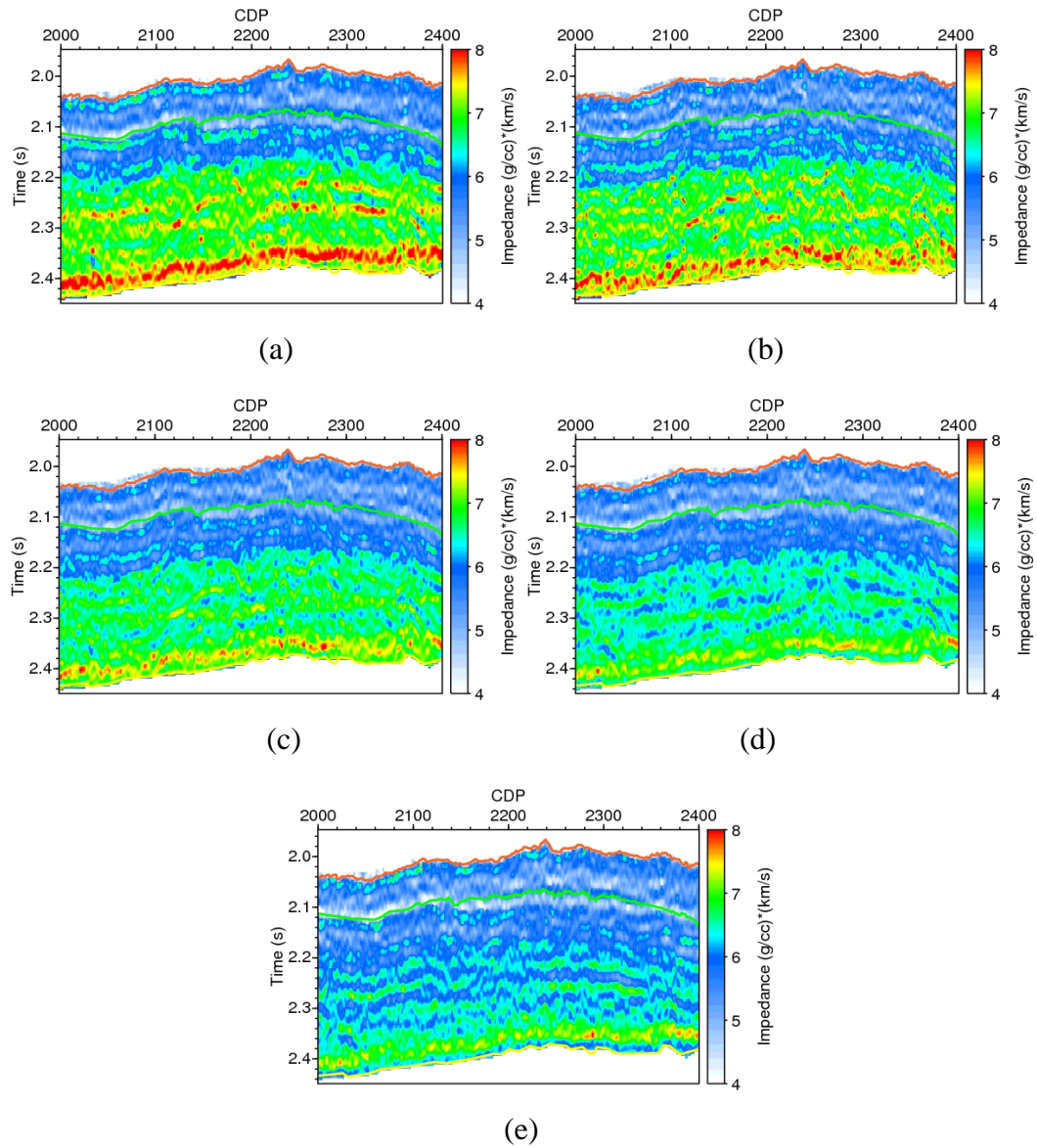
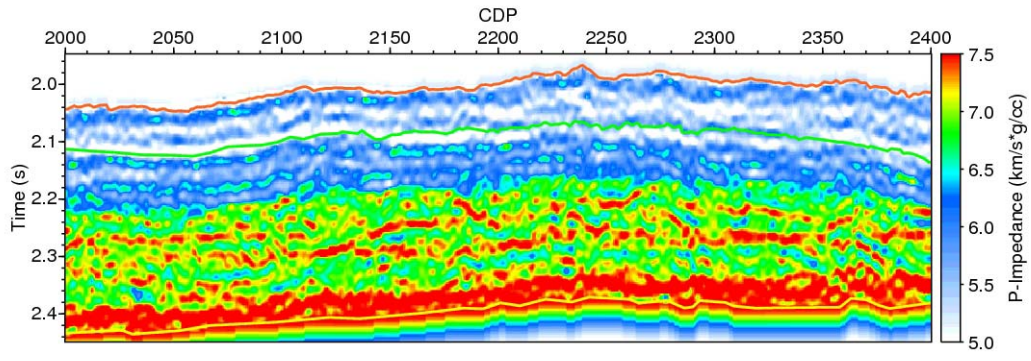
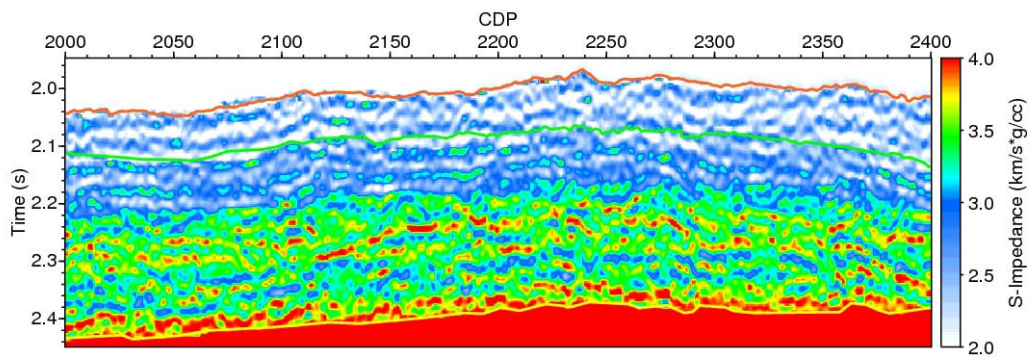


**Figure 5.16** Ray impedance inversion results at different ray parameter values: (a) 0, (b) 0.05, (c) 0.1, (d) 0.15 and (e) 0.2 s/km.



(a)



(b)

**Figure 5.17** Elastic inversion results for (a) P-impedance and (b) S-impedance.

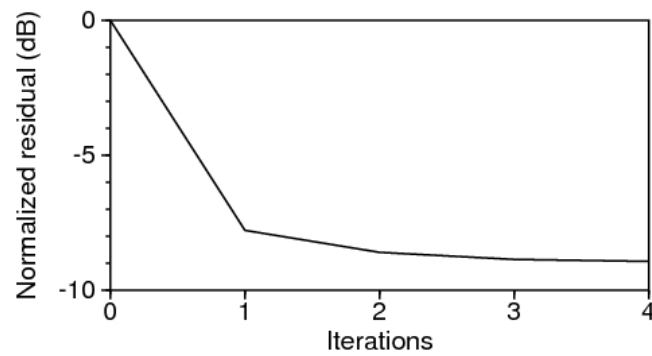


**Figure 5.18** The normalised convergence curve for the real data inversion.



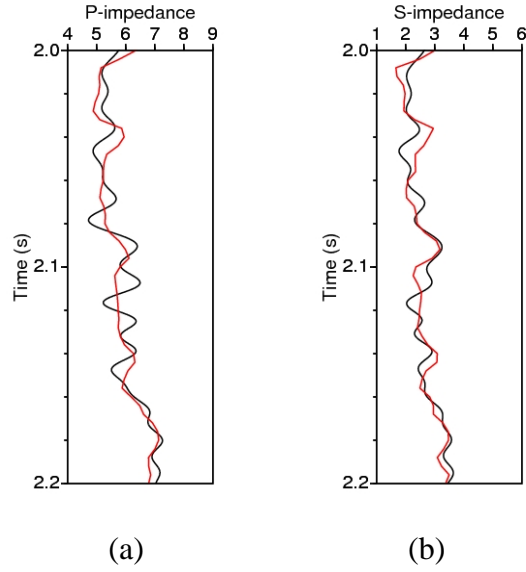


**Figure 5.19** Comparison between the inverted attributes at CDP 2232 and the well logs for (a) P-impedance and (b) S-impedance.

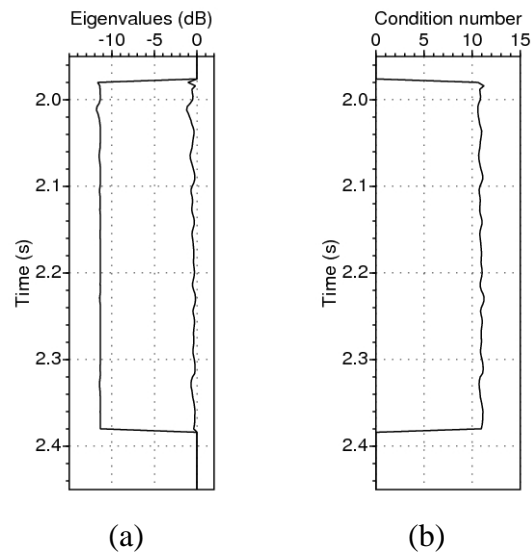


**Figure 5.20** (a) Eigenvalue and (b) condition number analyses at CDP 2232 for the two-parameter elastic parameter inversion.

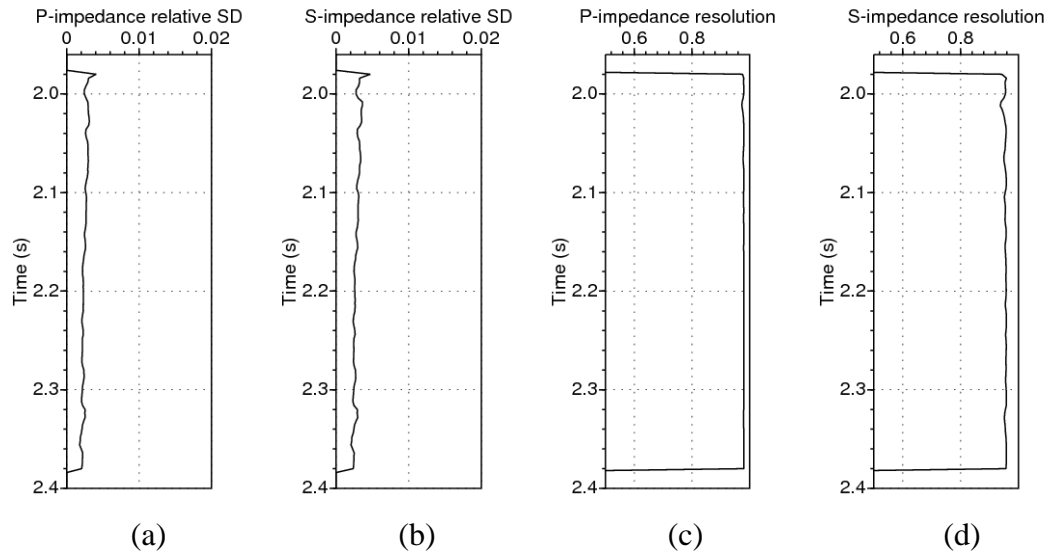
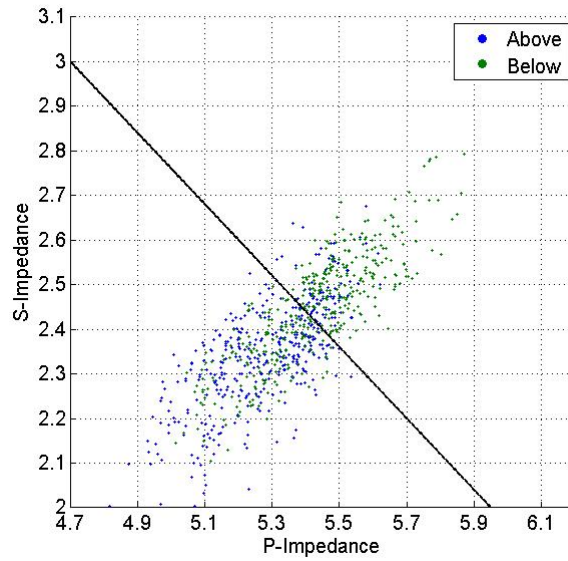
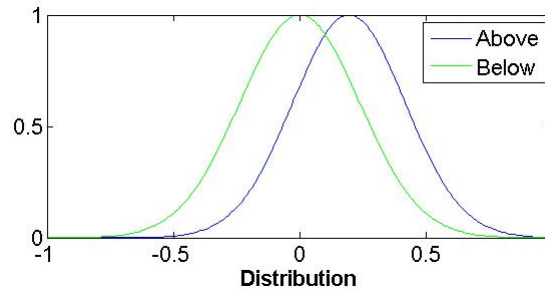


**Figure 5.21** The uncertainty analyses for (a) P-impedance and (b) S-impedance and the resolution analyses for (c) P-impedance and (d) S-impedance at CDP 2232.

From the inversion results shown in Figure 5.17, I extract the sample P-impedance and S-impedance values above and below the Top Heimdal horizon (the middle green curve) and generate a crossplot (Figure 5.22a) following the same way as in Chapter 4.3. The separation between these two formations is best described by the major axis denoted by the black line in Figure 5.22(a). Along this axis, the projections are generated in Figure 5.22(b) which can facilitate us in interpreting the inversion results.



(a)



(b)

**Figure 5.22** (a) Crossplot of the inverted S-impedance versus P-impedance values for the cap-rock (blue) and the reservoir sand (green). (b) Distributions after projecting the crossplot along the main axis (black line in a).

## 5.5 Discussion and Conclusions

Ray impedance itself is able to indicate lithology and through it we can also invert other elastic parameters, which may be more familiar for interpretation. For simultaneous inversion of P-wave velocity, S-wave velocity and density, I have demonstrated that, like other inversion schemes, they can not be simultaneously determined with normal acquisition design. However if the parameters to be inverted are reduced to two, we can have reliable results for lithological interpretation.

In traditional two-parameter inversion schemes, many authors (e.g. Shuey 1985, Smith and Gidlow 1987, and Fatti et al 1994) tried different approaches to rearrange

the Aki and Richards (1980) linearised approximation to the Zoeppritz equations to solve for different elastic attributes. In applying these schemes, hard constraints are usually imposed either explicitly or implicitly to have a stable solution for the inversion problem. Smith and Gidlow (1987) utilised the Gardner equation (Gardner et al., 1974) to remove the density reflectivity in order to improve the stability of the inversion. Both the Shuey (1985) and Fatti et al. (1994) equations are generally adopted by using only the first two terms while implicitly constraining the 3rd term's reflectivity to be zero. In all means the density term is either absorbed through empirical relationship (Smith and Gidlow, 1987) or truncated under the assumption of small incident angles (Shuey, 1985; Fatti et al., 1994). However in our two-parameter inversion from ray impedance, the density term is naturally absorbed into the P-impedance and S-impedance terms by introducing the true P-wave incident angle  $\theta$ , which is related to the ray parameter through P-wave velocity. This P-wave velocity field can be the one I used in ray tracing (section 1.5.4) or the initial P-wave model obtained in section 4.2.1 for previous inversions. The validity of this scheme has been verified by a similar synthetic test as the one depicted in section 5.2.1, in which the P-impedance and S-impedance can be fully recovered in the noise-free circumstance.

In this linearised iterative inversion scheme, the matrix  $\mathbf{A}$  contains the initial model information which can not be obtained from the band-limited seismic data but contributes the numerically major part of the final estimate. In this sense a fairer analysis should be restricted to estimates within the seismic bandwidth, i.e. the relative change of elastic parameters rather than the absolute parameter values. However from the intrinsic character of this inversion problem (see equation 5.1), the relative change of elastic parameters are not decoupled naturally as in those methods (e.g. Smith and Gidlow, 1987) using the Aki-Richards expression (Aki and Richards, 1980) for reflection coefficients. In addition, the resolution analysis does show the discriminability of good or bad inversion schemes, which is still useful in assessing an inversion algorithm.

## Chapter 6

### **Converted-wave ray impedance inversion and joint analysis with P-P wave ray impedance**

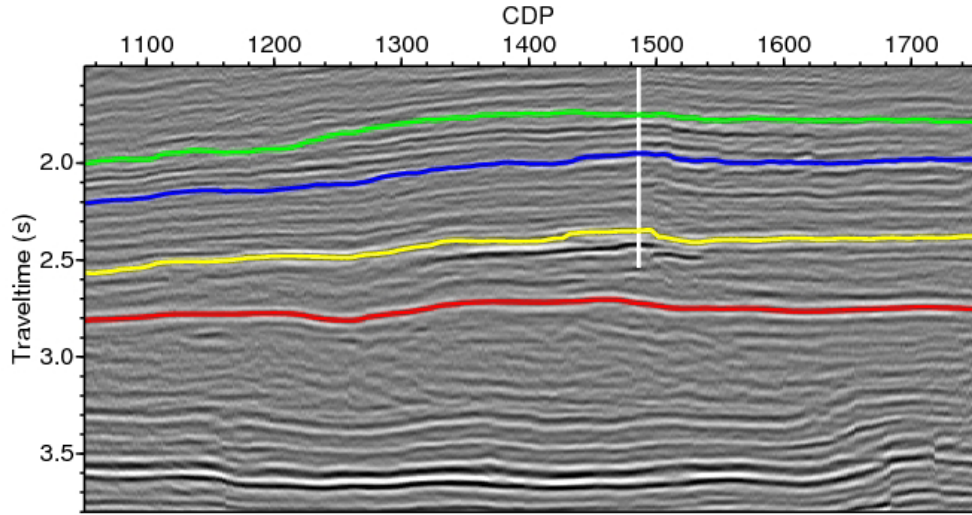
Nowadays P-wave reflection seismic surveying remains the primary method in hydrocarbon exploration. However multi-component seismic acquisition captures the seismic wavefield more completely than conventional single-component techniques and hence can help with fracture detection, imaging through gas clouds, lithology definition and fluid identification. As a consequence, multi-component surveying has developed rapidly, allowing converted P-S wave inversion and joint interpretation and analysis of P-P and P-S waves.

The so-called shear-wave elastic impedance (SEI), corresponding to elastic impedance (Connolly, 1999), has been derived as a quantity to link well logs with converted waves seismic data (Landrø et al., 1999). Duffant et al. (2000) extracted SEI from a North Sea dataset and showed how instantaneous  $\alpha/\beta$  can be obtained by combining SEI and EI. Converted P-S waves have also been used in identifying elastic rock properties (Jin et al., 2000; González, 2000; Wu, 2000; Zhu et al., 2000; Ramos and Castagna, 2001; etc). In this chapter, the concept of converted ray impedance (CRI) derived from the pseudo quadratic approximation of Zoeppritz equations for the P-S converted waves (Wang, 1999) is proposed. The relationship between CRI and RI is comparable to that between SEI and EI. In the second part of this chapter, a joint analysis of CRI and RI is demonstrated on identifying a tight gas reservoir of southwestern China.

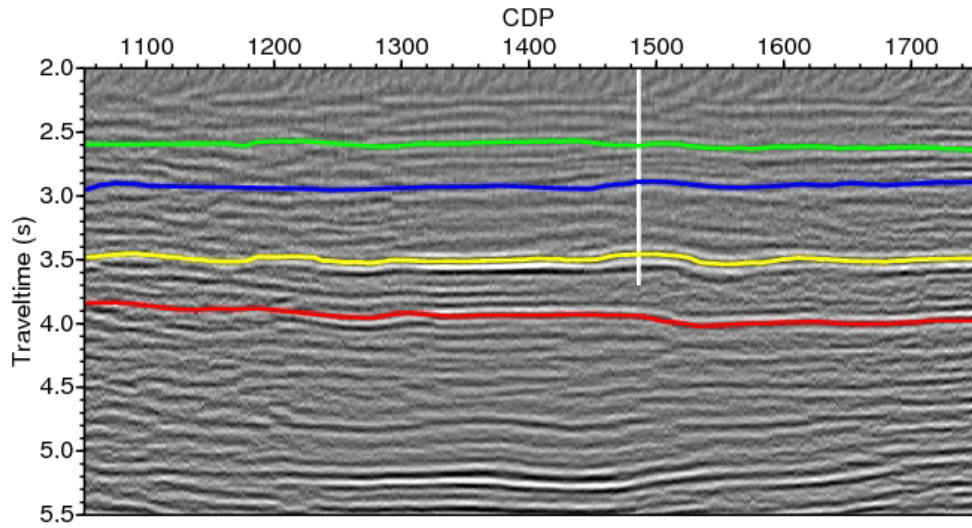
## 6.1 The dataset for this study

The dataset involved in this chapter comes from the west Sichuan basin, between the Longmen Mountains and Longquan Mountains, southwestern China. The major interest for us is the deep-trapped and very tight sand (gas) reservoir buried in the Xujiahe Group in the upper Triassic  $T3X^4$  and  $T3X^2$  (from shallow to deep) formations. Here  $T3$  denotes the upper Triassic,  $X$  stands for the Xujiahe Group and the superscript indicates the index of a group member. The whole  $T3X^4$  and  $T3X^2$  are about 600 and 500 m in thickness respectively with small strata dip angle ( $\leq 5^\circ$ ) and very low porosity ( $\sim 4\%$ ), consisting of predominantly continental clastic sediments (Gan et al., 2009). As the reservoir is very deeply buried and there exists a very thick near-surface low-velocity zone, which strongly attenuates and absorbs high frequency components, the bandwidths of the seismic reflections from target reservoirs are fairly narrow with low dominant frequencies (less than 20 Hz), resulting in a low resolution (1/4 wavelength,  $\sim 60$  m with a typical velocity of this area 4800m/s). However, as the purpose of this research is to carry out the joint P-P and P-S analysis using the novel ray impedance concept, the resolution issue is not my major concern.

The whole survey is recorded as 3D/3C. The main processing flow that has been applied on the dataset includes: noise attenuation (random noise, ground roll and guided waves), statics, surface consistent scaling, surface consistent deconvolution, phase-only Q compensation, time-variant filtering and prestack time migration. The stack section of a 2D line (P-P waves) across the well CX560 (located at CDP 1486) is displayed in Figure 6.1a. Four key horizons have been interpreted in this area: top of  $T3X^4$  (green), bottom of  $T3X^4$  (blue), top of  $T3X^2$  (yellow) and bottom of  $T3X^2$  (red), from top to bottom. The corresponding P-S wave section is displayed in Figure 6.1b in P-S travel time.



(a)



(b)

**Figure 6.1** (a) The P-P-wave stack section for the tight gas sand reservoir across the well CX560. (b) The corresponding P-S-wave stack section.

For the well CX560, several logs have been supplied including P-wave velocity, S-wave velocity, density, Gamma ray and resistivity (Figure 6.2). In this well,  $T3X^4$  is located between 3415 and 3968 m whereas  $T3X^2$ , which has not been fully penetrated, starts from 4740 m down to the end of the logs (5238 m). As we can see, the S-wave velocity log is only partially available, so that an empirical relationship (Castagna et al. 1985) between P-wave velocity ( $m/s$ ) and S-wave velocity ( $m/s$ )

$$\beta = 0.6325 \times \alpha - 222.0 m/s$$

is derived through a linear regression using the available data. This equation will be used in calculating S-wave velocity from P-wave velocity log where the former is not recorded. The well logs are then correlated to the P-P seismic data (Figure 6.3a) using the P-P time to depth curve supplied by the data provider.

The well-tie is also performed for the P-S stack section (Figure 6.3b) in a similar way as we do for P-P data. The correlation coefficients after the well-tie are 0.8213 and 0.7532 for P-P and P-S data respectively. The polarity of the converted wave data has been flipped so as to have a consistent convention as the P-P data. In the resultant P-S wave stacks an increase in both S-wave velocity and density will result in a peak, which is the same as P-P wave data. Now at the well location, we can confidently identify the correspondence between the P-P and P-S events and this relationship will later be established at other locations away from the well.

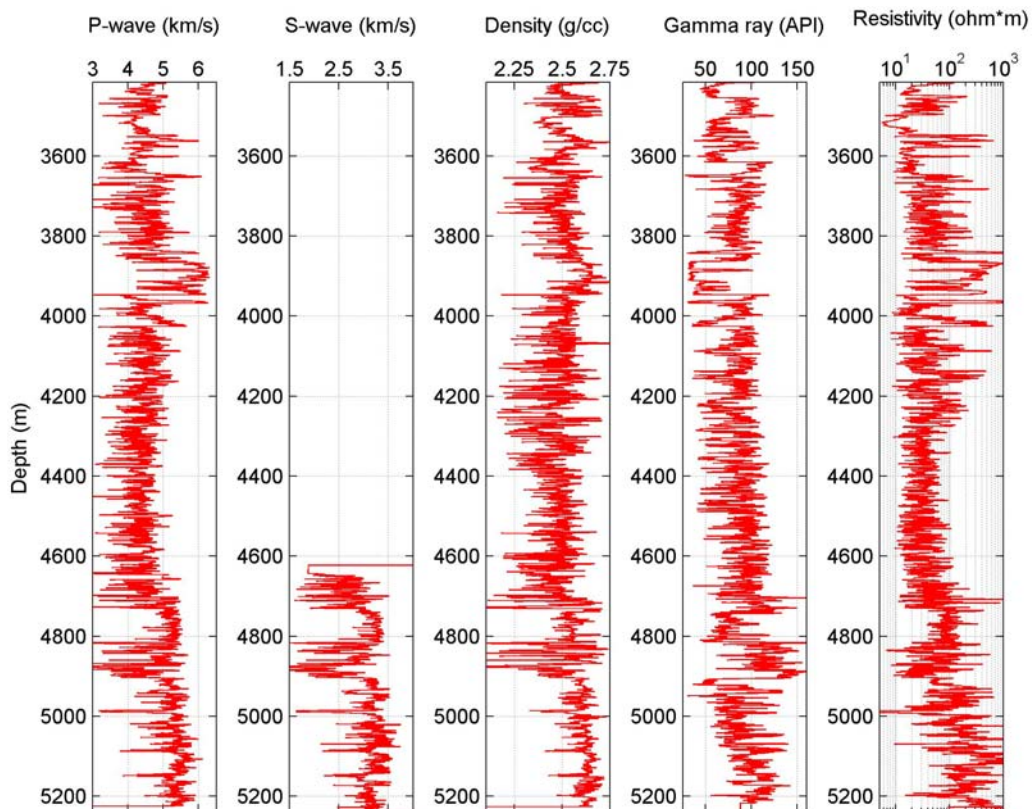
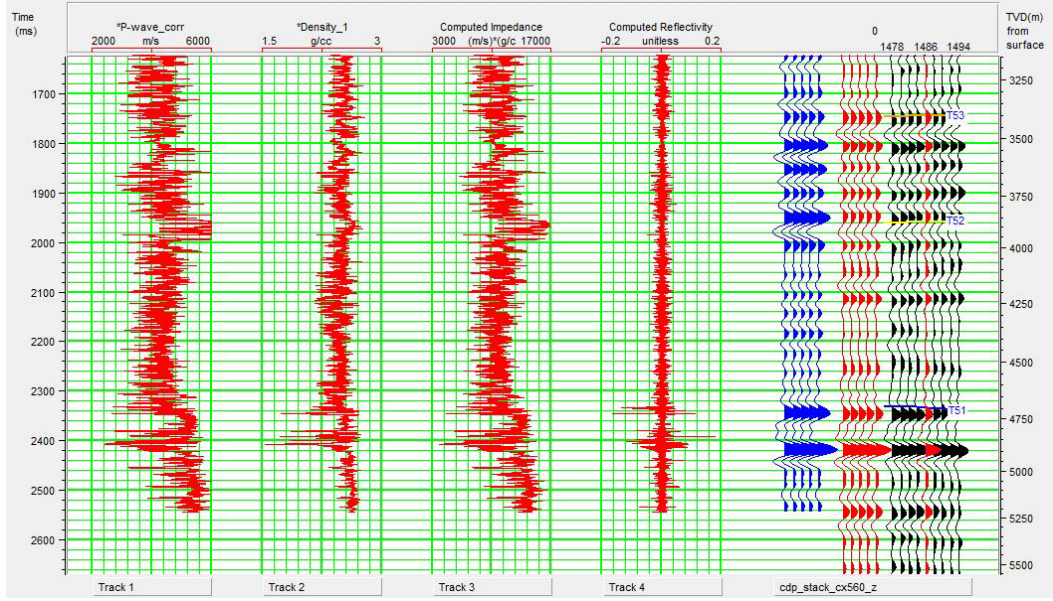
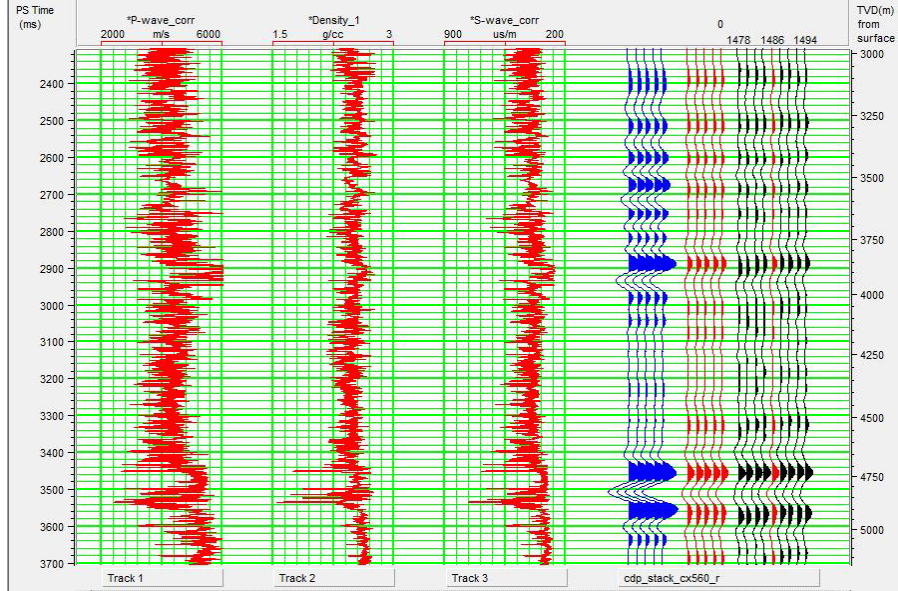


**Figure 6.2** Well log portions within the target reservoir area from the well CX560.





(a)



(b)

**Figure 6.3** (a) Correlation between the well logs (Figure 6.2) and the P-P seismic stack section shown in Figure 6.1a. (b) Well-tie applied to the P-S stack section of Figure 6.1b. The correlation coefficients are 0.8213 and 0.7532.

## 6.2 Derivation of converted ray impedance

The converted wave reflectivity expression in Wang (1999) is truncated as

$$R_{ps}(p) \approx -\frac{\alpha}{\beta} \left( \frac{\Delta\mu}{\rho} q_{\alpha} p - \frac{\Delta\mu}{\rho} \frac{1}{q_{\beta}} p^3 \right) \quad (6.1)$$

where  $q_\alpha$  and  $q_\beta$  are the average vertical slownesses for P wave and S wave respectively. In Figure 6.4, the accuracy of (6.1) is compared with the linearised approximation of the Zoeppritz equations (Aki and Richards, 1980), which has been widely used by various authors (e.g., Jin et al., 2000; Stewart et al., 2003; González, 2006). This comparison cites the same five examples described in section 1.4 and from these figures we can observe that generally expression (6.1) is more accurate than the Aki and Richards (1980) linearised approximation except the case shown in Figure 6.4b. However, in the only example where the pseudo quadratic approximation performs worse, the linearised one is no longer accurate as well before the pseudo quadratic behaves worse. Based on these analyses, I will adopt equation (6.1) in the derivation of converted ray impedance and relevant P-S-wave issues.

Substitute

$$\frac{\Delta\mu}{\rho} \approx \beta^2 \left( \frac{\Delta\rho}{\rho} + 2 \frac{\Delta\beta}{\beta} \right),$$

$$q_\alpha \approx \frac{\cos\theta}{\alpha} \text{ and } q_\beta \approx \frac{\cos\varphi}{\beta}$$

into equation (6.1) we will have

$$-R_{ps}(p) = 2\kappa \frac{\Delta\beta}{\beta} + \kappa \frac{\Delta\rho}{\rho}, \quad (6.2)$$

where  $\kappa = \beta p \sqrt{1 - \alpha^2 p^2} - \frac{\alpha\beta^2}{\sqrt{1 - \beta^2 p^2}} p^3$ . I deliberately move the negative sign to the

left hand side of (6.2) in order to have the same polarity on P-P and P-S field data when  $\alpha$ ,  $\beta$  and  $\rho$  all change in the same direction. Similar to the derivation of EI and RI, CRI should be related to P-S reflectivity in the same way that AI relates to zero-offset P-P reflectivity, satisfying

$$-R_{ps}(p) = \frac{CRI_{i+1}(p) - CRI_i(p)}{CRI_{i+1}(p) + CRI_i(p)}. \quad (6.3)$$

Hence

$$\frac{1}{2} \Delta \ln CRI = -R_{ps}(p) = 2\kappa \Delta \ln \beta + \kappa \Delta \ln \rho, \quad (6.4)$$

and then

$$CRI(p) = \beta^{4\kappa} \rho^{2\kappa} = \mu^{2\kappa}. \quad (6.5)$$

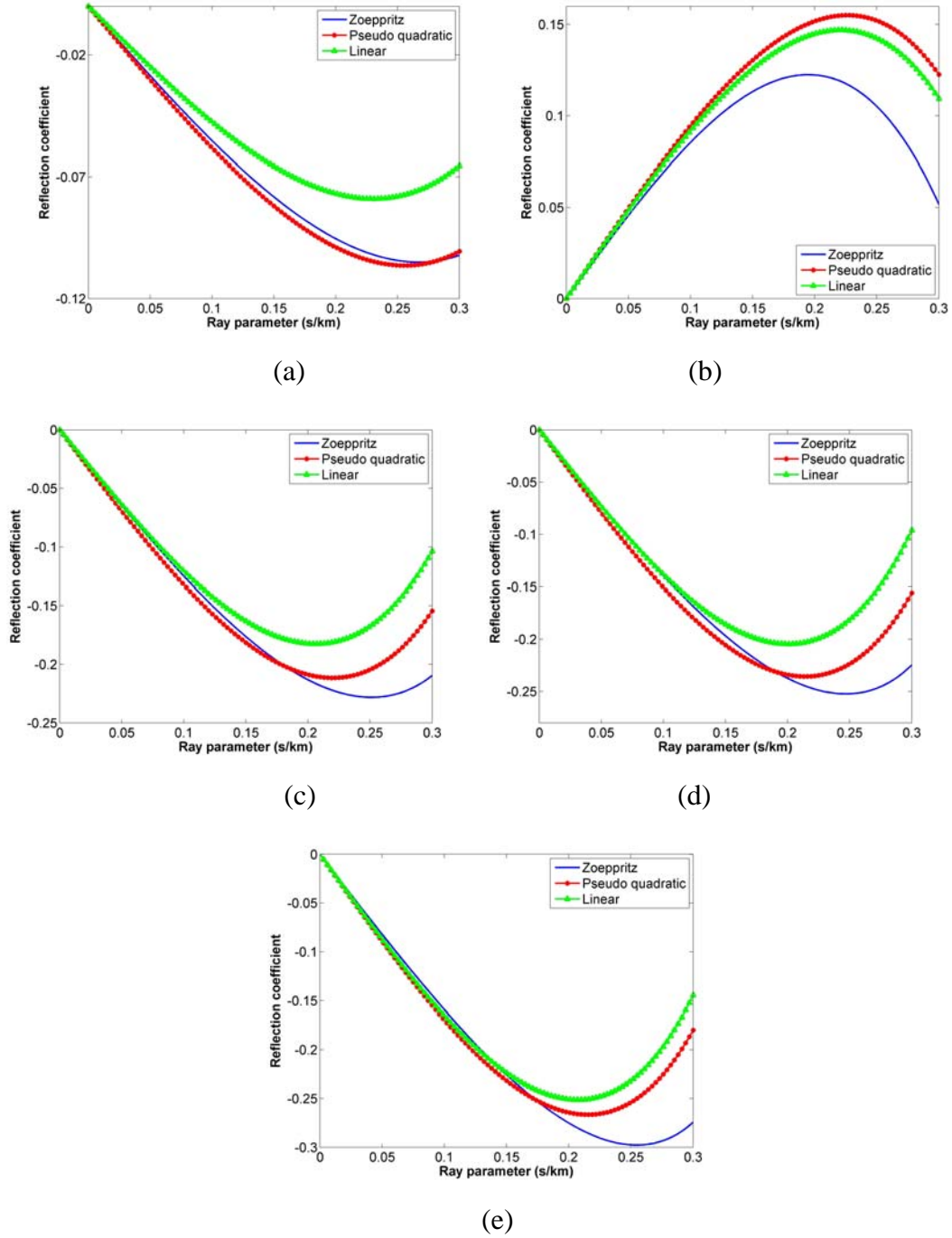


**Figure 6.4** P-S reflection coefficient comparisons between the pseudo quadratic expression (6.1) and the Aki and Richards linearised approximation with the exact values from Zoeppritz equations. (a)-(e) correspond to the five examples described in section 1.2.

Making the integral of equation (6.4) on both sides to be (6.5), the coefficients need to be constant for each ray parameter value. From the analysis on the real well log (Figure 6.2), it turns out that the variation of  $\kappa$  is about 25% (Figure 6.5) but it has to be treated as a constant in integrating equation (6.4), in the same way as in SEI derivation (Landrø et al., 1999; Duffant et al., 2000; González, 2006). Actually  $\kappa$  can be transformed into  $\kappa = \sin \varphi (\cos \theta - \sin \theta \tan \varphi)$  where  $\varphi$  is the converted S-wave angle. For a certain  $\theta$  value plus the assumption of fixed  $\beta/\alpha$  ratio, which makes  $\varphi$  unchanged as well,  $\kappa$  will be a constant for each angle stack. This kind of assumption is commonly adopted in elastic impedance derivation for both P-P waves (Connolly, 1999) and P-S waves (Landrø et al., 1999; Duffant et al., 2000; González, 2006). For the convenience of the reader, I copy the expression of SEI from González (2006) here as

$$SEI(\theta) = \rho^c \beta^d,$$

where

$$c = \frac{\beta}{\alpha} \frac{\sin \theta}{\sqrt{\frac{a^2}{\beta^2} - \sin^2 \theta}} \left( 2 \sin^2 \theta - \frac{a^2}{\beta^2} - 2 \cos \theta \sqrt{\frac{a^2}{\beta^2} - \sin^2 \theta} \right)$$

and

$$d = \frac{4\beta}{\alpha} \frac{\sin \theta}{\sqrt{\frac{a^2}{\beta^2} - \sin^2 \theta}} \left( \sin^2 \theta - \cos \theta \sqrt{\frac{a^2}{\beta^2} - \sin^2 \theta} \right).$$

The SEI derivation from Landrø et al. (1999) and Duffant et al. (2000) is slightly different as they use another linear approximation to the P-S wave Zoeppritz coefficient. As the latter linear approximation is seldom adopted by other authors, I will only compare the converted-wave ray impedance with the SEI derived from the Aki and Richards approximation.

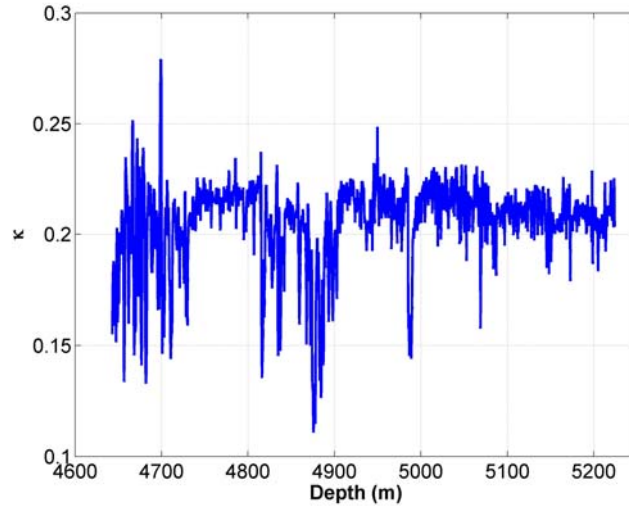


**Figure 6.5** Variation of  $\kappa$  over a portion of the well logs shown in Figure 6.2.

To further confirm that the converted ray impedance (6.5) is a good link connecting prestack seismic data with well logs, a synthetic modelling test from the real well logs (Figure 6.2) is implemented. For this experiment, the log data situated between the top of  $T3X^4$  and the bottom of the well have been converted to two-way traveltime, approximately spanning from 1.72s to 2.6s. In Figure 6.6 the left trace is generated by convolving a Ricker wavelet (dominant frequency 20Hz) with the reflectivity series obtained from the Zoeppritz equations. The reflectivity series of the middle trace is synthesised from (6.3) and (6.5) and that for the right trace is calculated from the SEI (González, 2006) and a similar expression of (6.3). Here both CRI and SEI are regarded as intrinsic rock properties which are used in the same way as AI, EI and RI. All the traces in Figure 6.6 have the same ray parameter value  $p = 100 \text{ s/km}$  and the  $\kappa$  value in using (6.5) is a constant averaged over the whole window. However the angle value of SEI varies according to different velocities in different layers in order to retain a constant ray-parameter value and the ratio of S-wave velocity over P-wave velocity in SEI is an averaged constant for the whole window.

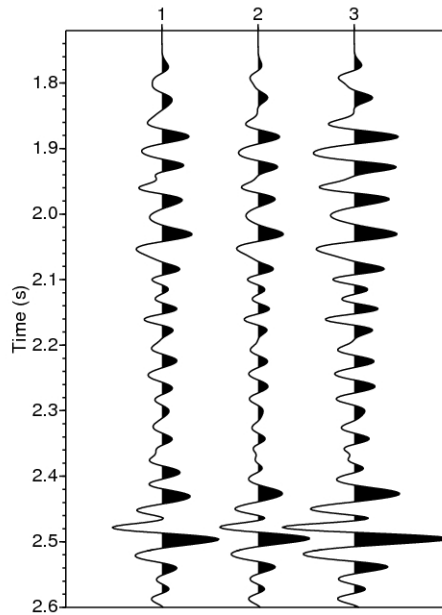


**Figure 6.6** Synthetic traces using (from left to right) Zoeppritz equations, converted ray impedances and shear elastic impedances.

The correlation coefficients for the 2nd and 3rd traces with the first trace are both 0.93. However the amplitude of the synthetic trace using SEI (3rd) is visibly stronger than the other two with a RMS value of 1.62 after normalisation using the RMS amplitude of the 1st trace synthesised from Zoeppritz equations. Whereas the normalised RMS amplitude of the middle trace is 0.84, slightly weaker than the real one. This comparison takes into account the errors that are originated from the assumption of constant exponentials in both CRI and SEI, together with the accuracy loss of the pseudo-quadratic and the linear approximations to the Zoeppritz equations (Figure 6.4), which makes it more convincing to adopt the CRI in P-S wave inversion.

Both CRI and SEI do not have the dimensionality of impedance and we can adopt a similar normalisation strategy as in elastic impedance (Whitcombe, 2002). This practice will not affect the accuracy in the above modelling comparison.

### 6.3 Event matching between P-P and P-S waves

In joint P-P and P-S analysis, the importance of robust correlation between P-P and P-S waves can not be overemphasised. Miscorrelation of key stratal surfaces will lead to

erroneous seismic attributes when doing inversion or making inaccurate interpretation and hence a robust P-P and P-S matching scheme plays an important role in the success of joint inversion or interpretation.

In a thin layer, the ratio between the travel time of a P-P wave and P-S wave is related to the ratio of P-wave to S-wave velocities by

$$\frac{\alpha}{\beta} = \frac{2T_{ps}}{T} - 1. \quad (6.7)$$

where  $T$  and  $T_{ps}$  are the P-P and P-S travel time. As a consequence, the registration of P-P and P-S waves usually coincides with the estimation of  $\alpha/\beta$  (Li et al., 2000). Gaiser (1996) quantitatively estimated the ratio of P-wave velocity to S-wave velocity through correlation techniques. Rickett and Lumley (2001) and Zhang and Wang (2009) correlated corresponding events by identifying maximum cross-correlation in local windows. From an interpreter's perspective, DeAngelo et al. (2003) matched P-P and P-S events through time slice correlation on 3D datasets. Fomel and Backus. (2003) and Nickel and Sonneland (2004) both presented automatic event registration methods originated from image processing techniques (e.g. Fischer and Modersitzki, 2003).

Here I simplified the image registration method presented by Fomel and Backus (2003) by minimising the objective function

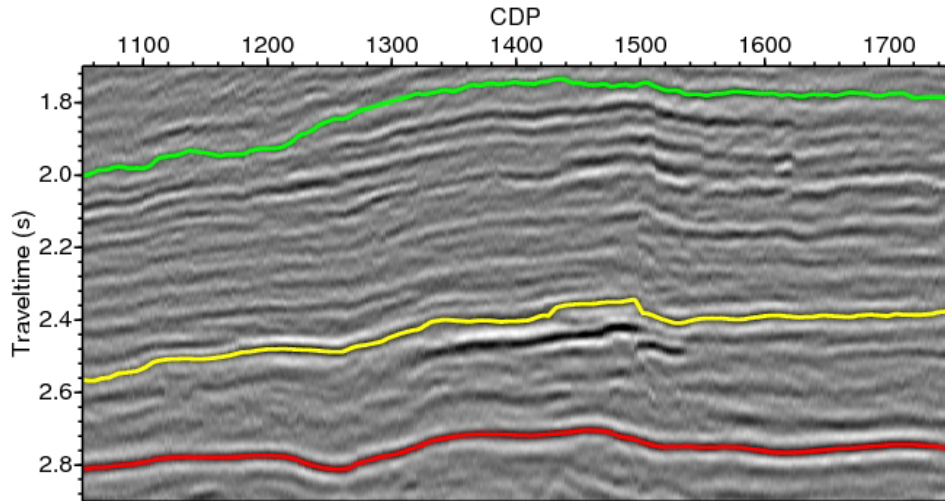
$$\|d_{pp}(T) - a(T)d_{ps}(\psi(T))\|^2 + \eta\|\psi''(T)\|^2 \quad (6.8)$$

where  $a(T)$  represents the amplitude tuning function and  $\psi(t)$  is the warping function denoting the correspondence of reflection events in the two images. The least-squares minimisation of the first term in (6.8) is underdetermined as we normally squeeze the P-S time into P-P time. Hence the second smoothness constraint term is necessary to make the inversion problem well-defined. As the amplitude tuning function  $a(T)$  appears linearly in the equation, this inversion problem is referred as separable nonlinear least-squares and can be solved by a variable projection technique (Golub and Pereyra, 2003). The least-squares objective function (6.8) is minimised with the Gauss-Newton method and in order to avoid being trapped in a local minimum, we need a good initial  $\psi(T)$  function to start with. In my approach, I establish the

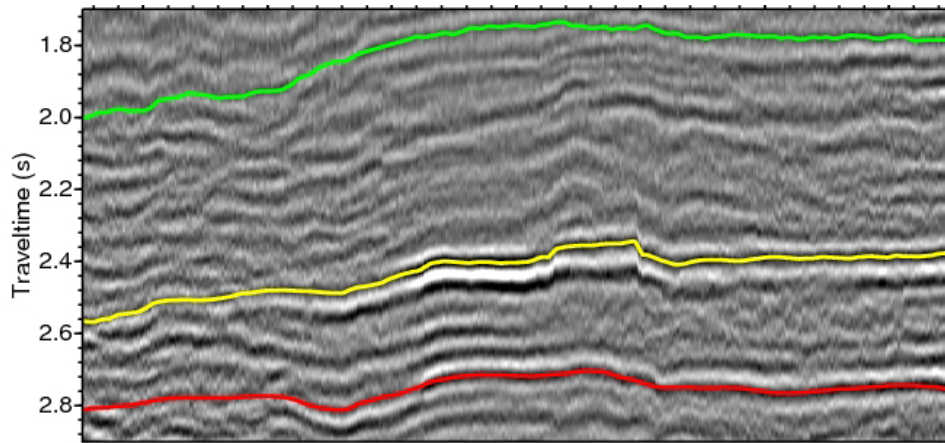
correspondence by correlating several interpreted horizons on both P-P and P-S stacks and linearly interpolate the warping functions at intermediate parts. As  $a(T)$  does not change rapidly by having a good initial guess of  $\psi(t)$ , it can be calculated by matching the instantaneous amplitude of the P-P waves and P-S waves and during each iteration  $a(T)$  is updated.

Figure 6.7a and 6.7b compare the P-P and P-S stack sections after the initial matching of those correlated horizons that have been interpreted. The final P-S image obtained by minimising (6.8) is an improved registration result (Figure 6.7c). The correlation coefficients at each CDP position are compared between the initial matching (red) and the final matching (blue) in Figure 6.8(a). In correlation calculation, the window starts from the top of  $T3X^4$  (green) and ends at the bottom of  $T3X^2$  (red). The amplitude spectra of the P-P data (grey), the P-S data before (red) and after (blue) the final registration are plotted in Figure 6.8(b) for reference. On the left part of Figure 6.8(a), the low correlation values indicate poor matching in this area. This is due to the lack of coherent events as a consequence of poor imaging on the P-S section. Figure 6.9 displays the warping P-S time functions (coloured values) regarding the P-P time (vertical axis) for all CDP locations. These values will be used to match correlating events in joint P-P and P-S analysis. As an important product of this registration, the  $\alpha/\beta$  ratios after the initial and the final match are compared in Figure 6.10.

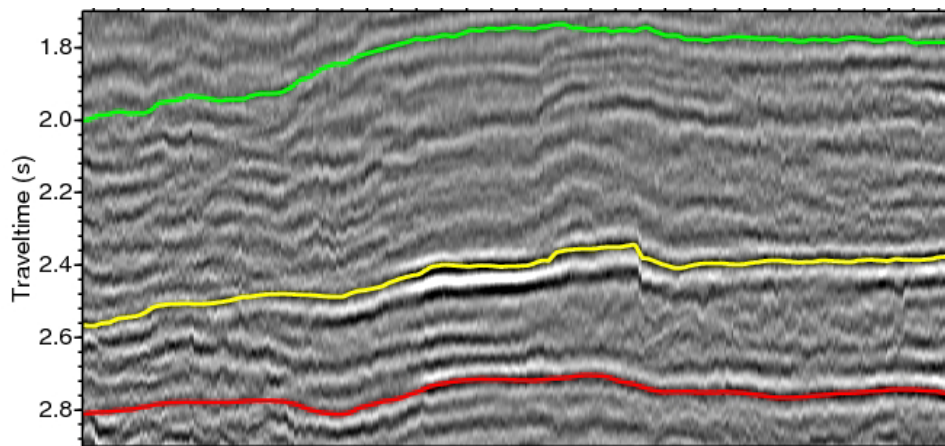




(a)

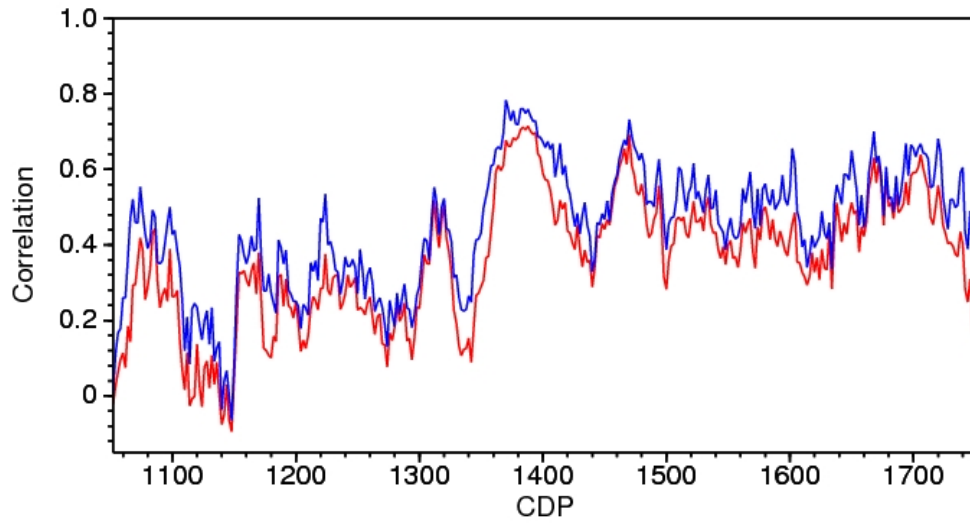


(b)

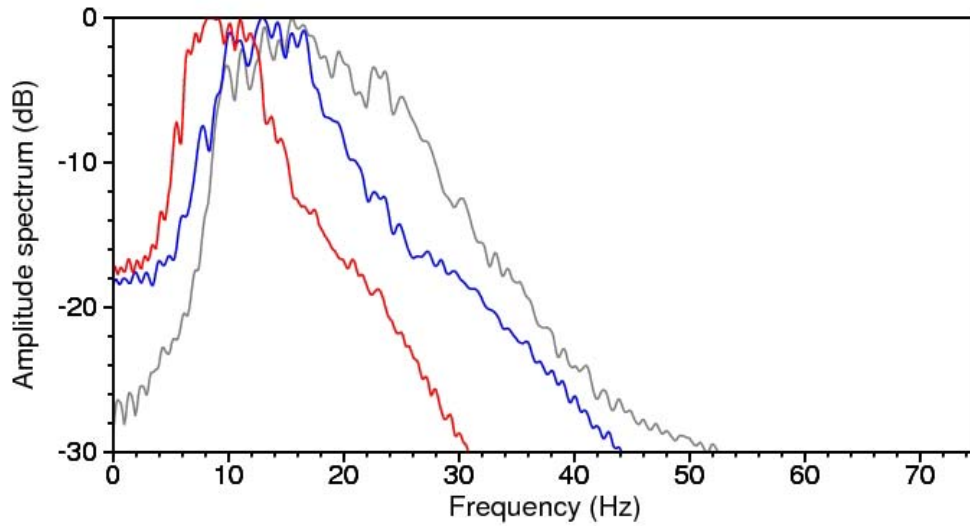


(c)

**Figure 6.7** (a) The reference P-P stack section. (b) The registered P-S stack by matching interpreted horizons. (c) The final P-S stack matched to P-P time through iterative inversion.



(a)



(b)

**Figure 6.8** (a) Correlation coefficient comparison performed at each CDP location between the initial matching result (red) and the final matching result (blue). (b) The amplitude spectra of the P-P data (grey), the P-S data before (red) and after (blue) the final registration.

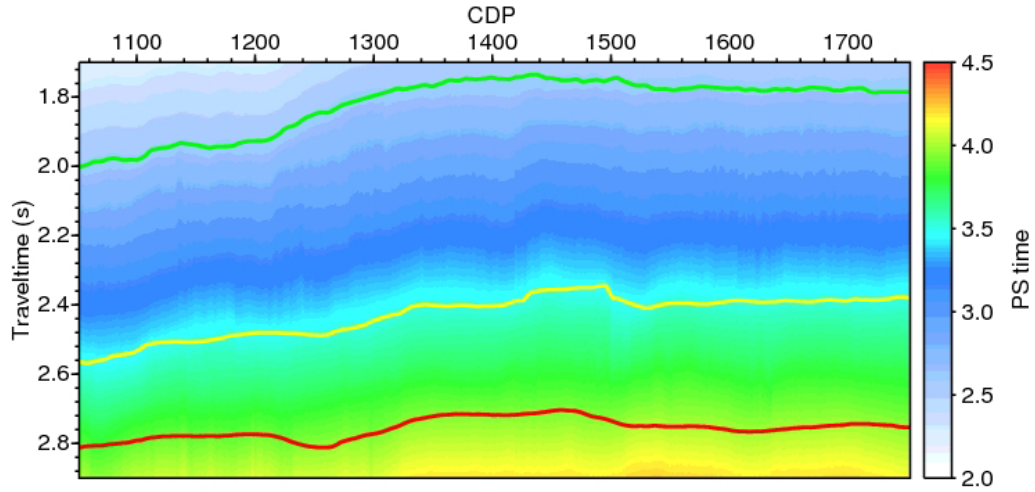


**Figure 6.9** Warping P-S time functions corresponding to P-P time leading to the final registered P-S image in Figure 6.6c.

When applying this image matching algorithm, the reflection events are assumed to be positioned laterally correctly after the migration so that the registration is only performed by vertical transformations. In doing this kind of matching, I try to remove the time differences between correlating P-P and P-S events, however there are three other discrepancies between P-P and P-S profiles which may affect the accuracy of this matching: different amplitude responses for the same geological interface, different wavelet frequency contents and phase uncertainties between P-P and P-S profiles. This inversion algorithm can automatically address the first problem through the use of an amplitude tuning function  $a(T)$ . After registration the P-S wave spectrum is usually stretched resulted from squeezing in the time domain. This effect can be removed to recover the original P-S wave frequency responses by using a similar spectrum correction scheme in the Gabor transform domain inverse Q filtering algorithm (Wang, 2006, 2008; Zhang and Wang, 2009). As for the phase uncertainties, we can perform a residual constant phase check using the method of White (1988) (as described in Chapter 2) on both sorts of profiles and match their phases before registration. Alternatively, the phase difference can be derived from cross-correlating P-P and P-S data after they are registered.

Considering the intrinsic problems in events matching, e.g. correlating P-P and P-S events are not always found in both seismic data, and the extrinsic problems, such as the noise left in either dataset, it is extremely difficult to have a perfect matching, i.e.,

the correlation coefficients all reach one. From a practical perspective, only the major correlated P-P and P-S events around target horizons need to be matched and the uncertainty is left between them by reasonable interpolation. Our algorithm follows this principle but tries to reduce the uncertainty to a minimum level before carrying out joint analysis or joint inversion. The algorithm stability also benefits from a local smoothing strategy by calculating the central velocity ratio within a window across a group of traces.

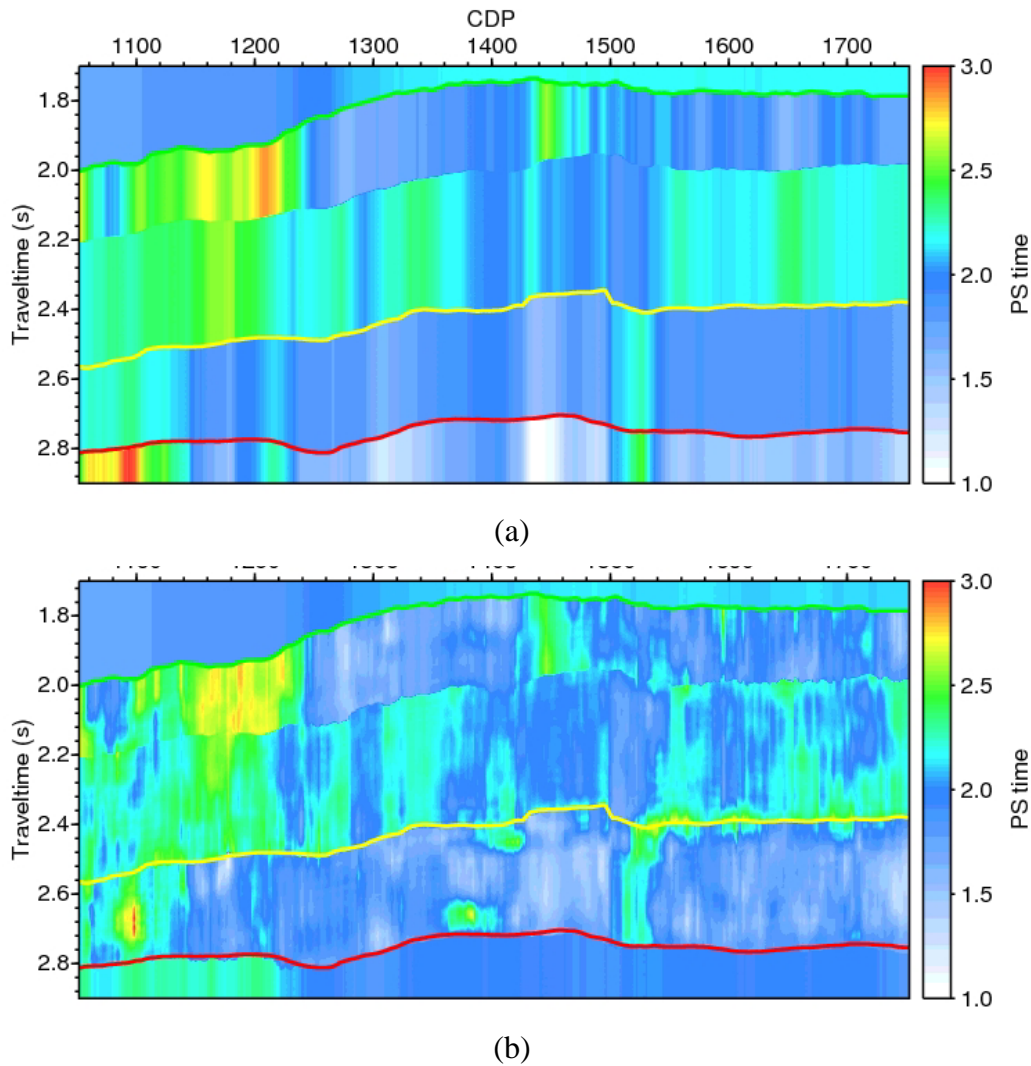


**Figure 6.10** Estimated P to S velocity ratio from (a) the initial match using interpreted horizons and (b) the updated match after the iterative inversion.

#### 6.4 Inversion result analysis

For P-P seismic data, ray impedance inversion (depicted in Chapter 4) is firstly carried out on constant ray-parameter profiles. From the obtained ray impedance

profiles, a further elastic parameter inversion is implemented to obtain both P-impedance and S-impedance. Figure 6.11 shows the inversion results at the well location (CDP 1486) compared with well-log-calculated values for QC purpose. Those synthetic curves can offer us a direct impression of impedance values corresponding to different sand groups. The plots, from (a) to (c), are corresponding to ray impedance at  $p = 0.1s/km$ , P-impedance and S-impedance.

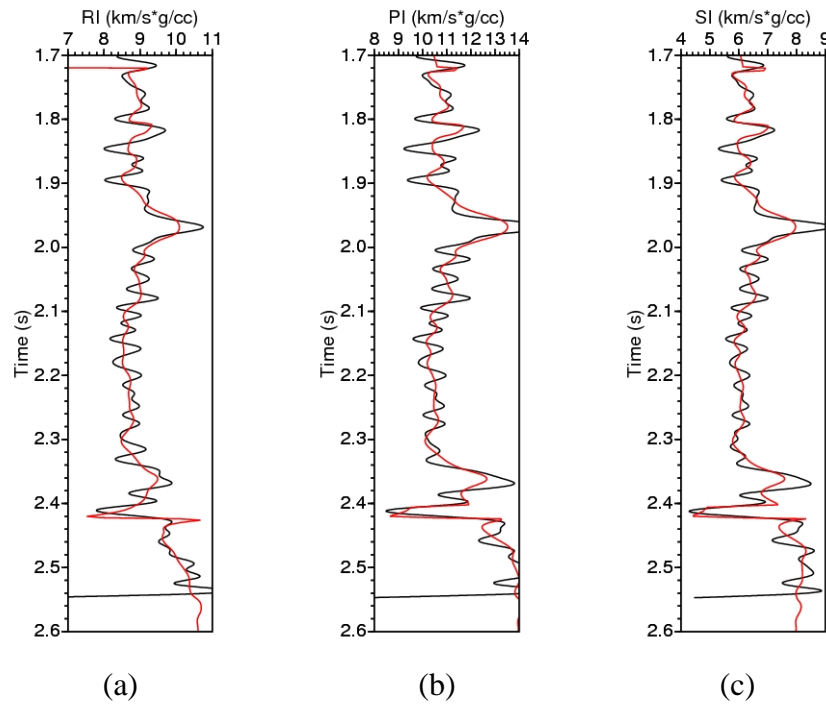
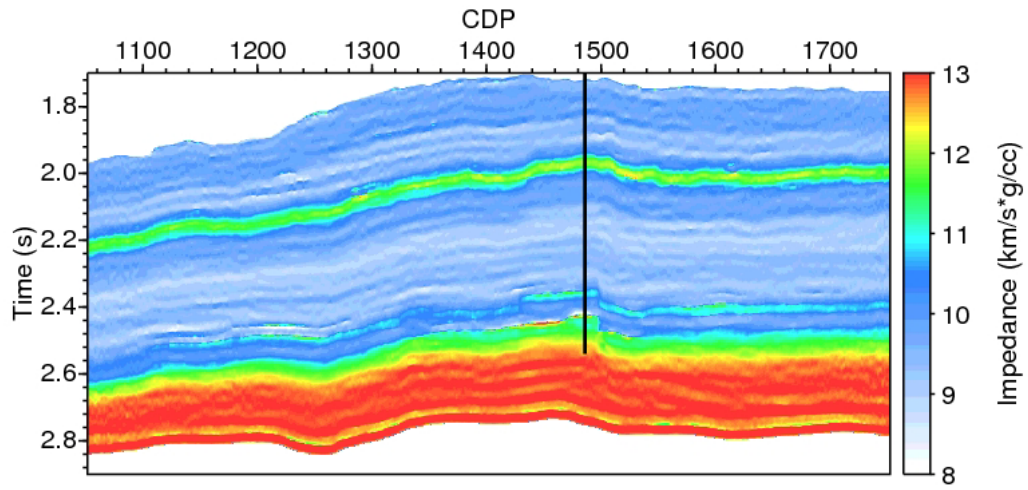


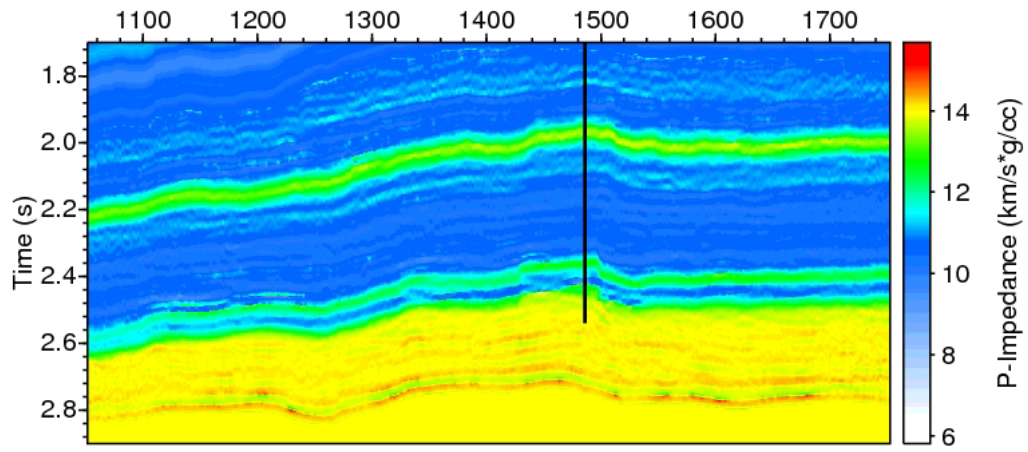
**Figure 6.11** Inversion results (red) compared with well log synthetics (black). (a) Ray impedance at  $p = 0.1s/km$ , (b) P-impedance and (c) S-impedance.

The inversion results show good correlations with the theoretical values. The two potential gas-bearing formations situated within  $T3X^4$  and  $T3X^2$  are distinguished as high impedance values at about TWT  $\sim 1.97s$  and  $\sim 2.37s$ . However the major gas-producing reservoir in this well is  $T3X^4$ , which is characterised by higher ray impedance values than  $T3X^2$ . The P-impedance in these two formations, as well as S-impedance values, are somewhat close with slightly higher values in  $T3X^4$ . The whole inverted impedance profiles for this 2D line are displayed in Figure 6.12, (a) – (c) are corresponding to those in Figure 6.11. The black vertical lines indicate the well position.

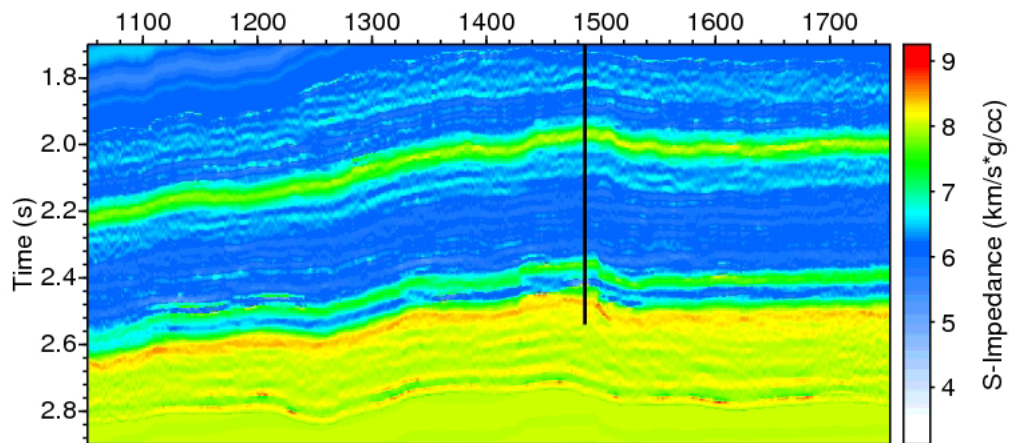




(a)



(b)



(c)

**Figure 6.12** Inversion results for the whole line (a) Ray impedance at  $p = 0.1s/km$ , (b) P-impedance and (c) S-impedance.

Converted-wave ray-impedance inversion consists of a similar work flow to the P-P wave ray-impedance inversion: (1) transforming common-image-point gathers from the offset domain to the ray-parameter domain for prestack time-migrated multi-component seismic data; (2) forming constant ray-parameter profiles; (3) estimating mixed-phase wavelets for different constant-ray-parameters; (4) sparseness-constrained reflectivity inversion; (5) converted-wave ray impedance inversion and (6) change the P-S time into P-P time for the convenience of interpretation.

Figure 6.13 shows the inverted CRI profile ( $p = 0.1s/km$ ) after being converted from P-S time to P-P time by applying the warping functions in Figure 6.9, and the calibration with the well log synthetic is plotted in Figure 6.14. To assess these inversion results, I extract some sample impedance values within the two producing formations  $T3X^4$  and  $T3X^2$ . At each CDP position, the sample value in either formation for a specific impedance type is averaged within a window of TWT 40ms. This window size is about the real thickness of either producing reservoir. Figure 6.15 compares the crossplots between RI versus AI (in a) and CRI versus AI (in b). Both the RI and CRI are inverted at the same ray parameter  $p = 0.1s/km$ . In both crossplots, the major producing formation  $T3X^4$  is clustering as a unique group whereas the behaviours of  $T3X^2$  are different. The area denoted by the red circle in either crossplot corresponds to the low impedance zone (CDP 1052-1122), which can be identified on both crossplots. However for CDP positions 1122-1266, the abnormal low impedance is only observed on the crossplot Figure 6.15(b) (denoted by the black circle), which is attributed to the low CRI values inverted. The distribution of the producing formation  $T3X^2$  encountered in well CX560 is not as wide as the major producing formation  $T3X^4$ . This point is clear from either crossplot. However the crossplot between CRI and AI further tells us that there is another low impedance zone which can not be identified from the RI inversion result and may need different treatment. The CRI inversion result can further help us in identifying the major gas reservoir in this 2D line area.

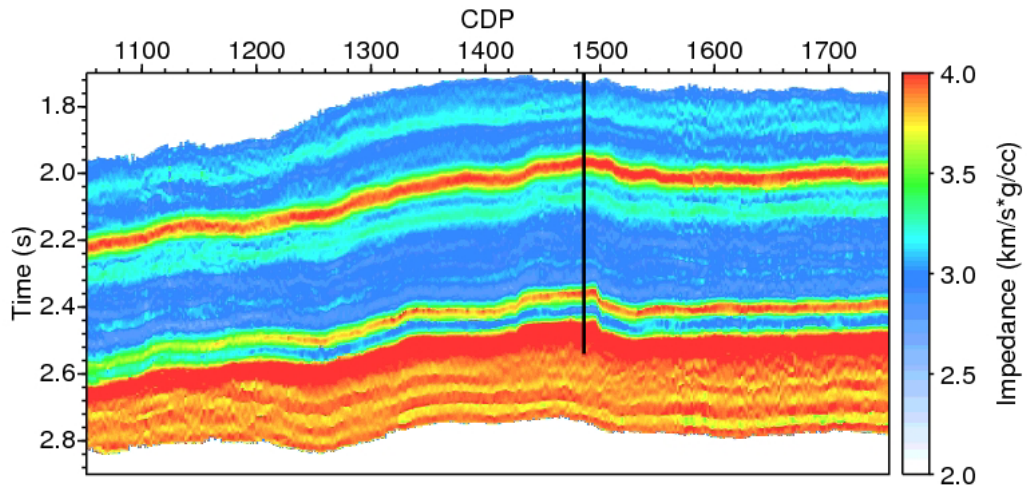


**Figure 6.13** Converted ray impedance inversion result.

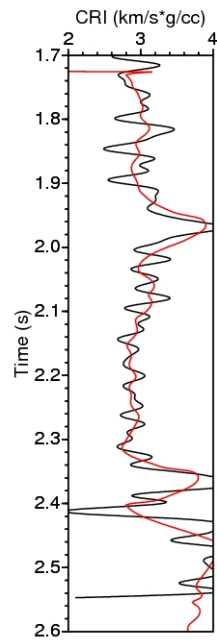


**Figure 6.14** Converted ray impedance at  $p = 0.1s/km$  compared with well log derived synthetics.



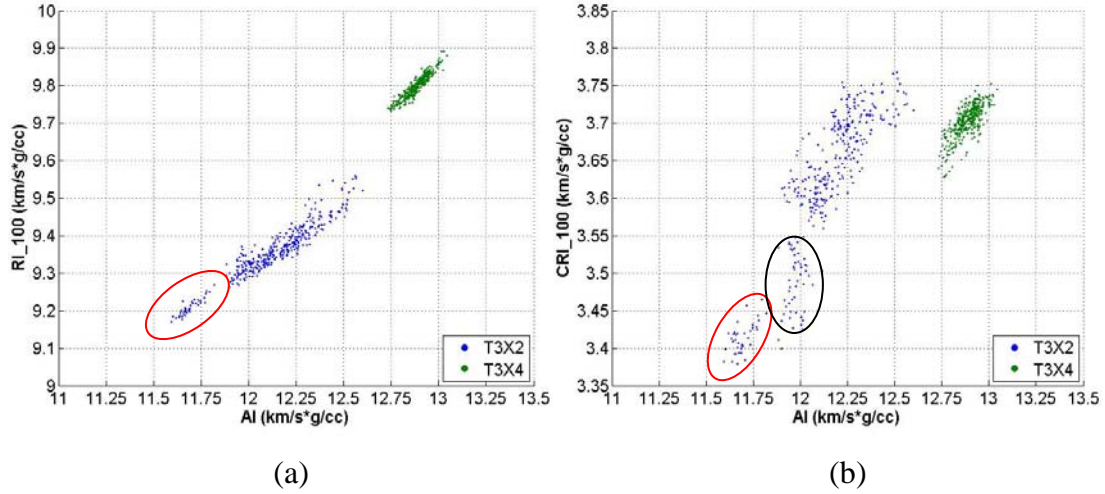


**Figure 6.15** (a) Crossplot between RI ( $p = 0.1s/km$ ) and AI. (b) Crossplot between CRI ( $p = 0.1s/km$ ) and AI.

## 6.5 Conclusions

In this chapter, I present a novel converted ray-impedance inversion method for P-S converted waves and analyse it together with the ray-impedance and elastic-parameter inversion results obtained in the prestack domain from P-P waves. In analysing P-S data, the pseudo quadratic approximation to the Zoeppritz equations for P-S reflectivity is more accurate than the Aki and Richards linear approximation in most cases. This superiority directly results in a more appropriate physical quantity in calibrating well logs to P-S reflection data. For a joint analysis of P-P and P-S reflection data in the ray-parameter domain, the inversion results with the same ray-parameter values actually come from the same group of seismic rays, for both P-P and P-S waves. This makes it intuitive and straightforward for us to make direct comparisons between different types of seismic reflection data.



## Chapter 7

### Conclusions and future work

#### 7.1 General conclusions

Zoeppritz equations describing the reflection coefficients exactly at an interface consist of seven independent variables: P-wave velocity, S-wave velocity and density at both sides of the interface plus ray parameter. Simplified expressions, such as the Aki and Richards (1980) linear approximation, make the formula more succinct by superseding the ray parameter with the incident angle at the interface. This practice significantly reduces the complexity and follows human intuition in using the reflectivity coefficients at a single interface. However in a multi-layer medium, the angle value may be misleading as it varies with the layer velocity for the same seismic ray. The derivation of the conventional elastic impedance has to sacrifice the accuracy by assuming weak contrasts between layers and the angle values at both sides of an interface to be equal to their average. This practice obviously violates Snell's law and researchers have tried to address this interior problem of elastic impedance since its birth by defining new type of "elastic" impedance on the ray parameter (VerWest, 2000; Wang, 2003a; Santos and Tygel, 2004). In this way, Snell's law is naturally favoured and interfaces are no longer limited to the weak contrast assumption.

Alternative impedances have been theoretically proposed by the above authors, however their applications were not demonstrated, the detailed techniques were not dealt with and the potential of using this type of impedances were not shown. These problems are all discussed in this dissertation which starts from the ray impedance definition of Wang (2003a). In Chapter 1, the ray impedance concept is compared with the elastic impedance by showing the superiority of the former in discriminating lithologies.

Chapter 2 deals with the important issue of wavelet in both seismic processing and inversion. The wavelet extracted from the well log and seismic data combination is theoretically the most accurate, however it requires an appropriate time-depth relationship to generate a proper well-tie between them. A cumulant matching between the wavelet and seismic data is implemented via a linearised inversion technique to statistically extract the wavelet, which can be used directly in processing and inversion when well information is not available, or to correlate well logs to seismic data for further wavelet processing. The restrictions in statistical wavelet estimation are acknowledged and well discussed. With the development of modern acquisition instruments and techniques, statistical wavelet estimation maintains its important role in seismic exploration, especially when no well is drilled.

Chapter 3 describes the inversion of sparse seismic reflectivity sequences under a quantitative Cauchy norm. This norm has its advantage over the Gaussian norm as the latter will result in a smoothed least-squares solution and is not preferable for a blocky impedance inversion, plus we know that the natural character of reflectivities is rarely Gaussian but leptokurtic. Hence the Cauchy norm is a more reasonable selection in reflectivity inversion. However we found that the final inverted reflectivity sequences tend to be Gaussian gradually after iterations although this Gaussian distribution is very different from the previous one. This is because the Cauchy norm is only applied on the model term, and the data misfit term is still considered to be with Gaussian distribution. It is also observed that both the Cauchy and Gaussian norms applied on model term can partially recover the original reflectivity bandwidth but within different frequency components. As a consequence I try to integrate their resolution-enhancing abilities in one result through a frequency domain data merging technique, whose results are more suitable for blocky impedance inversion.

Ray impedance profiles are generated through the generalised linear inversion scheme and the results are utilised to identify rock properties and lithologies in Chapter 4. The interpretation from our results is consistent with that from the previous AVO analysis on the same dataset. It has also been demonstrated that we can invert P- and S-wave impedance directly from the ray impedance, with the density term naturally absorbed into the P-impedance and S-impedance terms. I also examine the ability of ray

impedance to recover three elastic parameters ( $\alpha$   $\beta$   $\rho$ ) simultaneously but it comes out that a stable solution is largely attributed to the constraints rather than the data. This means that ray impedance does not alter the ill-condition character of density inversion. These results are all well documented in Chapter 5.

Chapter 6 discloses a new way in jointly analysing P-P and P-S wave data through the proposal of converted-wave ray impedance. The novel concept of converted-wave ray impedance shows some advantages over the shear-wave elastic impedance in relating well logs to P-S reflection data and consequently in P-S wave elastic inversion. The joint analysis of P-P and P-S waves in the ray-parameter domain has a definite physical meaning since they come from the same group of seismic rays if the inversion results are obtained with the same ray-parameter value. Integrating the P-S wave inversion result into the analysis will boost our confidence in lithology interpretation. Up to this point, the prestack seismic inversion under the framework of ray impedance for both P-P and P-S waves has been established.

## **7.2 Future work**

There are several ways summarised in Chapter 1 to reconstruct CIP gathers from the offset domain to ray-parameter domain. But none of them is accurate enough when the subsurface structure is geologically complex. The local slope mapping method is accurate when subsurface structures are all flat and also applicable when slight dip angles exist with reflectors. The ray-tracing method in CIP gathers has significantly removed the geological structure effect through migration, but errors emerge when transforming CIP gathers from the offset domain to the ray-parameter domain by the bending ray-tracing scheme. To be accurate, the dipping effect needs to be considered during migration, which should always be carried out before inversion when it is possible (Bacon et al, 2003; Avseth et al., 2005), to image the CIP gathers in the ray-parameter domain directly. Some preliminary researches have tried to migrate seismic data into prestack angle domain directly (De Bruin et al., 1990; Prucha et al., 1999; Xu et al., 2001; Xie and Wu, 2002; Rickett and Sava, 2002; Sava and Fomel, 2003; Biondi and Symes, 2004) for elastic inversion and AVA analysis/inversion, and a

similar algorithm could be developed for accurate ray-parameter domain CIP gathers as well. For more accurate imaging, anisotropy should also be accounted.

Modern evolution of seismic acquisition and processing techniques makes the quality of the dataset supplied to seismic prestack inversion improved dramatically. The enhanced effective bandwidth and signal-to-noise ratio make the prestack inversion method more robust. Apart from advances in the traditional seismic processing, there is another category of cosmetic techniques designed for AVO analysis or prestack inversion, e.g. align correlating events for different offset, deserves our attention.

Stemming from ray impedance definition, the density term needs further investigation in elastic parameter inversion. As ray impedance is valid only in a regime of relatively small angle values (corresponding to  $30 - 35^\circ$  limitation in elastic impedance), so is the two-term elastic inversion algorithm in which the density term is naturally absorbed into the P- and S-impedance terms. Using the modern long-offset seismic data in inversion, the density term must stand out as an individual part contributing to the reflection coefficient. As the quadratic reflection expression is much more accurate than the Aki and Richards linear equation (Mallick, 1993; Wang, 1999), investigation regarding density inversion should rely on the former.

Throughout this thesis, I use the deterministic inversion scheme to solve those non-linear least-squares problems, which involves a Gauss-Newton method to update the model(s) iteratively. Deterministic approaches are generally faster and economical in terms of computation cost, however the solution may be trapped in a local minimum in non-linear inversion problems or sometimes the vertical resolution is restricted by the seismic bandwidth. Stochastic inversion has long been used in reservoir characterisations, particularly in the development stage of an oil field, for the high resolution it can achieve (Haas and Dubrule, 1994; Torres-Verdin et al, 1999; Rowbotham et al., 2003; etc.). In exploration seismic, stochastic approaches are also popular to address certain inversion problems, e.g., Helgesen et al., (2000), Velis and Ulrych (1996) and Velis (2008). These algorithms, together with some recent developments in evolutionary algorithm, such as the Ant Colony Optimization

algorithm (Chen et al., 2005 and Hajizadeh et al., 2009), can also be tried for the various inversions described in this thesis.

### **7.3 Software developed**

In doing the research of ray impedance inversion, I wrote a whole software package for ray impedance inversion starting with the offset domain prestack data after migration. Most images displayed in the thesis are generated by the package I developed, apart from Figure 2.9 and Figure 6.3 for interactive well-tie practice and the wavelet extracted in Figure 2.10 for comparison purpose. Most of the algorithms involve a large amount of computation are coded in C under the environment of Seismic Unix (CWP, Colorado School of Mines) and those related to lithology modelling and analysis are written in Matlab.





## **Publications**

### *Peer-reviewed paper:*

Lu, X. and Wang, Y., 2007, Mixed-phase wavelet estimation by iterative linear inversion of high-order statistics: *Journal of Geophysics and Engineering*, 4, 184-193.

### *Conference presentations:*

Lu, X. and Wang, Y., 2009, Elastic parameters inversion through ray impedance: 71st EAGE conference, Expanded Abstracts, S023.

Lu, X. and Wang, Y., 2009, Sparseness of seismic reflectivity inversion: 71<sup>st</sup> EAGE conference, Expanded Abstracts, P085.

Lu, X. and Wang, Y., 2007, Mixed-phase wavelet estimation by linear inversion of high-order statistics: 69th EAGE conference, Expanded Abstracts, P267.

Lu, X. and Wang, Y., 2006, Seismic acoustic impedance inversion in the pre-stack domain: 68th EAGE conference, Expanded Abstracts, P057.



## References

- Aki, K., and Richards, P. G., 1980, Quantitative seismology: theory and methods: W.H. Freeman.
- Amundsen, L., 1991, Comparison of the least-squares criterion and the Cauchy criterion in frequency-wavenumber inversion: *Geophysics*, 56, 2027-2035.
- Avseth, P., 2000, Combining rock physics and sedimentology for seismic reservoir characterization of North Sea turbidite systems: PhD Thesis, Stanford University.
- Avseth, P., Mukerji, T. and Mavko, G., 2005, Quantitative Seismic Interpretation - Applying Rock Physics Tools to Reduce Interpretation Risk: Cambridge University Press.
- Bacon, M., Simm, R. and Redshaw, T., 2003, 3-D seismic interpretation: Cambridge University Press.
- Biondi, B. and Symes, W., 2004, Angle-domain common-image gathers for migration velocity analysis by wavefield-continuation imaging: *Geophysics*, 69, 1283-1298.
- Castagna, J. P., Batzle, M. L., Eastwood, R. L., 1985, Relationships between compressional-wave and shear-wave velocities in clastic silicate rocks: *Geophysics*, 50, 571-581.
- Chen, S., Wang, S. and Zhang, Y., 2005, Ant colony optimization for the seismic nonlinear inversion: 75th SEG Annual International Meeting, Expanded Abstracts, 1732-1734.
- Claerbout, J. F., 1992, Earth soundings analysis: Processing versus inversion: Blackwell Scientific Publications, Inc.
- Cooke, D. A. and Schneider, W. A., 1983, Generalized inversion of reflection seismic data: *Geophysics*, 48, 665-676.
- Connolly, P., 1999, Elastic impedance: *The Leading Edge*, 18, 438-452.
- DeAngelo, M. V., Backus, M., Hardage, B. A. and Murray, P., 2003, Depth registration of P-wave and C-wave seismic data for shallow marine sediment characterization, Gulf of Mexico: *The Leading Edge*, 22, 96-105.

- De Bruin, C. G. M., Wapenaar, C. P. A. and Berkhout, A. J., 1990, Angle-dependent reflectivity by means of Prestack migration: *Geophysics*, 55, 1223-1234.
- Debye, H. W. J., and van Riel, P., 1990, Lp-norm deconvolution: *Geophysical Prospecting*, 38, 381–403.
- Debski, W. and Tarantola, A., 1995, Information on elastic parameters obtained from the amplitudes of reflected waves: *Geophysics*, 60, 1426-1436.
- De Nicolao, A., Drufuca, G. and Rocca, F., 1993, Eigenvectors and eigenvalues of linearized elastic inversion: *Geophysics*, 58, 670–679.
- Diebold, J. B., and Stoffa, P. L., 1981, The travelttime equation, tau-p mapping, and inversion of common midpoint data: *Geophysics*, 46, 238-254.
- Duffaut, K., Alsos, T., Landrø, M., Rognø, H. and Al-Najjar, N., 2000, Shear-wave elastic impedance: *The Leading Edge*, 19, 1222-1229.
- Fatti, J. L., Smith, G. C., Vail, P. J., Strauss, P. J., and Levitt, P. R., 1994, Detection of gas in sandstone reservoirs using AVO analysis: A 3-D seismic case history using the Geostack technique: *Geophysics*, 59, 1362-1376.
- Fischer, B. and Modersitzki, J., 2003, Curvature based image registration: *Journal of Mathematical Imaging and Vision*, 18, 81-85.
- Fomel, S., 2002, Applications of plane-wave destruction filters: *Geophysics*, 67, 1946-1960.
- Fomel, S. and Backus, M. M., 2003, Multicomponent seismic data registration by least squares, 73rd SEG Annual International Meeting, Expanded Abstracts, 781-784.
- Freedman, D.A., Pisani, R. and Purves, R.A., 1978, *Statistics*: W.W. Norton, Inc. New York.
- Gaiser J. E., 1996, Multicomponent Vp/Vs correlation analysis: *Geophysics*, 61, 1137–1149.
- Gan, Q., Xu, D., Tang, J., and Wang, Y., 2009, Seismic resolution enhancement for tight-sand gas reservoir characterization: *Journal of Geophysics and Engineering*, 6, 21–28.
- Gardner, G. H. F., Gardner, L. W., and Gregory, A. R., 1974, Formation velocity and density — The diagnostic basis for stratigraphic traps: *Geophysics*, 39, 770-780.
- Giannakis, G. B., 1987, Cumulants: a powerful tool in signal processing. *Proceedings of the IEEE*, 75, 1333-1334.

- Golub, G. and Pereyra, V., 2003, Separable nonlinear least squares: the variable projection method and its application: *Inverse Problems*, 19, R1-R26.
- Gonzalez, E., 2006, Physical and quantitative interpretation of seismic attributes for rocks and fluids identification: PhD Thesis, Stanford University.
- Gonzalez, E., Mukerji, T. and Mavko, G., 2000, Facies classification using P-to-P and P-to-S AVO attributes, 70th SEG Annual International Meeting, Expanded Abstracts, 98-101.
- Goodway B., Chen T. W. and Downton J., 1997, Improved AVO fluid detection and lithology discrimination using Lamé petrophysical parameters; “Lambda-Rho”, “Mu-Rho”, & “Lambda/Mu fluid stack”, from P and S inversions. 67th SEG Annual International Meeting, Expanded Abstracts, 183–186.
- Haas, A. and Dubrule, O., 1994, Geostatistical inversion – a sequential method of stochastic reservoir modelling constrained by seismic data: *First Break*, 12, 561–569.
- Hajizadeh, Y., Christie, M. and Demyanov, V., 2009, Ant colony optimization algorithm for history matching: 71st EAGE conference, Expanded Abstracts, R022.
- Helgesen, J., Magnus, I., Prosser, S., Saigal, G., Aamodt, G., Dolberg, D. and Busman, S., 2000, Comparison of constrained sparse spike and stochastic inversion for porosity prediction at Kristin Field: *The Leading Edge*, 19, 400–407.
- Hendrickson, J. S., 1999, Stacked: *Geophysical Prospecting*, 47, 663-705.
- Jensås, I., Eidsvik, J. and Theune, U., 2008, Methods for Blocky Seismic AVA Inversion: 70th EAGE conference, Expanded Abstracts, P345.
- Jin, S., Cambois, G. and Vuillermoz, C., 2000, Shear-wave velocity and density estimation from PS-wave AVO analysis: Application to an OBS dataset from the North Sea: *Geophysics*, 65, 1446-1454.
- Jones, I. F., 2010, Tutorial: Velocity estimation via ray-based tomography: *First Break*, 28, 45-52.
- Lazear, G. L., 1993, Mixed-phase wavelet estimation using fourth-order cumulants: *Geophysics*, 58, 1042-1051.
- Levy, S. and Fullagar, P. K., 1981, Reconstruction of a sparse spike train from a portion of its spectrum and application to high resolution deconvolution: *Geophysics*, 46, 1235-1243.

- Li, X. Y., 2000, Converted-wave velocity analysis: searching for  $V_c$  and  $\gamma$ : 62nd EAGE Annual International Meeting, Expanded Abstracts, L0051.
- Liang, G, Cai, X., and Li, Q., 2002, Using high-order cumulants to extrapolate spatially variant seismic wavelets: *Geophysics*, 67, 1869-1876.
- Landrø, M., Duffaut, K. and Rognø, H., 1999 Well calibration of seabed seismic data: 69th SEG Annual International Meeting, Expanded Abstracts, 860-863.
- Liu, G., Formel, S., Jin, L. and Chen, X., 2009, Stacking seismic data using local correlation: *Geophysics*, 74, V43-V48.
- Longbottom, J., Walden, A. T. and White, R. E., 1988, Principles and application of maximum kurtosis phase estimation: *Geophysical Prospecting*, 36, 115-138.
- Lu, X., and Wang, Y., 2007, Mixed-phase wavelet estimation by iterative linear inversion of high-order statistics: *J. Geophys. Eng.*, 4, 184–193.
- Mallick, S., 1993, A simple approximation to the P-wave reflection coefficient and its implication in the inversion of amplitude variation with offset data: *Geophysics*, 58, 544–552.
- Mendel, J. M. 1991, Tutorial on higher-order statistics (spectra) in signal processing and system theory: theoretical results and some applications: *Proc. IEEE*, 79, 278-305.
- Menke, W., 1984, *Geophysical data analysis: Discrete inverse theory*: Academic Press Inc.
- Mora, P., 1987, Nonlinear two-dimensional elastic inversion of multioffset seismic data: *Geophysics*, 52, 1211-1228.
- Mora, P., 1988, Elastic wave-field inversion of reflection and transmission data: *Geophysics*, 53, 750-759.
- Nickel, M. and Sonneland, L., 2004, Automated PS to PP event registration and estimation of a high-resolution  $V_p/V_s$  ratio volume: 74 th SEG Annual Meeting, Expanded Abstracts, 869-872.
- Oldenburg, D. W., Scheuer, T., and Levy, S., 1983, Recovery of the acoustic impedance from reflection seismograms: *Geophysics*, 48, 1318-1337.
- Ostrander, W. J., 1984, Plane-wave reflection coefficients for gas sands at nonnormal angles of incidence: *Geophysics*, 49, 1637-1649.
- Potter C. C. and Stewart R. R., 1998, Density predictions using  $V_p$  and  $V_s$  sonic logs: CREWES Research Report, Volume 10.

- Prucha, M., Biondi, B. and Symes, W., 1999, Angle-domain common-image gathers by wave-equation migration: 69th SEG Annual International Meeting, Expanded Abstracts, 824–827.
- Ramos, A. C. B. and Castagna, J. P., 2001, Useful approximations for converted wave AVO: *Geophysics*, 66, 1721-1734.
- Rickett, J. E. and Lumley, D. E., 2001, Cross-equalization data processing for time-lapse seismic reservoir monitoring: A case study from the Gulf of Mexico: *Geophysics*, 66, 1015-1025.
- Rickett, J. and Sava, P., 2002, Offset and angle-domain common image-point gathers for shot profile migration: *Geophysics*, 67, 883-889.
- Rietsch, E., 1980, Estimation of the signal-to-noise ratio of seismic data with an application to stacking: *Geophysical Prospecting*, 28, 531–550.
- Robinson, E. A., and Treitel, S., 1980, *Geophysical signal analysis*: Englewood Cliffs, N.J., Prentice-Hall Inc.
- Robinson, J. C., 1970, Statistically optimal stacking of seismic data: *Geophysics*, 35, 436-446.
- Rowbotham, P. S., Marion, D., Lamy, P., Insalaco, E., Swaby, P. A. and Boisseau, Y., 2003, Multidisciplinary stochastic impedance inversion: integrating geological understanding and capturing reservoir uncertainty: *Petroleum Geoscience*, 9, 287-294.
- Russell, B. H., Hedlin, K., Hilterman, F. J., and Lines, L. R., 2003, Fluid-property discrimination with AVO: A Biot-Gassmann perspective: *Geophysics*, 68, 29-39.
- Rutherford, S. R., and Williams, R. H., 1989, Amplitude-versus-offset variations in gas sands: *Geophysics*, 54, 680-688.
- Sacchi, M. D., and Ulrych, T. J., 1995, High resolution velocity gathers and offset space reconstruction: *Geophysics*, 60, 1169-1177.
- Sacchi, M. D., and Ulrych, T. J., 1996, Estimation of the discrete Fourier transform a linear inversion approach: *Geophysics*, 61, 1128-1136.
- Sacchi, M. D., 1997, Re-weighting strategies in seismic deconvolution: *Geophys. J. Internat.*, 129, 651-656.
- Sava, P. and Fomel, S., 2003, Angle-domain common image gathers by wavefield continuation methods, *Geophysics*, 68, 1065-1074.
- Scales, J. A. and Tenorio, L., 2001, Prior information and uncertainty in inverse problems: *Geophysics*, 66, 389-397.

- Shuey, R. T., 1985, A simplification of the Zoeppritz equations: *Geophysics*, 50, 609-614.
- Smith, G. C., and Gidlow, P. M., 1987, Weighted stacking for rock property estimation and detection of gas: *Geophysical Prospecting*, 35, 993-1014.
- Stewart, R. R., Gaiser, J. E., Brown, R. J. and Lawton, D. C., 2003, Converted-wave seismic exploration: Applications: *Geophysics*, 68, 40-57.
- Stolt, R. H. and Weglein, A. B., 1985, Migration and inversion of seismic data: *Geophysics*, 50, 2458–2472.
- Tarantola, A., 1986, A strategy for nonlinear elastic inversion of seismic reflection data: *Geophysics*, 51, 1893-1903.
- Tarantola, A., 1987, *Inverse problem theory*: Elsevier Science Publ. Co., Inc.
- Tarantola, A., and Valette, B., 1982, Inverse problems D quest for information: *J. Geophys.*, 50, 159–170.
- Treitel, S., Gutowski, P. R., and Wagner, D. E., 1982, Plane-wave decomposition of seismograms: *Geophysics*, 47, 1375-1401.
- Torres-Verdin, C., Victoria, M., Merletti, G. and Pendrel, J., 1999, Trace-based and geostatistical inversion of 3-D seismic data for thin-sand delineation: An application in San Jorge Basin, Argentina: *The Leading Edge*, 18, 1070–1077.
- Tyapkin, Y., and Ursin, B., 2005, Optimum stacking of seismic records with irregular noise: *J. Geophys. Eng.*, 2, 177-187.
- Ulrych, T. J., Sacchi, M. D., and Woodbury, A., 2001, A Bayes tour of inversion: A tutorial: *Geophysics*, 66, 55–69.
- Ursin, B., and Tjaland, E., 1992, Information content of the elastic reflection matrix: 62nd SEG Annual International Meeting, Expanded Abstracts, 796–799.
- Van der Baan, M. A. R., 2008, Time-varying wavelet estimation and deconvolution by kurtosis maximization: *Geophysics*, 73, V11-V18.
- Velis, D. R., 2008, Stochastic sparse-spike deconvolution: *Geophysics*, 73, R1-R9.
- Velis, D. R. and Ulrych, T. J., 1996, Simulated annealing wavelet estimation via fourth-order cumulant matching: *Geophysics*, 61, 1939-1948.
- VerWest, B., Masters, R. and Sena, A., 2000, Elastic impedance inversion: 70th SEG meeting, Expanded Abstracts, 1580-1582.
- Walden, A. T. and Hosken, J. W. J., 1985, An investigation of the spectral properties of primary reflection coefficients: *Geophysical Prospecting*, 33, 400-435.



- Walden, A. T. and Hosken, J. W. J., 1986, The nature of the non-Gaussianity of primary reflection coefficients: *Geophysical Prospecting*, 34, 1038-1066.
- Walden, A. T. and White, R. E., 1998, Seismic wavelet estimation: A frequency domain solution to a geophysical noisy input-output problem, *IEEE Transactions on Geoscience and Remote Sensing*, 1998, 287-297.
- Wang, Y., 1999, Approximations to the Zoeppritz equations and their use in AVO analysis: *Geophysics*, 64, 1920-1927.
- Wang, Y., 2003a, *Seismic Amplitude inversion in reflection tomography*: Elsevier Science Ltd.
- Wang, Y., 2003b, Multiple attenuation: coping with the spatial truncation effect in the Radon transform domain: *Geophysical Prospecting*, 51, 75-87.
- Wang, Y., 2006, Inverse Q-filter for seismic resolution enhancement: *Geophysics*, 71, V51-60.
- Wang, Y., 2008, *Seismic Inverse Q filtering*. Blackwell Publishing, Oxford.
- Wapenaar, C. P. A., Verschuur, D. J., and Herrmann, P., 1992, Amplitude preprocessing of single and multicomponent seismic data: *Geophysics*, 57, 1178-1188.
- Whitecombe, D. N., 2002, Elastic impedance normalization: *Geophysics*, 67, 60-62.
- White, R. E., 1977, The performance of optimum stacking filters in suppressing uncorrelated noise: *Geophysical Prospecting*, 25, 165-178.
- White, R., E., 1984, Signal and noise estimation from seismic reflection data using spectral coherence method: *Proc. IEEE*, 72, 1340-1356.
- White, R. E., 1988, Maximum kurtosis phase correction: *Geophysical Journal*, 95, 371-389.
- Wiggins, R. A., 1978, Minimum entropy deconvolution: *Geoexploration*, 16, 21-35.
- Wijngaarden, A. J. and Berkhout, A. J., 1996, Resolution analysis on AVO attributes: 66th SEG Annual International Meeting, Expanded Abstracts, 1711-1714.
- Wu, Y., 2000, Estimation of gas saturation using P-to-S converted waves: 70th SEG Annual International Meeting, Expanded Abstracts, 158-161.
- Xie, X. B. and Wu, R. S., 2002, Extracting angle domain information from migrated wavefield: 72nd SEG Annual International Meeting, Expanded Abstracts, 1360-1363.
- Xu, S., Chauris, H., Lambaré, G. and Noble, M., 2001, Common-angle migration: A strategy for imaging complex media: *Geophysics*, 66, 1877-1894.

- Yilmaz, O., 2001, *Seismic Data Analysis: Processing, Inversion and Interpretation of Seismic Data*: Society of Exploration Geophysicists.
- Zhang, F. and Wang, Y., 2009, Amplitude-preserving calibration of PP- and PS-wave reflection events, 71st EAGE Annual International Meeting, Expanded Abstracts P087.
- Zhang, Y., Xu, S., Bleistein, N. and Zhang, G., 2007, True amplitude angle domain common image gathers from one-way wave equation migrations: *Geophysics*, 72, S49-58.
- Zhu, F., Gibson, R. L., Atkins, J. and Yuh, S. H., 2000, Distinguishing fizz gas from commercial gas reservoirs using multicomponent seismic data: *The Leading Edge*, 19, 1238-1245.